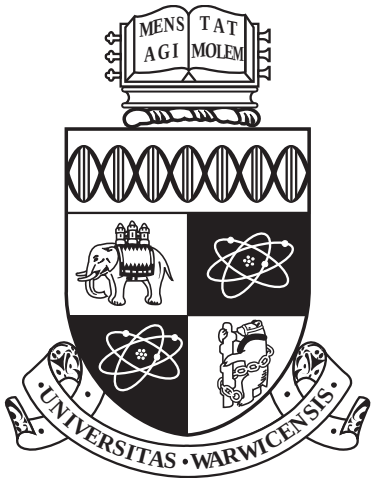

Gaseous Electron Multipliers (GEM)-Based UV Photomultiplier Devices

by

James Bryant

Thesis

Submitted to the University of Warwick

for the degree of

Doctor of Philosophy

Department of Physics

September 2018

THE UNIVERSITY OF
WARWICK

Contents

List of Tables

List of Figures

Acknowledgments

I would like to thank my supervisors Gavin Bell and Yorck Ramachers, first for giving me the opportunity to work on this project and for all their help throughout. They have been incredibly friendly and approachable and have always been there to help whenever needed.

Also special thanks to Raffaello de Campo for all his expertise and work as an external supervisor. His bounds of energy and helpful nature helped move along the project on many occasions.

Many thanks to all my friends for making my time at University of Warwick lots of fun. Especially everyone in the office, who always found new and exciting ways to not do work. Special thanks goes to Chris Burrows, who was the best postdoc senpai anyone could ask for, and Marc Walker for all his help with XPS and various other things.

Shout out to the lunch crew and Mohammed Saghir in particular for always making lunch time become an interesting conversation.

I would also like to thank all the people in the electronics workshop especially Tung Fai Yu and David Greenshields, who helped design, build and maintain a variety of electrical components and despite being very busy were heavily involved in the project.

Special thanks also to the guys at mechanics workshop: Matty Mills and Lance Fawcett, for creating a variety of different devices and for putting up with my terrible technical drawings.

Declarations

I declare that this thesis reports my work between October 2014 and September 2018 under the supervision of Dr Gavin Bell and Dr Yorck Ramachers. The research reported here has not been submitted either wholly or part in any other academic institution for admission to a higher degree.

The work presented was carried out by the author except in the cases outlined below: Electronics used in these devices were primarily built by the electronics workshop and mechanical parts by the mechanical workshop.

XPS data was taken by Dr Marc Walker in the Warwick Photoemission Facility, however the analysis of the data was performed by the author. Some of the Reflection measurements and water absorption measurements in chapter 6 were taken by Dr Martin Spangenberg and Dr Philip Mousley, who were working on similar research projects and helped with a variety of aspects of the project.

Abstract

The gain stability of Thick Gaseous Electron Multipliers (ThGEMs) and a novel structure coined gaseous gap electron multiplier (GGEM) was investigated. It was found there was a rising signal over a period of several hours to days which depends on the electric field strength and is only stopped by removing the element from the chamber. Whilst it cannot solely be due to charging of rims as suggested in literature as there is none for GGEMs it could also possibly be due to charging of other dielectric in the chamber.

Copper, magnesium and zinc oxide were investigated as possible air-stable ultra-violet (UV) photocathodes. The copper used was from the surface of the printed circuit board (PCB) used in the fabrication of ThGEMs and the copper foil used to make the GGEMs. Magnesium and zinc oxide films were grown via thermal deposition in vacuum, by changing the oxidation methods used when growing the films we are able to get some basic qualitative comparison on how the oxide state effects its properties as a photocathode. Both MgO and ZnO were found to be remarkably stable in air, despite an initial change, they settled to an ambient work function (WF) which was found to change very little for very long periods, such as several months to a year.

Mechanically polishing the copper surface with Brasso was found to increase the signal and therefore the quantum yield (QY) by around 5 to 6 times, despite little to no change in measured WF using a Kelvin Probe. It was found using X-ray Photoelectron spectroscopy XPS that polishing the copper surface removed the $CuO/Cu(OH)_2$ leaving behind more metallic copper which must have a higher QY.

For both MgO and ZnO films it was found that if the samples were oxidised in vacuum they appeared to have lower work function than if oxidised in ambient conditions. From XPS measurements the increase in work function was attributed to a larger $MgCO_3$ and hydrozincite components respectively. With the decrease in WF with ambient exposure being attributed to a larger MgO component.

Both MgO and ZnO were found to have a range of possible signals, in part due to the rising gain behaviour, however there was a general trend of lower WF resulted in higher signal.

Some possible applications for ThGEM-based Gaseous Photomultiplier (GPM) devices have been investigated, in particular real-time water monitoring which we showed is possible by investigating the quantities of 3 different chemicals: potassium hydrogen phthalate, clothiandin and tryptophan.

Abbreviations

AES Auger Electron Spectroscopy

AMU Atomic Mass Unit

CHA Concentric Hemispherical Analyser

CMA Cylindrical Mirror Analyser

CPD Contact Potential Difference

DDS Dynamic Derivative Spectroscopy

ETE Electron Transfer Efficiency

EQE External Quantum Efficiency

FWHM Full Width Half Maximum

GEM Gaseous Electron Multiplier

GGEM Gaseous Gap Electron Multiplier

GPM Gaseous Photomultiplier

HOPG Highly-Ordered Pyrolytic Graphite

IBF Ion Backflow Fraction

IMFP Inelastic Mean Free Path

KHP Potassium Hydrogen Phthalate

KP Kelvin Probe

LED Light Emitting Diode

LIXPS Low Intensity X-ray Photoemission Spectroscopy

MHSP Micro-Hole Strip Plate

MM-ThGEM Multi-Mesh Thick Gaseous Electron Multiplier

MPGD Micro-Pattern Gaseous Detectors

MSGC Micro-Strip Gaseous Chamber

MWPC Multi-Wire Proportional Chamber

NLOS Non-Line Of Sight

PCB Printed Circuit Board

PD Photodiode

PEEK Polyetheretherketone

PMT Photomultiplier Tube

PTFE Polytetrafluoroethylene

PVD Physical Vapour Deposition

QY Quantum Yield

QE Quantum Efficiency

RICH Ring Imaging Cherenkov

RQE Relative Quantum Efficiency

SIMS Secondary Ion Mass Spectrometry

ThGEM Thick Gaseous Electron Multiplier

TPC Time Projection Chamber

UPS Ultraviolet Photoemission Spectroscopy

UV Ultra-Violet

VUV Vacuum Ultra-Violet

WF Work Function

XPS X-ray Photoelectron Spectroscopy

Chapter 1

Introduction

1.1 Preface

The topic of this thesis is the construction of Thick Gaseous Electron Multiplier (ThGEM)-Based Gaseous Photomultiplier (GPM) devices and a review on their potential applications as ultraviolet (UV) light detectors. In this thesis the operating conditions of gaseous electron multipliers, including a novel design coined in this thesis as a 'Gaseous Gap Electron Multiplier' (GGEM) which is constructed without the dielectric between the holes of the two electrode plates, will be investigated. The growth and characterization of metal oxide UV photocathodes will also be investigated, including the effect of chemical composition and their stability over time in gaseous and ambient conditions.
The gain stability of gaseous electron multipliers was investigated by measuring the photocurrent under illumination, shown in chapter 3. The photocathodes chemical composition was investigated using a technique called X-ray Photoelectron Spectroscopy (XPS) and the work function was measured using a single point Kelvin probe in ambient conditions to see how the composition of the surface affects the work function (WF), as shown in chapter 4. The relative and absolute quantum yields of the photocathodes are also measured and calculated, as shown in chapter 5, to see how well these materials perform as UV photocathodes. Finally, in chapter 6 the potential applications of ThGEM-based GPMs are reviewed and some proof-of-concept measurements are taken.

1.2 Motivation

Over the last decade or so, ultraviolet (UV) light sources have been rapidly improving, decreasing in size and cost whilst increasing in power and quantum efficiency (QE) especially at shorter wavelength emission. Gas discharge lamps using noble gases have been a standard for the emission of vacuum ultra-violet (VUV) light, especially in applications such as ultraviolet photoelectron spectroscopy (UPS) where helium is the most commonly used [4]. However

for most commercial applications, UV light emitting diodes (LEDs) are now more commonly used over UV discharge lamps as they are cheaper, smaller, have narrower wavelength emission, higher energy efficiency, longer lifetimes, less fluctuation in light intensity, small standby time and low heat generation [5, 6]. UV LEDs can also be tuned to have specific wavelength emissions anywhere in the UV range (400nm-200nm). Despite their numerous disadvantages compared to LEDs, gas discharge lamps are still used in some applications as they are capable of shorter wavelength emission and higher powers.

Recently, there has been marked improvements in the performance of deep ultraviolet UVC (200-280nm) LEDs. In particular, AlGaN has been researched as a possible material for high VUV LEDs with high QE. A group at the University of South Carolina reported the first AlGaN-based VUV LEDs between 250nm and 280nm in 2004 [7, 8, 9]. For the 280nm LED a record external quantum efficiency (the number of photons emitted from the LED to the number of electrons passing through the device) of over 1% was reached, however for the deeper 250nm LED only 0.01% EQE was reached. More recently, a EQE as high as 1.5% was reached for 280nm LEDs [10].

These recent improvement in cheap, small and powerful UVC light sources mean applications using UVC are becoming much more viable, as such, cheap and robust UVC detectors will also be required. These detectors will need to have a sharp cut-off in their responsivity at solar wavelengths so as not to be affected by background solar light, this particular property of detectors is called 'solar-blind detection', as it is not affected by the solar portion of the spectrum.

The UVC part of the UV spectrum ($< 280nm$) is of particular interest to various applications, as there is basically no ground level background. This is because these wavelengths are almost completed absorbed in the upper atmosphere, the remaining radiation in this wavelength range only accounting for ($< 1\%$) of the total solar irradiance at ground level [11]. UVC light sources are currently used in various applications such as: environmental sensing [12], disinfection [13], spectroscopy [14], medical diagnostics [15] and communication [16]. In particular UVC LEDs are used as they have a tunable narrow bandwidth and can be cheaply produced.

Although there is significant research towards wide-gap semiconductor photodiodes (PDs) [17] (including the development of avalanche PDs which have internal gain resulting in much higher sensitivity) these devices still have a small detector area and UV focusing optics are expensive. Therefore large area UV applications currently still require the use of multiple Photomultiplier Tubes (PMTs) [18], which can incur large costs.

Detectors incorporating photocathodes, like PMTs, are also of particular interest due to the sharp cut off due to the work function of the material used for the photocathode, allowing for spectral determination. GPMs just like PMTs use photocathodes and therefore also has this benefit. In PMTs the multiplication stage occurs by accelerating electrons which then collide with a succession of anodes under vacuum which causes secondary electrons to be emitted, wherein the case of GPMs the multiplication stage occurs from the inelastic collisions with the inert gaseous atoms under an accelerating field. Further detail on the processes present in GPMs is discussed

in section 1.4.
GPMs are potentially very useful for large-area, cheap UVC detectors due to their ease of manufacturing. However their lack of stability when approaching high gains and lack of air-stable UV photocathodes have stopped them being more widely used. Although not commercially available, GPMs have played a significant part in High Energy Particle (HEP) experiments such as Ring Imaging CHerenkov (RICH) counters [19], rare-event experiments and cryogenic applications [20, 21].
In this thesis we will attempt to get a handle on the stability and operation of Thick Gaseous Electron Multipliers (ThGEMs) and through coupling with UV photocathodes investigate their use as a GPM and some potential applications.

1.3 Development of the Gaseous Electron Multiplier

The first and most simple type of gaseous detector is the parallel plate chamber [22] consisting of two parallel electrodes held under high voltage bias such that multiplication occurs in the gap. Although this simple structure has intrinsically high rate capabilities and good energy resolution, the exponential dependence on the gap size and sensitivity to defects [23], lead to research into a new branch of detectors called micropattern gaseous detectors (MPGD).
In 1968 a type of MPGD known as multi-wire proportional chamber (MWPC) was introduced by Charpak et al. [24] which caused avalanche multiplication around thin anode wires, due to a high electric field gradient. This detector consisted of an array of wires supported by insulator such as kapton or PCB. The wires were placed under a high voltage bias and a separate anode would have been used to collect the charges.
However, secondary photons and ions produced by ionisation of the gas in the avalanche limited the sensitivity at high rates. This is because the ions produced by the avalanches are slowly collected at the anode which generates a build up of positive space charge, which in turn modifies the electric field. There is also a position sensitivity limitation due to the difficulties in placing and maintaining a distance of less than a few millimetres between the anode wires and mechanical instabilities from electrostatic repulsion for wires above a critical length (about 10cm for 1mm spacing) [25]. Although some research has been done into introducing supports to MWPCs to reduce mechanical instabilities [26, 27], the operation of these devices have been limited due to non-uniform operation due to contact with insulators or glue.
In 1988, Oed et al. [28] introduced a new type of MPGD called the Microstrip Gas Chamber (MSGC) which consisted of tiny metal strips engraved on a thin insulating substrate, the electrodes were alternately biased as anode and cathode. By use of photolithography the electrode spacing could easily be reduced by an order of magnitude and the fast collection of ions by the nearby cathode strips reduced the space charge build up and greatly decrease the rate limitation. However it was found out that polymerization occurred in the gas under sustained avalanche

conditions causing a thin insulating layer to form on the electrodes and discharges caused permanent damage to the delicate electrodes [1].
In 1996, Giomataris came up with a new type of gaseous detector called the micromegas [29]. Unlike previous detectors the multiplication stage occurs in holes in a wire mesh and was coupled with the high-gain properties of parallel plate detectors. The closed geometry of the multiplication stage meant there was less space charge build-up but unlike the MSGCs a lack of thin anodes means they are insensitive to damage from radiation or polymerization. Also they had a naturally low ion-backflow fraction (IBF) due to the ions being caught in the mesh [30].
Finally in 1997, Sauli et al. [31] introduced the Gaseous Electron Multiplier (GEM), these devices consist of a dielectric sandwiched between two electrodes with holes drilled or etched through the device. As in the case of the micromegas the avalanche was confined to holes, however the photon and ion-mediated effects are further reduced as they will be absorbed into the dielectric walls of the holes.

The GEM also has the unique property of being able to share the overall gain needed in a

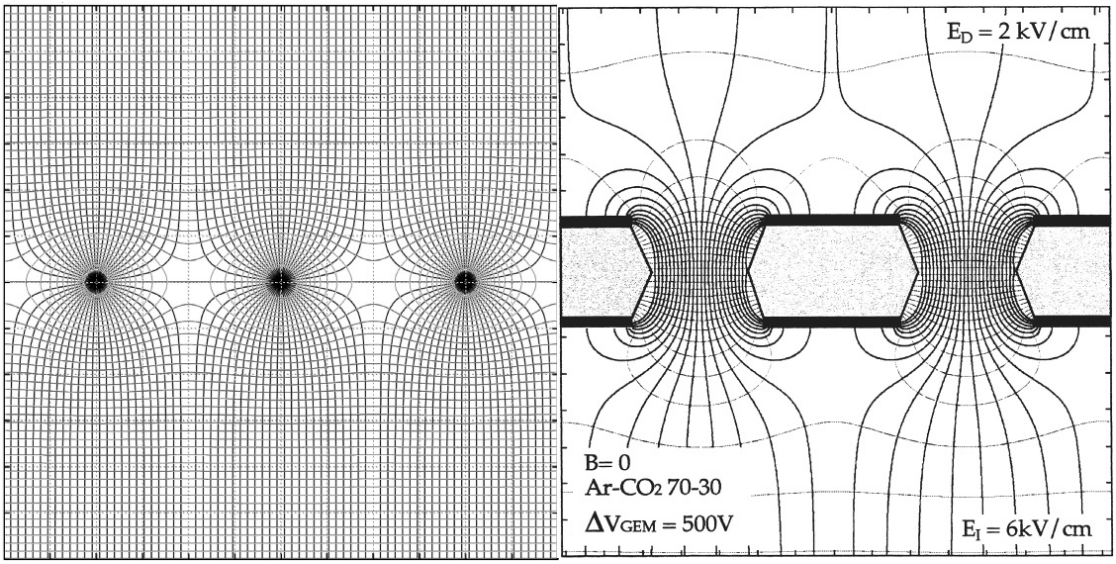

(a) (b)

Figure 1.1: A model of the electric field lines for a) Multiwire proportional chamber & b) Gaseous Electron Multiplier, both images are taken from Sauli et al. [1]

cascade of elements operated at lower voltages, this reduces the occurrence of discharges and improves stability and reliability. Another advantage of GEMs is that they are cheap and easy to manufacture and can easily cover large areas with minimal difficulty.
There has also been considerable research reducing the ion IBF via novel GEM/ThGEM structures. Lower IBF values means less damage or ageing of the photocathode by ion impact [32] or sporadic discharges to cathode-excitation effect, particularly at high rates [33]. Also in Time Projection Chamber (TPCs) the space-field distortion induced by the ion migration to the drift volume can cause significant loss of event topology [34]. IBF can be lowered by cascading

GEM/ThGEM elements or even further IBF reduction has been achieved by staggering the hole alignment between multiplier elements [35]
Hybrid MPGDs with both GEM and MSGC elements were introduced by making lithographic patterned electrodes for ion defocusing. Such as the Micro-Hole Strip Plate (MHSP) [36], COBRA [37] and Thick-COBRA [38]. An IBF as low as $10^{-4}\%$ at a gain of 10^5 was reported for 2 GEMs sandwiched between 2 COBRA multipliers [39].
More recently, multi-layer ThGEMs have been investigated by Cortesi et al. [40]. Further improvement to this design was made by Olivera et al. [39] by merging the double micromegas with its large gain with the more robust multi-layer ThGEMs, coining a Multi-Mesh Thick Gaseous Electron Multiplier (MM-ThGEM). In this device two micro-meter meshes are laminated in between two ThGEM elements. This causes efficient focusing into the holes, natural ion and photon suppression, coupled with the amplification of the strong uniform electric field in the small gap between parallel meshes. Also due to the large field gradient between the amplification region and the pre-amplification region the ions produced in the avalanche and from below are trapped on the uppermost mesh reducing the IBF.
Although more complex GEM devices exist, in this thesis we will, in general, compare the general properties of a single ThGEM device. However the general properties of this device should also be similar to the other types of GEM devices.

1.4 Gaseous Electron Multiplier Theory

Gaseous ionisation detector operation can effectively be broken into 4 stages:

1. Production of primary electrons
2. Drift and acceleration of electrons and ions
3. Multiplication of electrons via successive collisions
4. Charge collection and amplifications

The production of primary electrons can be either from direct ionisation of the surrounding gas or by emission from a solid surface via the photoelectric effect, discussed in more detail in section 1.5.
The primary electrons produced then experience a drift and acceleration due to the electric field caused by a high voltage bias placed across the electrodes of the detector. These electrons are accelerated to the point where successive ionisation occurs with the surrounding gas resulting in production of secondary electrons that are subsequently collected and measured.

1.4.1 Ionisation Multiplication

The first effect we will describe in more detail is the multiplication of electrons in the gas, the primary electrons are accelerated due to the resultant electric field in the device. Once the electrons are accelerated to a point where they have kinetic energy higher than the ionisation potential of the gas atoms or molecules they can cause an ionisation collision producing another electron, which in turn can be accelerated into another ionisation collision if it is not absorbed into the walls of the detector. If the inelastic mean free path (IMFP) is much smaller than the multiplication length, the process repeats itself causing a chain reaction forming an avalanche of electron-ion pairs, known as a Townsend avalanche, first discovered by Townsend in 1901 [41]. At these energies, the main loss of energy is via inelastic collisions such as excitation and ionisation and the contribution of elastic processes becomes negligible. Due to the large difference in mobility between electrons and ions a characteristic drop-like charge distribution forms with the electrons at the front and the slow ions forming a trail behind.

For a uniform electric field the total multiplication from the Townsend avalanche is of the form in equation 1.1,

$$M = \frac{n}{n_0} = e^{\alpha x} \tag{1.1}$$

where n is the number of final electrons after multiplication, n_0 is the number of primary electrons produced and α is the inverse mean free path for ionisation otherwise known as the 1st Townsend coefficient also defined as $\alpha = N\sigma_i$ where N is the number of molecules per unit volume and σ_i is the ionisation cross section. This coefficient therefore represents the number of ionizing collisions per unit drift length.

The Townsend coefficient, α, depends on the electric field strength and gas pressure. Many analytical expressions for α exist [42]. The generalised form of the Townsend coefficient is shown in equation 1.2,

$$\frac{\alpha}{P} = Ae^{-\frac{BP}{E}} \tag{1.2}$$

where A and B are phenomenological constants. For Argon, the values of $A \approx 14\text{cm}^{-1}\text{torr}$ & $B \approx 180 Vcm^{-1}\text{torr}^{-1}$ are given by Sauli et al. [43]. However, due to the double exponential dependence of the electric field on α, large errors can occur for even small differences in the parameters used.

Figure 1.2 taken from [43] shows the experimental data for the Townsend 1st ionisation coefficient from Kruithoff and Penning [44] and Jeleneak et al [45] compared to the general approximation from equation 1.2 and calculation by Sauli et al. [43] using a program called MAGBOLTZ for Argon at NTP.

For non-uniform electric fields the acceleration of the electron changes as it drifts through the detector therefore the Townsend coefficient will also change. A simple approximation would be to split the field into infinitesimal slices and integrate across, such that $M = e^{\int \alpha(x)dx}$. However this method produces large errors in fields with large space gradients due to the fact that the values for Townsend coefficient at a specific electric field strength are measured under uniform

electric field [46].

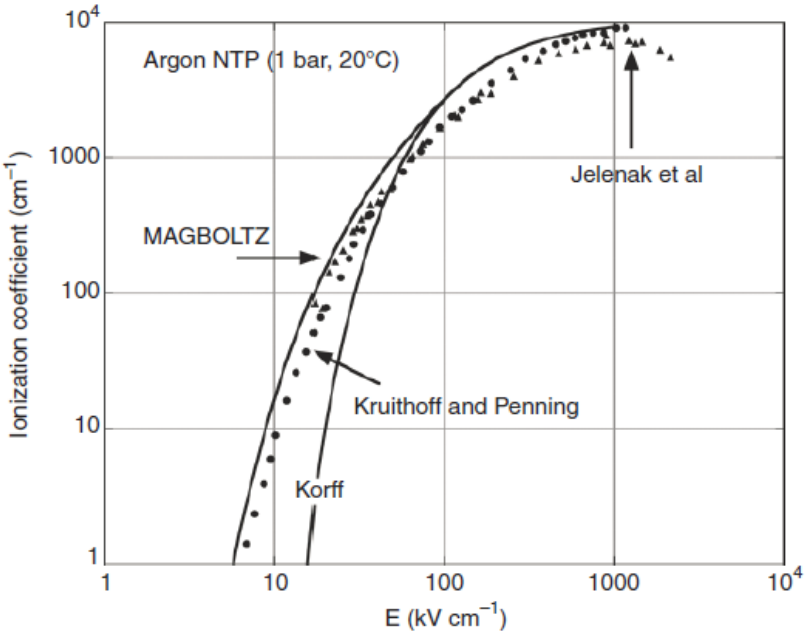

Figure 1.2: Comparison of experimental data to Korff's approximation and MAGBOLTZ calculation for Argon at NTP taken from Sauli et al. [43]

1.4.2 Excitations and Secondary Photon Emission

A large number of processes can occur during inelastic interactions between electrons and molecules. As well as ionisation, collisions with the atoms can cause excitation leaving an atom in an excited state which can then de-excite via numerous processes. Noble gases in particular can de-excite via emission of DUV photons. DUV emission can be produced via decay of excimers that are produced via collisional excitation between excited and ionized atoms. Figure 1.3 shows the emission from argon excimers as measured by Hurst and Klots [47]. The lower wavelength emission (105nm) dominates at low pressure corresponding to the emission from de-excitation from short-live molecules called dimers, whilst excimer emission peaks at around 125nm. Other photon emission can occur via atomic emission in the visible and infra-red regions however these are not as intense. It is generally believed that DUV emission dominates over other types of radiative decay at high pressures [48].

If the photons have enough energy to ionise the gas they can cause secondary avalanches and even eventually lead to a dielectric breakdown or spark. As such, in proportional counters such as MWPCs, it is common to use a mixture of noble gas and a molecular gas called quenching gas, CH_4 and CO_2 are some commonly used quenching gases used in gaseous detectors. These molecular gases de-excite via vibrational and rotational modes instead of radiative therefore they

suppress the effects of secondary emitted photons on causing spark breakdowns. However, the use of quenching gas is less important in GEMs due to its avalanche containment in the closed geometry of the holes which limits secondary effects from photon emission. Therefore even though pure noble gases are generally not used in MPGDs, GEM operation in pure noble gases is possible. The use of pure noble gases without molecular gases also reduces the ageing effects of photocathodes which is particularly useful for detection of visible light due to the delicate nature of visible photocathodes [49].

Addition of even small amounts of other species to noble gas shifts the excimer emission to

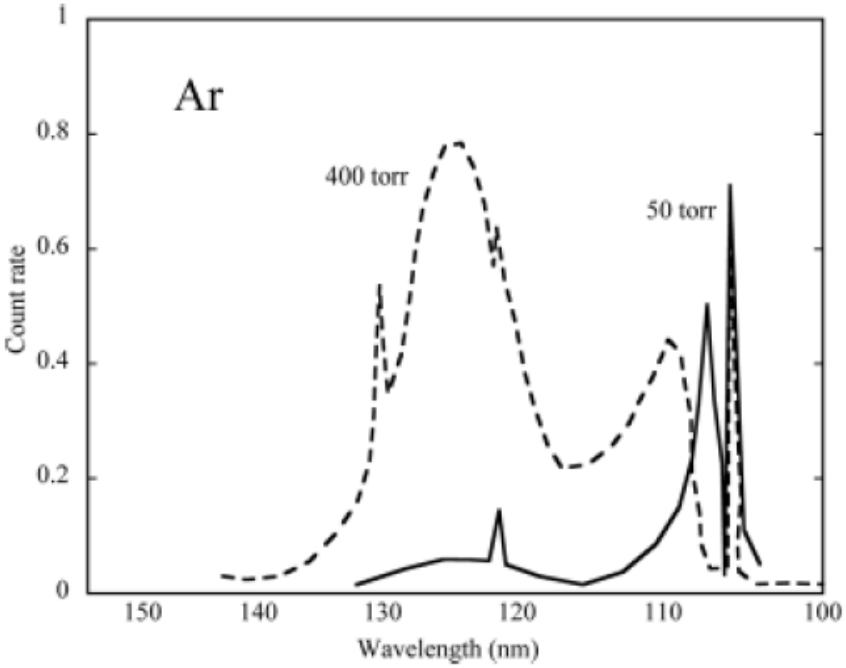

Figure 1.3: Fluorescence emission of Argon excimers from Hurst and Klots [47]

longer wavelengths towards that of the additive as shown for argon-xenon and argon-nitrogen in Takahashi et al. [50], where nitrogen shifts the secondary emission to the visible reducing the chance of a breakdown to occur from secondary photon emission.

Another important process that can occur if the ionization potential of one of the gas species present in the mixture is lower than the excitation potential of the other is a very effective process of collisional transfer called the penning effect, $A* + B \rightarrow A + B^{+} + e^{-}$. This effect increases the number of ionised states that leads to a very effective increase in the ionisation yield as shown by Druyvesteyn and Penning [51]. Mixtures of these gases are called Penning mixtures and are widely used in proportional counters to improve energy resolution [52].

1.4.3 Induced Charge

As ions and electrons drift towards to the electrodes the surface charges change, the cathode towards more negative and anode to more positive values. The signals detected on the load resistor however are opposite in polarity. Therefore in the ThGEM device, as the electrons drift towards to the negative plate the detected signal will be positive.
The instantaneous charge induced on an electrode by a drifting charge can be simply calculated using the Ramo Theorem [53] shown in equation 1.3,

$$i = E_w e v \tag{1.3}$$

where E_w is the weighted electric field, in which the electrode in question is placed at unit potential and all other electrodes are grounded and i is the instantaneous current flowing in a given electrode due to the motion of a single electron of velocity v.

1.4.4 Streamer Formation and Breakdown

In the avalanche the high density of ions and electrons cause the electric field to be modified, increasing its strength in front and behind the avalanche. Photons emitted from the avalanche can cause secondary avalanches to develop in these regions of higher field, this process continues in front and behind the original avalanche causing a streamer to form. If not damped by detector geometry, quenching gas, or a reduction in the field strength; the streamer can propagate across the whole gap leading to a spark breakdown. Precise modelling of the avalanche to streamer transition (AST) requires precise detail of electron and ion kinematics which are dominated by collisions with the background gas and the interaction of the particles via their own space charge field [54].

Avalanche to Streamer Transition

A widely used criteria used for AST, known as the Raether limit [55] is shown,

$$Q_{crit} = M_{max} n_0 \approx 10^6 - 10^7 e \tag{1.4}$$

this equation is a simplified assumption that assumes the transition occurs when the amplitude of the space charge field becomes comparable with the background electric field. However, in practice spark breakdown occurs at multiplication values and avalanche sizes much lower than this value. The actual value of Q_{crit} (the critical charge accumulated before spark breakdown) depends on several factors such as: geometry and density of primary electron cloud, number of original electrons (n_0), detector geometry, burrs or residual material from fabrication and electron, gas composition and pressure, and ion diffusion.

Currently no comprehensive model is available that gives an overview of the AST for different gas species, ambient pressures and electric field strengths [54]. Also as AST often occurs in strongly inhomogeneous background fields (i.e. close to sharp tips, burrs or rough surfaces) the AST can only currently be evaluated on a case-by-case basis.

Feedback Effects

When operating with poorly quenched gases the maximum achievable gain may also be restricted by the fraction of ions that reach the cathode also known as the ion backflow fraction (IBF). A common limit used is $\gamma M_{max} k = 1$ [56], where k is the fraction of ions or photons that reach the cathode and γ is the probability of production of an electron from the cathode due to photon (γ_{ph}) or ions (γ_{+}) at the cathode. γ_{+} has been shown to be linearly proportional to ionisation potential of the gas and γ_{ph} is a sharply increasing function of photon energy (mostly due to a sharp increase in QE at the photocathode) [57].
The photon feedback is particularly bad for highly efficient photocathodes (i.e. low work function and high QE). This is the reason that classical gaseous detectors such as MWPC, which have a large IBF (≈ 1), have a maximum achievable gain which is very low when coupled with photocathodes. Whereas in the case of the GEM the cathode is geometrically shielded from direct light emitted by avalanches so the feedback is almost entirely from ion feedback. Also as mentioned earlier in section 1.3 there are more novel designs that further reduce the IBF. This allows GEMs and similar devices to operate at higher voltage biases and electric fields than MWPCs in badly quenched gases, including noble gases.
It is also noted that the cleaner the noble gas the smaller the maximum achievable gain is. Galea et al. [58] showed practically no gain for ultraclean He & Ne. This is due to the fact that the mean free path of noble gas ions before experiencing charge transfer is very large, so at some level of cleanliness the majority of the ions reach the cathode.

Counting Rate Limitation

It is well known that the maximum achievable gain also decreases with increasing counting rate [57]. This can be viewed as the statistical likelihood of avalanches overlapping forming space-charge field which can subsequently cause a spark breakdown. There is also other mechanisms that contributes to the counting rate gain limitation known as 'electron jets' or the 'cathode excitation effect'.
The so called cathode excitation effect was demonstrated as temporary enhanced value of γ_{+} & γ_{ph} after a discharge [59]. The explanation of which is most likely from positive ions deposited on thin dielectric films, either caused by polymerisation of the surrounding gas, oxidation of metal or adsorption of thin layers. The ions will create extremely high electric fields, similar to the more well known 'Malter effect'. These electric fields then cause electrons to be ejected

from the films in form or bursts of jets after some accumulated time [60].

1.4.5 Gain Stability

Charging of Dielectric

It is well known that hole-type gaseous multipliers suffer from gain variations due to the charging up of the dielectric surface due to the impinging free charge carriers and polarization of the dielectric [61]. It was expected that stability will be reached when the charge accumulation and charge evacuation reach an equilibrium.
Alexeev et al. [62] argued that the charges move within the PCB along the electric field lines and this is a slow process meaning an asymptotic gain stabilisation is reached anywhere from several hours or days. For cylindrical holes it is expected that lateral diffusion of the charge carriers will result in electrons occupying the lower part of the hole and positive ions will occupy the upper part of the hole. This should create an electric field that opposes the original bias, decreasing the overall gain.
However, it has been shown that for most GEMs/ThGEMs there is a long term rising behaviour present which appears to be in direct opposition with the decrease in gain due to lateral diffusion of the charge carriers following the original field lines. Also of interest is that Azmoun et al. [63] found that the % initial gain increase was exponentially proportional to the exposed surface area of the dielectric, via so called 'rims' around the holes. It was shown that films with a large initial rising effect were also drastically effected by the amount of water in the chamber, which could be explained via a modification of the surface conductivity of the exposed dielectric material on the surface.
Pitt et al. [64], through simulation and measurements showed that for ThGEMs with etched rims there also existed a long term gain variation with the short term drop due to the charging up of the hole walls.
It was suggested that the top rim charges negatively due to part of the primary electron cloud that is not focused into the holes resulting in a rise of gain over much longer time scales than the charging up of the dielectric (order of few hours). And conversely the bottom rim charges up positively due to collection of ions after the multiplication stage, as this happens about the same order as the charging up of the hole walls it results in simply a smaller drop over the short period. This is shown in figures 1.4*a*, 1.4*b* and 1.4*c*, taken from Pitt et al. [64] showing the 3 different cases in the simulation of charging process (no rim charging, bottom only and top and bottom rim).
Pitt et al. [64] also showed that for a negative induction field, where all the ions are collected at the bottom electrode the bottom rim charges up quicker resulting in an initial rise in gain followed by a drop as the hole walls finish charging up.
The ratio of the long-short term stabilization time was found to increase with increasing drift

field values as more electrons are collected on the top ThGEM electrode.

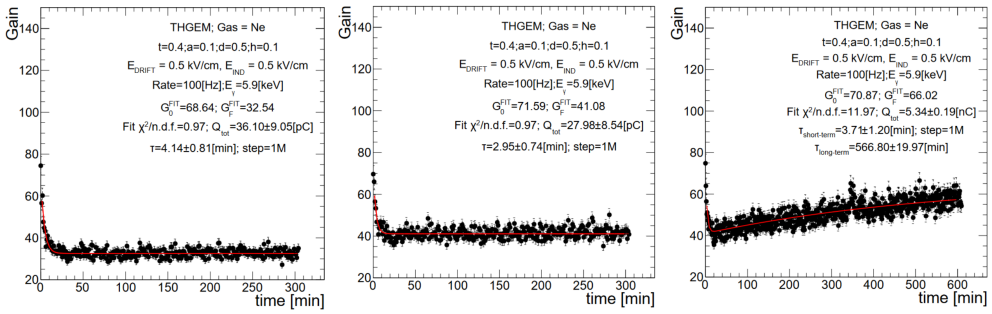

(a) (b) (c)

Figure 1.4: Simulation of gain stability taken from Pitt et al. [64] for a) no charging up of etched rims b)only bottom rim charging and c)top and bottom rim charging

Gaseous and surface Impurities

Another effect that can cause a rising behaviour in the gain is changes in the levels of impurities in the gas. This has been experimentally shown by Cortesi et al. [65] where a 2-fold reduction in the charging up of gain was found over a period of 6 hours when comparing measurements started immediately after pumping and those started after prolonged gas flow (24 hours). It was concluded this was due to a reduction in the impurities in the chamber after this period of flushing through with gas.

1.5 Photoelectric Effect

As mentioned in the previous section, the first process in gaseous ionisation detectors is the production of primary electrons. In standard gaseous detectors, primary electrons are created through direct ionisation of the surrounding gas via radiation. However, for GPMs, the primary electrons are produced via the emission of electrons from a material (known as a photocathode) under illumination of photons, this effect is commonly known as the photoelectric effect.
Photocathodes can either be reflective (electrons are emitted in the opposite direction of the incident photons) or semi-transparent (electrons are emitted in the direction of the incident photons or through the photocathode). For our purposes we have deposited films onto the top electrode of our detectors and therefore these photocathodes are used as the reflective type.
The photoelectric effect is a phenomenon where an electron is ejected from a metallic or semiconducting surface via absorption of one or two photons. The electron is only emitted when the photon energy exceeds a threshold called the work function of the material. Therefore the maximum kinetic energy that the photon can receive is $K.E_{max} = hf - \phi$ where f is the frequency

of the light and ϕ is the work function of the material.
In 1958, Spicer [66] developed a model for photo-emission, often called the three step model, as it treats the process in 3 distinct steps: optical absorption, electron transport to the surface and escape from the surface to vacuum. In metals the electrons are first excited from the valence to conduction band, these photo-excited electrons then travel to the surface losing some of their energy mainly through scattering with other electrons. If the photoelectron reaches the surface with enough energy, it can then escape the surface barrier and be emitted into the vacuum. The photoelectric yield therefore will be equal to the probability of these three processes: The probability of absorption, which will depend on the density of states in the valence and conduction band; the probability of transmission, which will depend on the photon penetration depth and inelastic mean free path (IMFP) of the photoelectron; and finally the probability of this electron then escaping, which will depend on the height of the surface barrier and the angle of incidence between electron and surface.

1.5.1 Work Function

The work function of a conductor is defined as the minimum energy needed to remove an electron from the bulk to a point outside the material with zero kinetic energy with respect to sample surface, i.e. the difference between the vacuum level (E_v) and the Fermi level (E_F) of a material. The work function effectively gives a cut-off frequency of the photons capable of causing photoelectrons via photoelectric effect.
In semiconductors however, the Fermi level exists somewhere in the bandgap of the material and the actual energy required to remove an electron to from the system, known as the ionisation energy (IE), is actually the difference between the highest occupied valence state and the vacuum energy [67]. In a semiconductor the position of the Fermi level and therefore its work function depends on the density of states, temperature, carrier density and doping concentration.
Work function can be measured directly by applying enough energy for electrons to escape the metal and measuring the electric current. Examples of direct measurement techniques include thermionic emission, field emission and photoelectric effect. Work function can also be measured indirectly via the Kelvin probe method, which will be described in further detail later in section 2.2.
Theoretical calculations using Density Functional Theory (DFT) [68, 69] have been performed with growing success on calculating the work function of materials. For example, Waele et al. [70] have managed to predict accurate work functions of crystalline solids with error bars below 0.3eV.
The work function can be viewed as a combination of two different components, the dominant bulk component which corresponds to the chemical potential that derives from the electronic density and density of states in the solid and the surface component also known as the surface dipole.

In the bulk of a metal the electron density is constant (simple jellium model) however as the lattice abruptly terminates at the surface, electrons can tunnel out the solid at some small distance creating a negative sheet of charges outside the solid and leaving a positive sheet of metal ions at the surface and sub-surface layer. This effectively creates a potential barrier to overcome which increases the work function. Therefore the work function of a metal can vary significantly depending on its crystal orientation [67]. The addition of adsorbates onto the surface can also increase this potential barrier by adding to the surface dipole.

Chapter 2

Experimental Methods

2.1 Growth Techniques

In this section we outline the various experimental techniques used to deposit thin films for use as photocathodes and ultra-thin films used as work function modifiers.

2.1.1 Physical Vapour Deposition

Introduction

Most of the photocathode films in this thesis were grown in vacuum via a simple deposition technique called physical vapour deposition (PVD). In PVD the substances to be deposited are sublimated into gaseous form which then travels through vacuum to the sample surface where it is deposited. There are many different types of PVD, the most commonly used forms being sputtering and vacuum evaporation. The latter is primarily used in this thesis to deposit thin metal oxide films for use as UV photocathodes. Therefore vacuum evaporation will be the primary focus of this section.

Vacuum evaporation is a technique that uses crucibles, tungsten boats, naked wires or electron beam heating to heat and sublimate the source material which then travels through the vacuum to the substrate. Vacuum evaporation has to take place in good vacuum conditions to avoid surface contamination and to have a long mean free path between collisions. Also care has to be taken in placing the sample far enough away from the filament and source to reduce radiant heating of the substrate or another means of cooling the sample needs to be implemented, such as water cooling. Radiant heating from the effusion cell can also deposit other contamination onto the sample surface if the chamber is not clean. In this thesis all growth occurs under vacuum pressures ($< 10^{-6}$mbar).

Experimental Method

Most of the photocathode layers mentioned in this thesis are deposited via a simple thermal vacuum deposition method in a purpose built vacuum system at the University of Warwick. The chamber is separated into two main sections by a gate valve to allow for sample loading and removing without compromising the pressure and contamination in the main chamber, in particular Zn has high vapour pressure at low temperatures meaning that it coats the inside of the chamber and can re-evaporate during other depositions. Figure 2.1*a* shows the chamber with the 2 sections labelled.

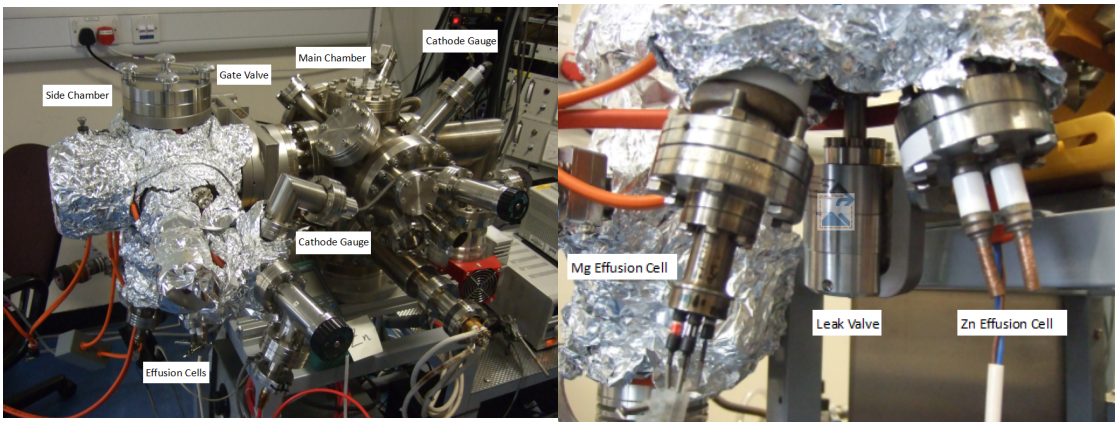

(a) (b)

Figure 2.1: a) Vacuum chamber for PVD b) bottom view of effusion cells and leak valve

Both sections of the chamber have their own turbo molecular pumps and rotary pumps for backing pumping.
Pressure in the chambers is measured by two hot cathode pressure gauges for the two separate sections of the chamber. These gauges use a regulated electron current from a heated filament to measure the pressure in the chamber. Gas ions caused by electron collisions are attracted to a central ion collector wire where the current is measured. Over a wide range of molecular density the ion current is assumed to be directly proportional to the molecular density and therefore the pressure can be inferred from the ion current.
Each material is deposited using their own separate effusion cells, which can allow for rough control of amount deposited of each via measurement of the temperature, using thermocouples. The sublimation of the solid source material happens via thermal evaporation in a ceramic crucible heated by a coil of tungsten wire. After the samples are grown, oxygen is slowly released into the chamber via a leak valve and narrow capillary tube leading to the sample surface. A narrow tube is used to direct the oxygen to the sample to minimise the oxidation of the tungsten filaments (both around crucibles and on ion gauges), whilst maximising the oxidation at the sample surface. Also on the gas line is a line to vent the side chamber with pure nitrogen for sample removal. Figure 2.1*b* shows a more detailed view of the bottom of the side chamber

showing both effusion cells and leak valve which allows oxygen into the chamber.

Evaporation Rate

The evaporation rate of a sublimated material in vacuum can be calculated using the Hertz-Knudsen vaporisation equation [71] as shown in equation 2.1,

$$\frac{dN}{dt} = Csqrt2\pi mKT(p^* - p) \tag{2.1}$$

where dN is the number of evaporating atoms per cm^2, C is a constant that depends on rotational degrees of freedom in vapour, $p^*$is the vapour pressure of the source material and p is the pressure above the surface. Maximum evaporation rate is when $p = 0$ and $C = 1$ however the actual vaporisation will be a third to tenth of this maximum rate due to collisions, surface contamination and other effects.
Using this equation if we know the temperature and vapour pressure of the material in question we can get an estimation on the vaporisation rate onto the substrate.
For low vaporisation rates, and ignoring collisions within the path to the sample, the flux distribution as from a point source can be described by a cosine distribution as shown in equation 2.2 [71],

$$\frac{dm}{dA} = \frac{E}{\pi r^2} cos\phi cos\theta \tag{2.2}$$

where E is the total mass evaporated, θ is angle from the normal to the vaporising surface and ϕ is the angle from the source to a point on the surface.
In general, to measure the vapour pressure of various gases a Knudsen cell is used, this cell consists of a closed volume with a small orifice, when the container is held at constant temperature the material that escapes through the orifice depends on the pressure differential [72].

2.1.2 Electrochemical Deposition

Introduction

Electrochemical deposition is a method in which a solid metal film can be deposited on an electrode submerged in an electrolyte solution, containing metal salts and other ions to promote current flow through the solution. A DC current is applied between the anode and the cathode (the electrode to be coated) and at the interface of the cathode and solution the metal ions reduce and cause a precipitation on the surface. This method was mainly used as a comparative method to PVD in this thesis as there is limited data for the deposition of films using this method. Electrochemical deposition does not require vacuum conditions and therefore can be a significantly cheaper and faster method of fabrication of thin films than PVD or molecular beam epitaxy.

An electrochemical cell usually consists of three separate electrodes submerged in the electrolyte solution: reference, counter and working. The working electrode is the name given to the electrode that the film is deposited on (i.e. cathode), in our case this is the ThGEM. The counter electrode is normally made of inert material such as platinum, gold or graphite so that it does not take place in the actual chemical reaction. The current is applied across the counting electrode and the working electrode. Finally, the reference electrode is the point of reference for potential control and measurement. The reference electrode must have stable and well-known electrode potential, this is normally achieved by employing a redox reaction where the participants in the reaction are constant (i.e. by saturation). The current flow through the reference electrode is kept close to 0 via high input impedance to the potentiostat. Also, to reduce ohmic losses in the solution, known as the Luggin-Haber capillary effect, the reference electrode is brought as close as possible to the working electrode.
A potentiostat is used to control the potential and measure the current. The potential between counter and working electrodes is adjusted so that the potential between the working electrode and reference electrode is kept at a value set by the software. The current is then measured from the counting electrode.

Experimental Setup

The setup used in our experiments matches closely that used in Illy et al. [73]. 3 electrodes were submersed in the electrolyte solution: The reference electrode of Ag covered with AgCl, the counter electrode of platinum wire and the working electrode (the sample to be coated). The ThGEMs, or working electrodes, had the connection soldered to the copper connector in the design, which was left out of the solution so it did not contaminate the ZnO layer deposited. To manipulate the electrodes and their amount of submergence in the electrolyte solution a set of mini-stands with crocodile clips were used. The potential was controlled by a potentiostat from Palmsens and the corresponding software that came with it.
The electrolyte solution was made by dissolving 0.1M $Zn(NO_3)_2$ and 0.1M KCl in a solution of deionised water. 0.1M $Zn(NO_3)_2$ was used to match the standard conditions in Illy et al. [73] as the ZnO films were shown to have peak optical transparency for this concentration [74].
In this method a precursor of NO_3^- is used via dissolving zinc nitrate hydrate in solution of water and KCl. NO_3^- has been used as it has high solubility in water and very high deposition rates can be obtained [75]. The steps of the reduction process at the cathode leading to precipitation of Zn on the surface of the cathode is shown in equation 2.3.
Deposition was performed at room temperature and with a potential of -1V as again this was shown to give maximum optical transparency [76]. The pH of the solution was not measured or controlled.

$$\begin{aligned} NO_3^- + H_2O + 2e^- &\rightarrow NO_2^- + 2OH^- \\ Zn^{2+} + 2OH^- &\rightarrow ZnO\downarrow + NO_2 \end{aligned} \tag{2.3}$$

2.1.3 Spin Coating

Introduction

To coat ultra-thin films for work function modifiers we used a simple technique called spin coating. This technique works by dropping liquid onto the sample surface and spinning the sample at high speeds (up to 5000rpm). The centrifugal force combined with the surface tension of the solvent pulls the liquid across the surface, producing uniform and consistent films.
The desired molecule is dissolved in a solvent which carries this molecule across the substrate surface, the airflow from the spinning motion then dries a substantial part of the solvent and the remaining liquid can be dried post-process by drying with a nitrogen gun or annealing.
Meyerhofer et al. [77] outlined a treatment which split spin-coating into 2 processes: one from the viscous flow across the sample surface and other from evaporation of the solvent solution. Using this approach the thickness of the final coating was predicted to depend on a variety of key parameters as shown in equation 2.4, where e and K are evaporation and flow constants defined in equations 2.5 and 2.6,

$$t = x\left(\frac{e}{2(1-x)K}\right)^{1/3} \tag{2.4}$$

$$e = C\sqrt{\omega} \tag{2.5}$$

$$K = \frac{\rho\omega^2}{3\eta} \tag{2.6}$$

x is the effect solid content of the solution, ω is rotation rate, ρ is the density of the solution and η is the viscosity. C is a constant that depends on whether the airflow above the sample surface is laminar or turbulent and on the diffusivity of solvent molecules in the air. C has been determined experimentally using laser interferometry [78].
Spin coating is a quick and cheap method of coating thin, reliable and uniform films. However it is often not used for manufacturing processes due to substantial waste of solvent from being flung off the substrate, also it is inherently a single substrate process and therefore has lower throughput than roll-to-roll processes.

Experimental Setup

A programmable spin coater from Ossila was used to coat films onto the ThGEMs. A chuck with a cutout which had the standard dimensions of the ThGEMs was used to hold the sample in place. The liquid was then dropped by hand using a pipette through a hole in a screen above the

sample and chuck. Solvent is dropped onto the sample surface once the device has reached the speed required for deposition, this method is normally called 'dynamic'. Dynamic dispensing is normally preferred as it is a more controllable process due to the fact that in 'static' dispensing (solution dispensed onto a stationary surface) the solution has had time to evaporate before the sample is spinned.

2.2 Kelvin Probe

2.2.1 Introduction

The Kelvin probe (KP) is a device which uses the Kelvin method, introduced by Lord Kelvin in (1898), to measure the contact potential difference between two conductors.
When two conductors are brought into electrical contact, free electrons flow from the conductor with higher Fermi level to the conductor with the lower Fermi level until equilibrium is reached and their Fermi levels are equal. As such the end of the conductor with higher Fermi Level builds up positive charge and the other conductor builds up a negative charge, the potential difference formed between these two conductors is called the Contact Potential Difference (CPD) which is equal to the difference in work function of the two materials.
However, it is not possible to measure the CPD directly by adding a voltmeter as it would end up measuring the sum of the voltages around the circuit which would inevitably add up to zero. As such an indirect method, such as used in the Kelvin probe, is required to measure the CPD.
Figure 2.2 shows a schematic diagram of the 'null' Kelvin method. In (a) two conductors with two different Fermi levels ($E_{fs}\&E_{ft}$) and work functions ($\phi_s\&\phi_t$) are shown. When the conductors are placed in electrical contact, in (b), a current flows from one conductor to the other creating a contact potential difference (V_{CPD}). A backing voltage is then applied which can be measured, this will be equal and opposite to the contact potential difference.
The Kelvin probe (KP) works by forming a capacitor device with a tip suspended above the sample to be measured, this forms a parallel plate capacitor between the 2 surfaces. By then periodically vibrating the tip above the sample surface it causes an alternating voltage to be generated across an external resistor, due to the change in capacitance ΔC, as shown in equation 2.7,

$$V_{ptp} = (V_{CPD} - V_b)RC_0\omega\varepsilon sin(\omega t + \theta) \tag{2.7}$$

where V_b, the external backing voltage is then applied until the voltage drop across the external resistor is 0, then this voltage would be equal but opposite in polarity to the CPD between the materials. This is known as the 'null' method.
The Kelvin method, however, only gives the CPD and not the individual work functions of the materials. Therefore, to determine the work function of samples measured, the tip's work func-

tion must first be determined. The calibration of the tip is discussed further in section 2.2.4 below.

In the case of measuring the work function of semiconductors however, there are additional mechanisms involved in the metal-semiconductor junction between the tip of the Kelvin probe and the semiconductor surface. With semiconductors there is surface band bending of the Fermi level to achieve alignment of the bulk Fermi levels, which can affect the measured work function. Also illumination of samples can cause photo-generated carriers to reach and neutralise surface donors/acceptors which can reduce band bending at the surface causing changes to work function, this effect is called surface photovoltage (SPV) [79, 80].

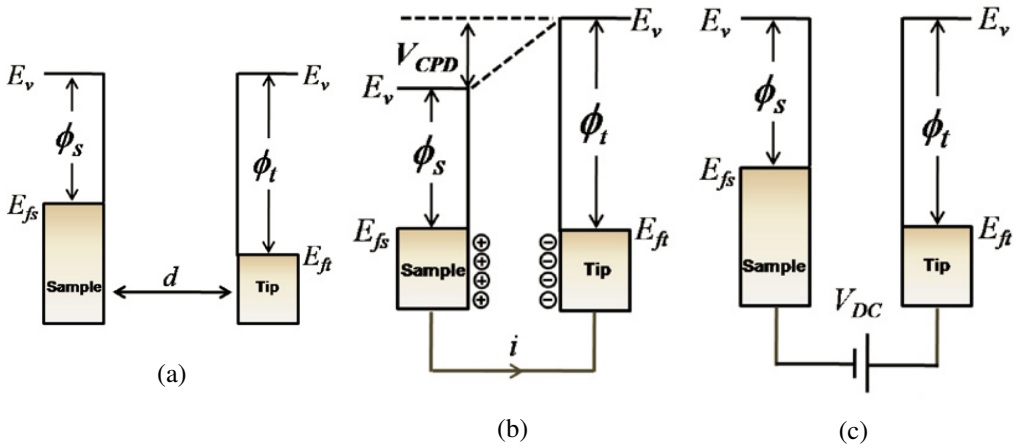

Figure 2.2: Schematic diagram of the 'null' Kelvin method.

2.2.2 Limitations and Benefits

The work function as measured via the Kelvin method is extremely surface sensitive and also sensitive to gases or adsorbed species as they can substantially change the energy required to remove an electron from the Fermi level, this is especially true for metal oxides [81].

Compared to direct measurements of work function via thermionic, field or photoemission; KP work function measurements are often higher because they take the arithmetic mean work function under the probe area. Whereas direct methods are weighted to patches of lower work function. In particular the photoemisson of semiconductors is sensitive to the topmost populated states of the valence band and the work function measured via direct measurements such as photoemission is often lower than the work function measured via the Kelvin probe.

Also surface dipoles may exert a far lesser influence on the measured work function using the Kelvin method compared to photoemission measurements. As photoemission measurements depend on the inside dipole electric field compared to the much weaker outer field of the dipole as in the case of the Kelvin method. [82]

2.2.3 Experimental Setup

The probe is mounted above the sample surface with a moveable clamp, with a adjustable y stage, which can be adjusted to bring it towards or away from the sample. The tip of the probe is coated in gold and has a flat surface of 2mm diameter. As the measurements are performed away from any walls the stray capacitance effects that often dominate measurements are no longer an issue [83, 84]. A screen is also used to minimise the electromagnetic pick-up noise present.

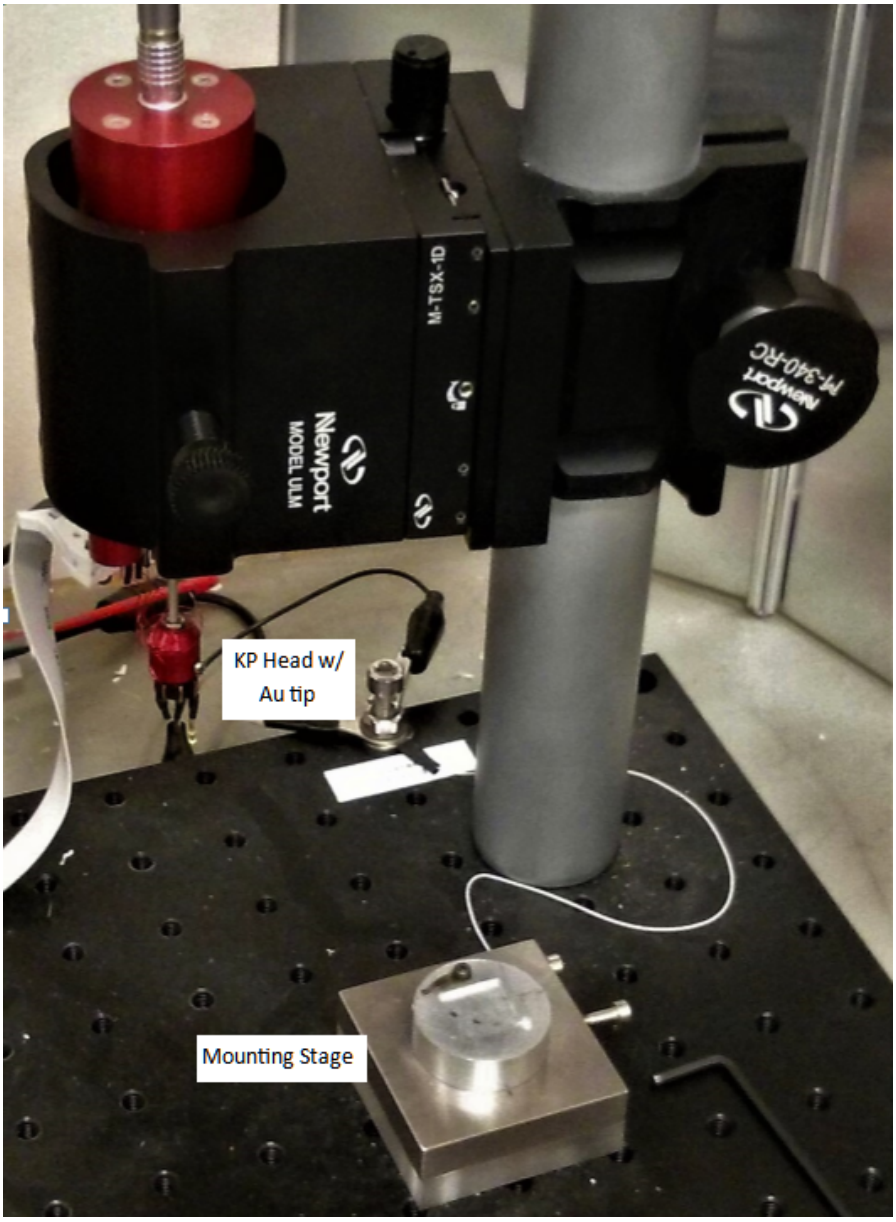

Figure 2.3: Experimental setup of Kelvin probe, with holder with beryllium clip for mounting ThGEMs for measurement

The Kelvin probe came with a sample holder as standard which is electrically grounded. As

some of the surfaces we will be measuring exhibit insulating properties such as MgO and ZnO both of which are wide band-gap insulators, a separate table was retrofitted to sit within this holder and have a top contact via a beryllium clip to ensure electrical contact and remove drifting capacitance effects during measurement.
The Kelvin probe uses a variation on the 'null' method discussed above called the 'off-null' method. The off-null method uses the linearity of the measured signal with the backing voltage (V_b) and uses curve-fitting procedures to extrapolate the intersection with the V_b axis to get the CPD [85]. This method reduces the noise, as at the 'null' point the signal to noise (S/N) ratio reaches a minimum. The 'off-null' method also has the added advantage of allowing measurements of mean capacitance which can be used to allow repeated measurements at the same experimental parameters.

2.2.4 Calibration

As stated previously the Kelvin probe measures the contact potential difference or CPD, not the absolute work function of a material. To convert the CPD into a value of work function, the work function of the tip is required and must first be measured. Possible methods of calibration of the tip work function are: To use an electrochemical half-cell as proposed by Hansen & Hansen [86], finding the photoemission threshold using fowler's theory [87] or to use a reference sample with known and stable work function to infer the work function of the tip.
As the measurements from the Kelvin Probe, in this thesis, are performed in air under ambient conditions, the work function of the samples can vary significantly from absorption of oxygen, water and other surface contaminants. Therefore finding a reference material with a known work function can be difficult. One such material is highly-ordered pyrolytic graphite (HOPG) which has been shown is stable in air with a work function of 4.475 ± 0.005eV, by Hansen & Hansen [86] with comparison with an electrochemical half-cell.
As such to calibrate the tip work function we use a selection of reference samples, including HOPG and use the CPD measured to make an estimate on the tip work function from literature values for the different materials. The different reference materials used were polycrystalline Au, Ag & Al with freshly cleaved HOPG.

Material	CPD(mV)	Photoelectric WF (eV) [88]	Kelvin WF (eV)
Au	130 ± 15	4.8	5.45[89]
Al	-995 ± 18	3.58	4.25 [90]
HOPG	-97 ± 18	4.79	4.475 [86]
Ag	-16 ± 9	4.59	4.3 [91]

Table 2.1: Calibration data for Kelvin probe: Au and Al samples came from aluminium reference table, half coated with gold film, from KP technologies. Ag measurements are taken from silver paste screen printed on ceramic substrates.

Table 2.1 shows the average CPD measured using the KP for all the reference samples and the corresponding values found in literature. Baikie et al. [88], used Fowler's Theory [87] with ambient pressure photoemission spectroscopy to extract the photoelectric threshold from the photocurrent measured from atmospheric ions.
The threshold values from Baikie et al. [88] might not be exact as we cannot assume surface layers such as oxides obey Fowler theory and the CPD measurements across the literature can vary significantly due to surface conditions, effect of absorbants such as water and O_2 and the intrinsic error in determining the work function of the tip. Therefore we will use both values to attempt to get an accurate value for the tip work function.
Taking the values of WF from literature shown in table 2.1 and the measured CPD values for our reference samples, we can now estimate the work function of the tip. Figures 2.4*a* and 2.4*b* show the estimated WF using the threshold values from Baikie and work function measured by Kelvin probe from various sources, respectively. This gives a mean value of 4.68 ± 0.07 eV and 4.9 ± 0.2 eV for figures 2.4*a* and 2.4*b* respectively. We will use the weighted mean value of 4.7 ± 0.07 eV as the tip work function for the rest of the thesis.

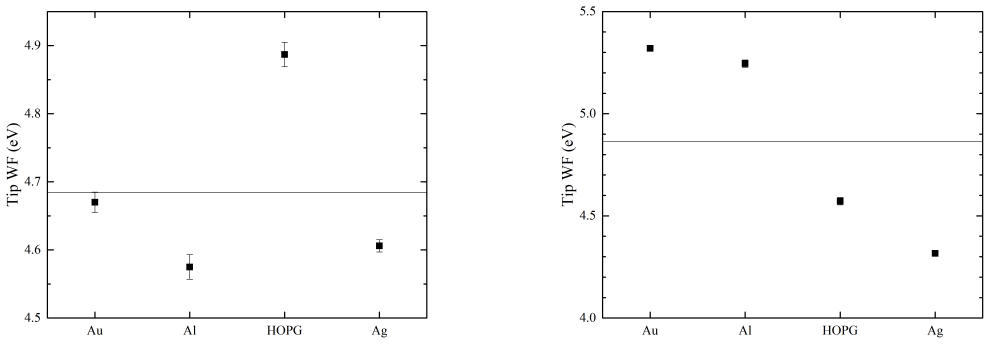

(a) (b)

Figure 2.4: Estimated Tip WF from a)Photoelectric Threshold values and b)Surface WF as measured by Kelvin probe

Table 2.2 shows the measured work function for the calibration samples using this tip work function. For most of the samples the WF measured using this tip WF is quite similar to the photoelectric threshold from Baikie et al. [88], except HOPG which matches more with the WF measured by KP in Hansen et al. [86]. This futher illustrates the problem with using only HOPG as a source for calibration in ambient conditions.
It can be seen that the dominant source of error is the determination of the tip work function from the literature values (0.07eV) as the measured average CPD values for the reference sample have a much smaller error. However for comparative measurements things such as the variance across a sample and the capacitive effects will be the primary source of error.

Sample	WF (eV)
Au	4.75
Al	3.63
HOPG	4.52
Ag	4.6

Table 2.2: Measured work function for calibration samples using calculated tip work function

2.3 X-Ray Photoelectron Spectroscopy

2.3.1 Introduction

X-Ray Photoelectron Spectroscopy (XPS) [92] also sometimes known as electron spectroscopy for chemical analysis (ESCA), is a surface analytical method that can investigate the elemental composition of a sample. This method works by measuring the kinetic energy (K.E.) of core-level electrons ejected from the surface via the photoelectric effect after irradiating the surface with X-rays.

If the energy of the X-ray photon is known, then the characteristic binding energy (B.E.) of the core level electron, which was emitted can be calculated from its measured K.E. as shown in equation 2.8,

$$K.E. = E_\gamma - \phi_I - B.E. \tag{2.8}$$

where ϕ_I is the work function of the instrument (the minimum energy required to get a electron from the surface to the detector).

As every element has a specific electronic structure and therefore a unique binding energy of their core electrons (roughly increasing the atomic number (Z)), from the peaks in the measured spectrum, the element that the electron has been liberated from can be inferred. Small shifts in binding energy can occur from the local chemical environment of the element, such as bonding, therefore these shifts can give information of the chemical state that the element is in.

XPS is a very powerful technique for measuring the chemical composition of a surface as it is inherently a highly surface specific method due to the electrons having a small inelastic mean-free path (IMFP), meaning the actual depth that is analysed is much smaller the the photon penetration depth. This can be quite useful as it allows us to look purely at the surface of a material without any interference from the bulk. Also, (ignoring changes to the electronic state of the surface from charging) XPS is also a non-destructive technique unlike other surface composition techniques, such as secondary ion mass spectrometry (SIMS) [93].

Another factor that can change the depth which is measured is the angle relative to the surface of the sample, also known as the take-off angle (θ_T). A common term to define the volume analysed is the sampling depth $(3\lambda_{IMFP}cos(\theta_T))$ which is defined as the depth which 95.7% of the

photoelectrons emanate from. By changing the take-off angle, the depth of study or sampling depth can also be changed, this can be useful to see how the chemical composition changes with depth.
The atoms which the core electrons are emitted from will be left in an excited state, the electrons from the valence band can then decay into the vacancy left by the photoionisation event. This relaxation event can either result in an emission of a photon (fluorescence) or another electron from the valence band, known as an Auger electron. As Auger electrons also have characteristic energies dependent on the atomic transitions, they can also be used in analysing chemical composition of a surface, which is the primary mechanism in a similar analytical method that uses a beam of electrons to excite the surface and emit these electrons called Auger electron spectroscopy (AES) [94]. As X-ray sources usually use relatively low energy photons, the Auger effect will dominate the florescence in relaxation events [95].
If the sample surface is electrically insulating then the emission of electrons under illumination of X-rays can cause a positive charge to accumulate at the surface. This can cause the peaks to shift to higher binding energies and become distorted. To reduce this effect it is necessary to replenish the electrons from an external source such as an electron gun. Any remaining shift in the spectrum can then be removed via charge correction using software, by selecting a reference peak and shifting the B.E to a known value. However charge correction from a reference peak does not take into account differential charging.

2.3.2 Instrumentation

XPS is performed under UHV to improve detection efficiency due to minimising collisions of electrons with surrounding gas, surface contamination and damage to the x-ray source. Also the chambers are often shielded with mu-metal to minimise the effect of external magnetic or electric fields.
Once the electrons are ejected from the material, they are filtered out by their K.E. using an analyser. The type of analyser used in the Warwick Photoemission facility is a Concentric Hemispherical Analyser (CHA) which consists of two concentric hemi-spheres. By applying specific potential to these spheres the electrons can be filtered by the path of their deflection. The spectrum achieved outputs counts per second as function of kinetic energy which can be converted into a binding energy via equation 2.8. Unlike it's counterpart (a double-pass mirror analyser (CMA), which is used in both AES and XPS) CHA allows for depth profiling of the sample by rotation of the sample with respective to the analyser as it has a smaller acceptance solid angle allowing electrons emanating from a single direction to be measured.
The X-ray source used was monochromated Al K_α with emission at 1486.6eV. X-rays are emitted by bombarding the solid Al target with high energy electrons causing a characteristic line emission associated with the filling of core holes created by the electron beam, plus a background due to bremsstrahlung. The emitted x-rays are then subsequently passed through a monochro-

mater so that just a single energy peak (K_α) is sent to the sample, with some intrinsic line width which will limit the broadness of the observed peaks in the spectra.

2.3.3 Peak Fitting and Analysis

First step in analysing the surface chemistry of a sample is to find the peaks present in the spectra received and find which elements they belong to from the background. The stepped background in the XPS spectrum is mainly due to secondary electrons, which have been inelastically scattered causing them to have lower kinetic energy. This background has to be subtracted before peak area can be determined, various functions are used to remove this background. In most of the fitted data in this thesis a Shirley background function was used, this is a useful function as it minimises the asymmetry in the components during fitting [96].
The Shirley function calculates the background intensity S(E) by,

$$S(E) = I_2 + \kappa \frac{A2(E)}{(A1(E) + A2(E))} \tag{2.9}$$

where κ defines the step in the background and is typically equal to $(I_1 - I2)$. This algorithm is an iterative determination of a background using the areas marked A1 and A2, thus the integrated areas for each point on the background must be computed at each step.

An initial survey scan is done over the whole range of binding energy at a lower resolution

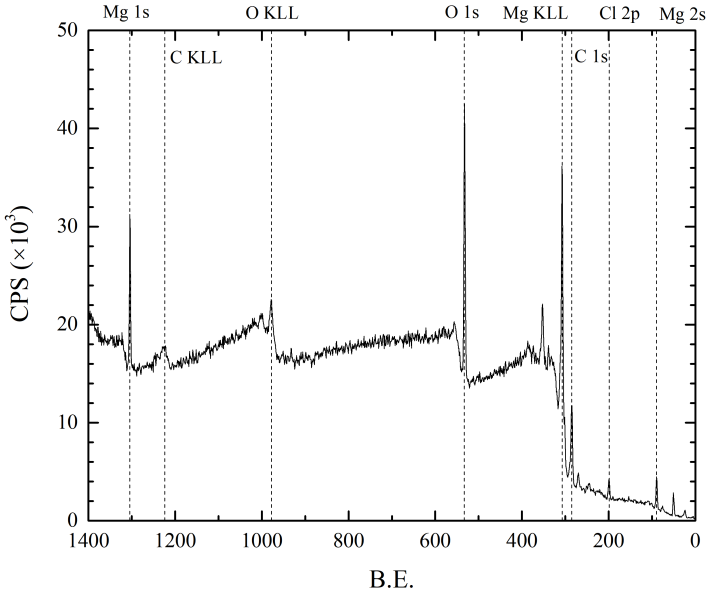

Figure 2.5: Example survey scan for MgO film on copper

to quickly highlight peaks of interest. The peaks can then be assigned to specific elements by

looking up tables of binding energy and manually assigning the peaks or letting the software automatically assign peaks, however this may highlight peaks that are not of interest or miss some that have been shifted out of the expected range (either chemically or by surface charging). An example survey scan for MgO film on copper is shown in figure 2.5.

Once these peaks have been located, narrow scans of higher resolution are performed on these select peaks, which can be used to find the different components present in a transition. Each element has a range of electronic states that can be excited, leading to possibly more than one transition peak visible in the spectrum for one element. The general rule for selection of a transition peak for quantification is to use the one with the largest peak area, subject to it being free from interfering peaks.

To get a basic quantification of the surface composition the peak area of the transition of interest is divided by the sum of the peak areas of all transitions, giving the atomic concentration (%). Intensities from the transitions need to also be scaled by Relative Sensitivity Factors (RSF). These factors are used to account for the relative sensitivity of the apparatus to specific elements and transitions peaks. The initial survey scan can be used for a rough quantification of atomic concentrations of elements in the top layer of the sample, however for detailed information on the chemical state of the various elements and what compounds are present, we need to use the narrow scans. This approximation however, assumes a homogeneous distribution throughout the sample therefore the structural model of the analyte needs to be known to ensure an accurate determination of concentration.

For each characteristic peak we assign a region, in this region we fit one or several components. The peak binding energy of these peaks tell us the chemical states of the atoms of that element. The FWHM can also give indications of physical influences such as a change in the number of chemical bonds contributing to that specific chemical state and/or differential charging of the surface. In theory the FWHM of a particular component is a convolution of the natural line width of the core level, photon source and analyser resolution.

The natural line width depends on the lifetime of the core hole created during the photoemission process. This can be calculated from the Heisenberg uncertainty relationship, $\Gamma = h\tau$. Where Γ is the intrinsic peak width in eV, h is the Planck constant and τ is the core hole lifetime in seconds. Γ increases with both atomic number of an element and for a given element with increasingly deeper shell orbitals, as the lifetime of the core hole decreases.

The fitting of component peaks to a particular region can be complex due to the overlapping of different peaks. Care needs to be taken when fitting peaks because even if the peak model fits the data well it may have no bearing on the physical properties of the sample.

Many factors can effect the lineshape and cause a deviation from the expected profile, including: the response function of the electron analyser, profile of the x-ray source, intrinsic life-time broadening of the core-level hole state, phonon broadening and differential charging of the sample.

In general, quantification in XPS is done using the functional form of the Voigt profile which is

a convolution of both Gaussian and Lorentzian distribution as shown in equation 2.10 below.

$$GL(x;F,E,m) = exp(-4ln2(1-m)\frac{(x-E)^2}{F^2})/(1+4m\frac{(x-E)^2}{F^2}) \tag{2.10}$$

This line shape is the general form used for all peaks fitted in this thesis unless stated otherwise. A general nomenclature used is GL(x) where the number in the bracket shows the mixing where GL(100) is a pure Lorentzian line-shape and GL(0) is a pure Gaussian line-shape.

As mentioned previously if the sample to be measured has insulating properties, such as MgO & ZnO which are both wide band gap insulators, charging up of the surface can cause the binding energies in the spectra to be shifted. To account for this a charge correction can be done by taking a peak with well known B.E. and shifting the whole spectrum by the difference in the actual measured B.E. and the expected B.E. The adventitious Carbon 1s peak is most commonly used for this purpose.

As well as using binding energies to highlight the chemical states of various elements the modified Auger parameter (α') can also be used. Originally defined by Wagner [97], this parameter is equal to the binding energy of the component of interest plus the kinetic energy from its respective Auger peak. As the kinetic energy of the Auger electron is independent of the photon energy, this parameter is unaffected by surface charging so therefore can be used as an effective marker for chemical states, especially when used in tandem with the binding energy measured.

Another feature present in the spectrum is peak splitting due to energy differences between the singlet and triplet states via interaction of the spin and orbital magnetic moments. This feature occurs when there are unpaired electrons in valence shells. If the unpaired electron is parallel to the valence electron it results in a lower binding energy, or alternately a higher energy for anti-parallel spin. The relative intensity of the 2 peaks of spin-orbit couplet is determined by the 2J+1 multiplicity of the levels. For example for a 2p spectra, the area ratio for the two spin orbit peaks ($2p_{1/2}$:$2p_{3/2}$) will be 1:2 which corresponds with the fact there are 2 electrons in the $2p_{1/2}$ level and 4 electrons in the $2p_{3/2}$ level.

2.4 ThGEM Housing

ThGEMs and other gaseous detectors need to be sealed in a noble gas or noble gas mixture. For most of our experiments a source of pure argon $(99+\%)$ gas is used. As such, a chamber needs to be made to hold and seal the GEM element whilst allowing UV light to enter without much attenuation. A UV transparent window is needed to allow UV photons through without much attenuation and the GEM element needs to have 2 connections: one to ground and one to a high voltage (HV) input.

One such chamber, which we will call the standard chamber, consists of two separate sections; a metal box to house the electronics and a front section which can be easily removed with a viton seal to keep the gas mixture in the chamber constant. On the back of the electrical box exists

an electrical connection which feeds into a data acquisition (DAQ) unit and gas entry to fill the front chamber with gas and subsequently seal it off using a tap. This setup is shown in figure 2.6.

Fused Silica was chosen as the material for the optical window into the chamber as it has high

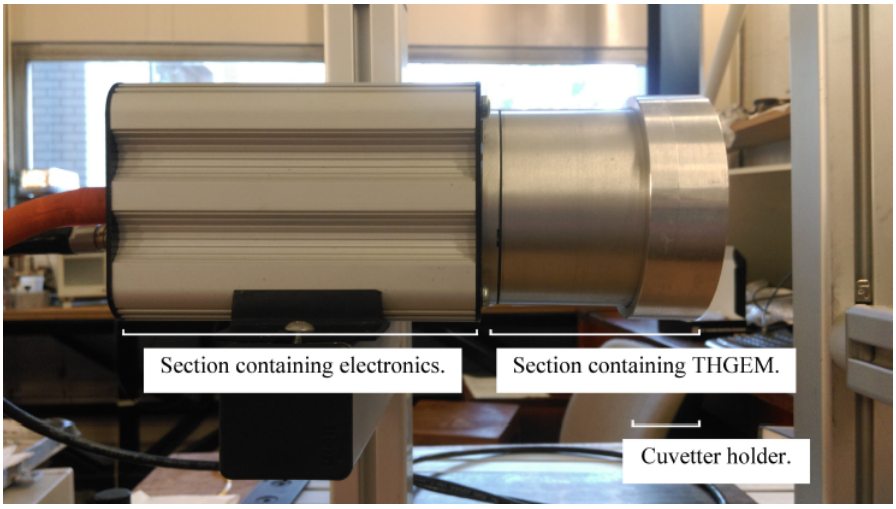

Figure 2.6: Standard chamber for mounting and testing ThGEM elements

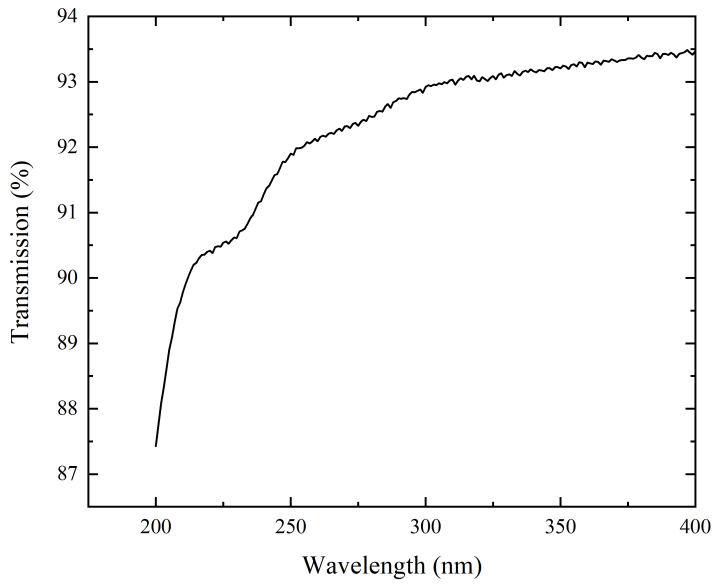

Figure 2.7: Transmission through fused silica window as function of incident wavelength

transmission ($> 90\%$) for wavelengths above 220nm. The standard transmission spectrum of fused silica is shown in figure 2.7, as provided by Thorlabs.

A table which has a spring loaded pin at the base connected to the HV supply and a connection

at the top which feeds the induced current output into the amplifier is used to mount the ThGEM element into the chamber. The table needs to be highly insulating and high density PTFE is used. Different tables are available for different thickness ThGEMs, with length and width of 15mmx15mm. The HV input and current output lead into a DAQ which is controlled by a computer.

To investigate larger ThGEMs another chamber was also constructed. Effectively operated in the same way as the previous chamber, this chamber also consists of a quartz window allowing UV light to enter without much attenuation. The HV in this case is controlled by a separate programmable NIM panel HV source. The amplifier used is the same circuit as that used in the standard chamber. The ThGEMs can either be free standing directly soldered onto wires or in a table similar to the one on the standard setup just on a larger scale.

2.4.1 Amplifier Circuit

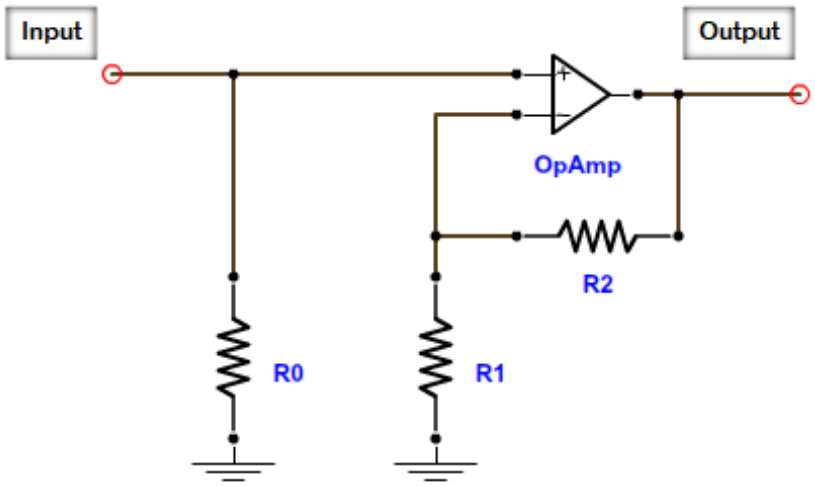

Figure 2.8: Basic Circuit diagram for amplifier circuit

As the output current is low, an amplifier is required to convert the small current from photo-generated electrons in the ThGEM to a readable voltage, it also needs to be resistant to sparks as the likelihood of one occurring can be quite high. The basic design is a current to voltage non-inverting amplifier as shown in figure 2.8, this basic circuit design is used in all of the different chambers. As the input impedance for the Op-amp is very high most if not all the input current flows into the resistor R0, giving a voltage across the non-inverting input of the op-amp of $V_+ = I_{in}R_0$. Therefore we use a large resistance for R0 (1GΩ). And the ratio of the resistors R1 and R2 control the output voltage such that $V_{out} = V_+(R_1 + R_2)/R1$. For this setup the gain in the amp is calibrated to convert 1pA of current into a output signal of 10mV, therefore $(R_1 + R_2)/R_1 = 10$.

2.4.2 Noise

There are lots of different types of noise present in the detector. There is electrical noise from the circuitry components in the operational amplifier and HV power supply such as: Shot, Thermal, Flicker, Burst and Avalanche. There is also electromagnetic pick-up from the residual noise in the room such as 'mains hum', which is the main source of noise in the detector, however this can be easily filtered out with a low pass filter, or shielding the detector with a grounded mesh. There can also be considerable noise due to micro-phonics, especially when the ThGEM is free-standing and not placed in the table.
When the ThGEM is being operated under illumination there will also be noise from the statistical fluctuations in the processes that occur such as photoelectron production and collection. All of these will contribute to the noise as they are inherently random events.
It is important to quantify the noise in our detectors as it limits the minimum detectable signal available. An important parameter used in many photodetectors is the signal-to-noise ratio (SNR) which gives an idea of the strength of the signal in question compared to the background noise.
Another point to consider is the extra noise generated by the UV light source, in particular the pond cleaning lamp (discussed in more detail in the section below) shows a large increase in EM pick-up noise if it is placed in close proximity to the detector.

2.5 Light sources and Calibration

Various different UV light sources were used throughout this thesis to investigate the response under different wavelengths. In this section the calibration of the spectral irradiance, for the different light sources used in this thesis, is performed. The spectral irradiance of our light sources is an important parameter for our measurements as it lets us compare the results from different light sources at varying distances and allows quantification of effective quantum efficiency.

2.5.1 Deuterium Lamp

The first light source we will look at is a deuterium arc lamp from LOT-QuantumDesign GmbH, which has already been fully calibrated. This lamp has a silica window to allow transmission of UVC light from deuterium discharge. This light source has high intensity, hard UV light emission and therefore the largest response under illumination, as such it is the primary light source used for when we are interested in comparative measurements as it will give the largest signal out of the light sources.

The Deuterium lamp produces a continuous spectrum from 160-400nm, a calibration of spectral irradiance at 300mm was performed at the Heraeus labs. However, the spectral irradiance measurements only go down to 200nm so we are unclear how much the lamp trails into harder UV. To estimate the power below this wavelength we fitted a simple Lorentzian function to the data,

$$y = y_0 + \frac{2A}{\pi}\frac{w}{4(x-x_c)^2+w^2} \tag{2.11}$$

although this is unlikely to be exact as there is likely some asymmetry in the power at lower wavelengths it will give us a rough estimate for our results, especially as we are mainly interested in comparative measurements.

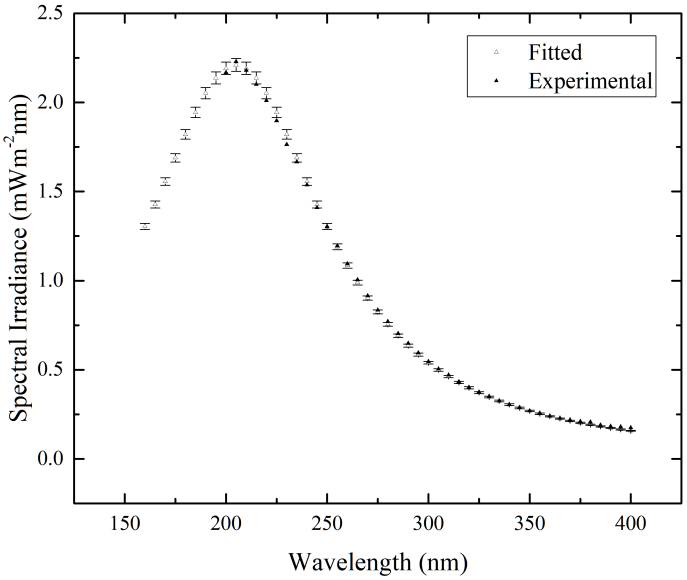

Figure 2.9: Calibration data for the deuterium lamp from Heraeus Fitted using a simple Lorentzian function

2.5.2 1st LED Housing

Another light source used was a housing which contains 2 white light LEDs, 2 blue light LEDs, and 2 individual UV LEDs at different wavelengths. These LEDs were procured through Thorlabs and table 2.3 shows their specifications as given by the manufacturer. In this section, we will attempt to get a full calibration of each of these LEDs although the white LED is only used as a reference light source to show that no signal is achieved for the visible spectrum for our detectors.

Full spectra of the LEDs was obtained using a miniature spectrometer from StellarNet Inc. which

produces a spectrum in terms of counts. The spectrum of normalised counts minus the background measured for the UV LEDs (206W, 300W & 370W) is shown in figure 2.10*a* and figure 2.10*b* for the White LEDs (LEDWE-15). For the 260W LED, the peak wavelength is around 262nm, 299nm and 372nm for the 260W, 300W and 370W LEDs respectively. The white LED is a convolution of 2 different peaks as mentioned in the specifications, the two peak wavelengths are 454nm & 554.5nm. These values match very well with those from table 2.3.

Name	Total Optical power (mW)	Peak Wavelength (nm)	FWHM
LED260W	0.3	260	12
LED300W	0.5	300	12
LED370E	2.5	375	10
LEDWE-15 (peak1)	13	450	20
LEDWE-15 (peak2)	13	560	50

Table 2.3: LED specifications of LEDs in the 1st housing shown in figure, the last LED, LEDWE-15 is a white light LED whose spectrum consists of two distinct peaks, therefore the optical power quoted relates to the power from both peaks

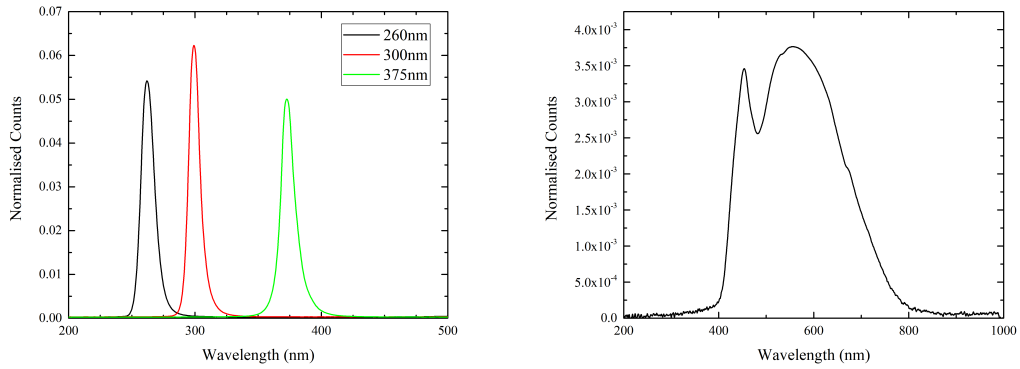

(a) (b)

Figure 2.10: Measured normalised spectrum of a) UV LEDs (260W, 300W & 370W) and b) White LEDs (LEDWE-15)

The next step in the calibration of these light sources is to convert the counts from the spectrometer into irradiance at a particular point. One way to do this is to use the manufacturer's total optical power measurement and multiply through by the normalised counts to get a radiance. We can then use the manufacturer's specification of a half viewing angle of 60° to get a irradiance at a specific distance, by a simple geometrical calculation, Irradiance=Power/Area where Area=$\pi(xtan(\theta))^2$ where x is the distance of a point from the light source and θ is the half-viewing angle.

However, to attempt to get a more accurate value of irradiance we also measure the power ourselves using a simple powermeter from Thorlabs. The responsitivity calibration of the pho-

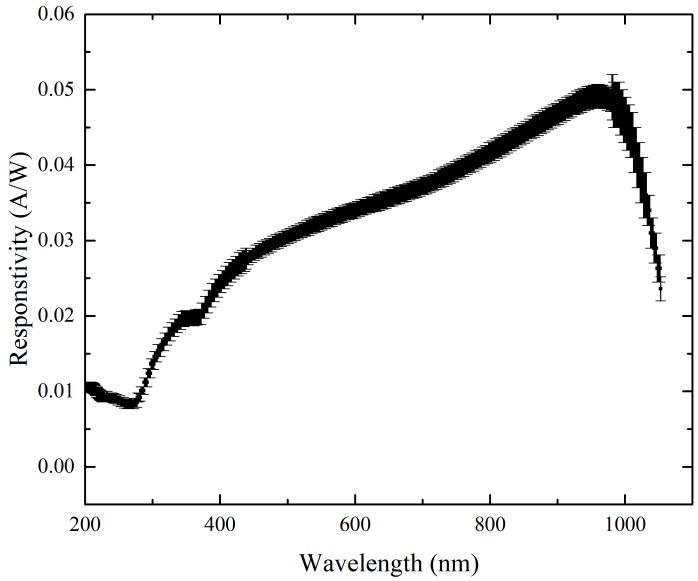

Figure 2.11: Responsivity curve of photodiode powermeter SV120C from Thorlabs.

todiode sensor was given by the manufacturer and is shown in figure 2.11.

The power measurements using this photodiode at a distance of 20mm are shown in figure 2.12,

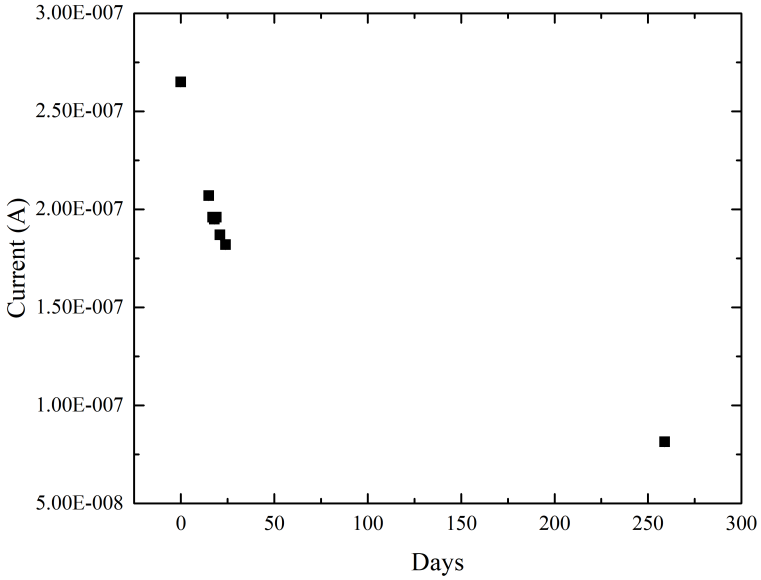

Figure 2.12: Power measurements of 260W LED using the Thorlabs sensor over a period of days at a distance of 20mm

over a period of many days. It can be seen that the power measured is decreasing, this could be due to a change in power over the lifetime of the LED, change in the responsivity of the power meter or a combination of the both. Therefore it is hard to say exactly what power is received from the LED. However we will take the value of 8E-8A that the LED appears to settle to as the lower limit of light from the LED. This gives us a total irradiance of 0.1344W/m^2 at a distance of 20mm, which using the simple geometrical approximation used before would give us a total power of 0.5mW which is actually higher power than the manufacturers specifications. The reason for this is probably the assumption that the power density is uniform across the illuminated area is wrong, with more power being focused centrally in the direct line of sight from the LED. For future use of the irradiance from this LED we will use a simple inverse square law on the value at 20mm to estimate the photon flux at any particular distance.

2.5.3 Pond cleaning Lamp

Another UV light source that is used is a pond cleaning lamp. This light source had no documents eluding to its emittance in wavelengths or optical power. As in the case of the LED housing we also used the StellarNet spectrometer to get a spectrum of the pond lamp, it can be summarised that this lamp is a low pressure Mercury vapour lamp due to its characteristic dominant emission line at 253.7nm.
As there is no power given by the manufacturer, we have to rely on the power measurements using the Thorlabs power meter. Which on average at 50mm distance gave a power reading of 1.455E-4W, which gives the irradiance shown in figure 2.13

2.5.4 High Power LED

The final light source used is a high power ball lens LED from Thorlab called 250J. According to the manufacturers specification this LED has a central wavelength at 250nm, FWHM of 12m, and a minimum optical power of 1mW. Also due to the ball lens the LED has a much smaller half viewing angle of 7.5°, with most of its intensity being focused into even smaller angles than this. Figure 2.14 shows the typical far field intensity distribution for this LED as given by Thorlabs.

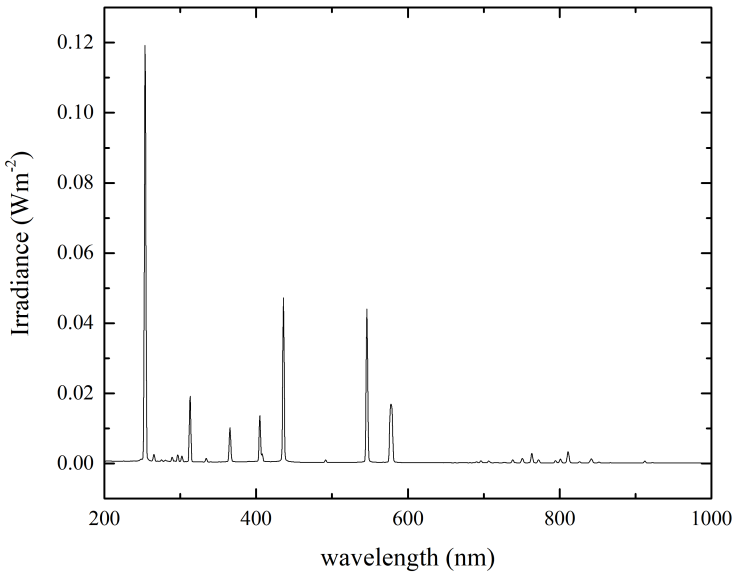

Figure 2.13: Calculated irradiance spectrum using the spectra measurement using StellarNet spectrometer and Thorlabs power meter at a distance of 50mm

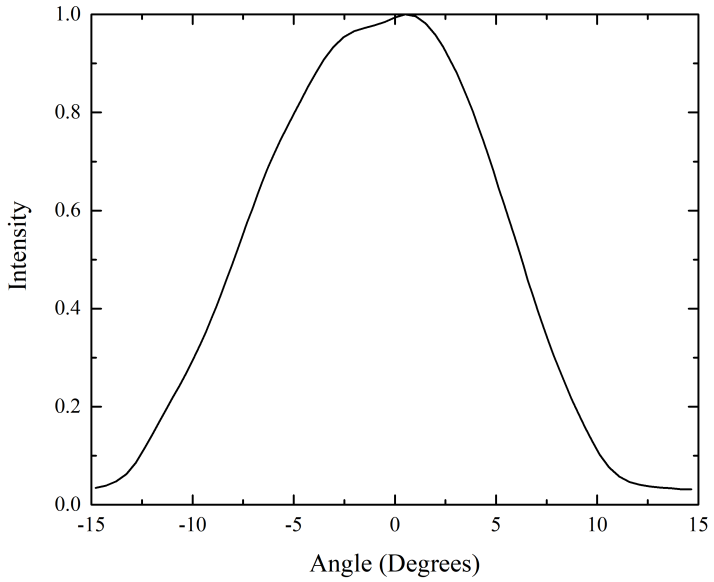

Figure 2.14: Typical far field intensity distributon for 250J LED from Thorlabs

Chapter 3

Study of Gaseous Electron Multiplier Operating Conditions

3.1 Introduction

The signal from the GEM element can be expressed as

$$I_P = e \times \varepsilon \times M \times \phi_i, \tag{3.1}$$

where ε is the quantum efficiency of the detector, M is the multiplication factor (or gain) of the GEM element, ϕ_i is the incoming photon flux impinging upon the photocathode and e is the charge of a single electron.

The quantum efficiency (ε) of a detector can be further broken down into two separate elements: the quantum yield (QY), the number electrons emitted per incident photon and the electron transfer efficiency (ETE) i.e. the probability of an emitted electron being transferred to the multiplication region. ETE is assumed to be dependent only on the reduced electric field (E/P).

In this chapter the operating conditions of the basic ThGEM design and a novel design called the Gaseous Gap Electron Multiplier (GGEM) are investigated. The output photocurrent will be measured for different GEM elements exposed to UV light, which will give us effective gain comparisons, as the quantum efficiency is assumed to stay roughly the same under stable conditions and a constant high voltage bias. Although variations in quantum yield (QY) will occur between samples, the assumption that the QY is similar for materials under same conditions should allow reasonable comparison between the structural properties without the direct measurement of QY. To further improve our results it would be useful to first get direct measurement of either gain of the detector or QY of the photocathode for each element to be tested. Direct measurment of QY of the photocathodes is discussed further in chapter 5 and the direct measurement of gain in the ThGEM devices is out of the scope of this thesis.

The relative gains of various ThGEM devices will be measured with different structural properties and under different gaseous conditions to get experimental data on the effect of such

properties on both the total signal and stability over time, comparing these results to those found in the literature.

3.2 ThGEM Fabrication method

The ThGEMs used in this thesis are made in house, out of printed circuit board via a simple UV lithographic method, where the board is exposed to UV light and subsequently etched using a bath of heated ferric chloride. Any pattern required can be made by a mask printed on transparent paper which will protect the copper that is required from the etchant.
An example mask used is shown in figure 3.1, this allows us to make a batch of ThGEMs from one PCB board, a similar mask is then used on the bottom side. On these masks there is a single connector, which will be on top and bottom on either side (One for the HV input and one for the photocurrent output). Holes are pre-etched into the copper to help reduce burrs when mechanically drilling. If hole diameters are drilled which are larger than these etched holes, burrs can cause the ThGEMs to spark at voltages as low as 1kV, possibly even before any reasonable signal is measured. Also, due to sparking at the edges a gap between the edge of the GEM and the edge of the copper electrode was also introduced into the etched pattern.

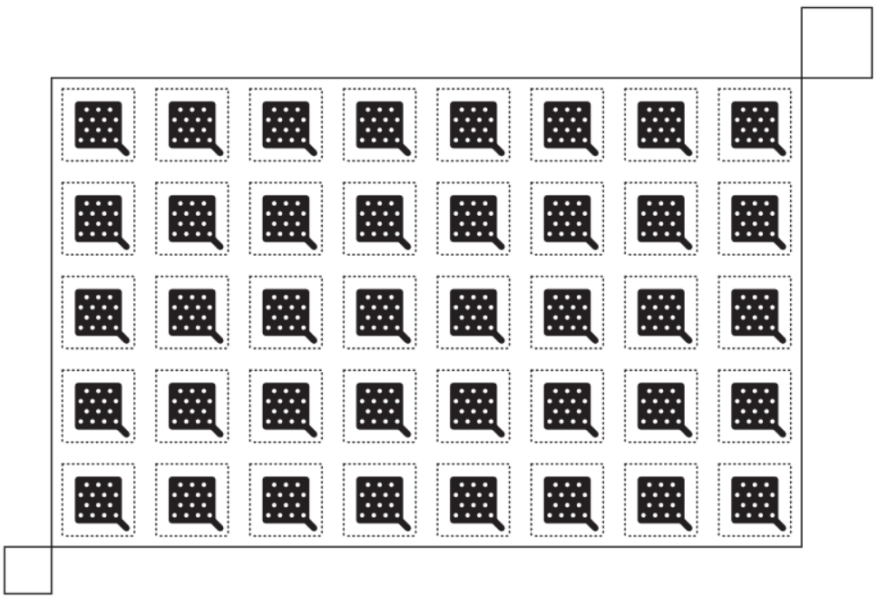

Figure 3.1: UV photolithographic mask for the etching process in the manufacturing of ThGEMS

Individual ThGEMs are then cut out using a dremel saw and holes are mechanically drilled into the FR-4. As the holes are drilled by hand it is expected this will cause some non-uniform operation, but can be taken as a worst case for operational stability. To improve the stability of the

ThGEMs laser or CNC drilling can be used to improve hole quality and make sure the etched rim is centred around the hole.
The standard cleaning process is to submerge the ThGEMs in a 50:50 mix of acetone and isopropanol and use an ultrasonic bath for 3 to 5 minutes. The remaining solution is then dried off with a nitrogen gun. However other methods of cleaning the surface were also implemented, for example we also polished the surface of some of the ThGEMs with solution of Brasso. ThGEMs which had been polished showed a large increase in the photocurrent measured for a given high voltage bias. The effect of different cleaning methods on the work function and photocurrent measured is discussed in more detail in chapter 4 and 5.

3.3 Leakage Current and Noise

The leakage current is the current that flows from one electrode to another through the dielectric when the HV bias is applied. If this current is large then it can affect the accuracy of the detector. As such in this section this current is measured to investigate if it is a potential problem for ThGEMs fabricated from PCB.
Figure 3.2, shows the leakage current measured as a function of the HV bias across a standard

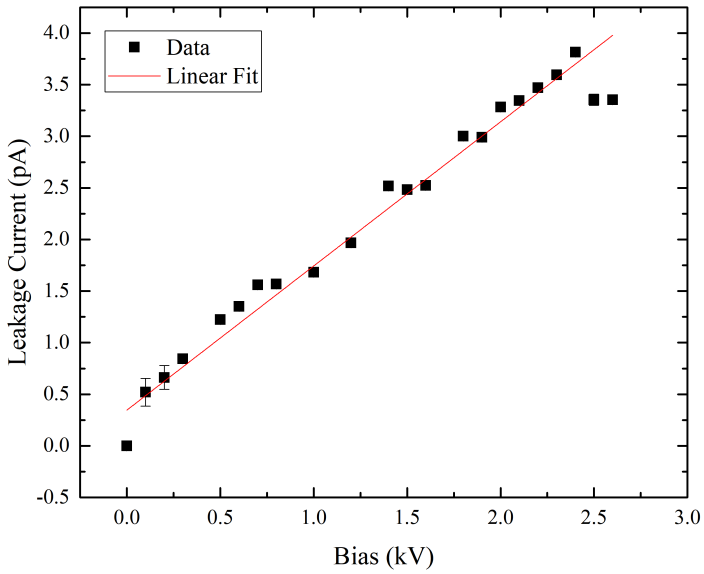

Figure 3.2: Leakage Current of ThGEM as a function of Bias

PCB ThGEM. It can be seen that although the leakage does increase with an increase of HV bias. The actual amount of current is very small and is smaller than other experimental errors and therefore for the most part can be ignored. The signal measured under illumination will be

subtracted from the signal when the light is turned off therefore negating the adjustment needed from any leakage current.

The amount of electrical noise present in the detectors is also important as this will have an effect on the sensitivity, as a signal to noise ratio of greater than 1 is needed to measure a signal. The electrical noise before and after a lowpass filter are shown in figures 3.3*a* and 3.3*b* respectively. The average noise under no illumination is about 44.8mV$\pm$1.4mV, however most of this noise is at 50Hz from mains hum and can be filtered out. After a lowpass filter of cutoff 40Hz, the noise is reduced to 4 ± 2mV or 0.4 ± 0.2pA. Extra noise can be present when a light source is placed in front of and close proximity to the detector due to electromagnetic pickup. However, fluctuations in gain or incident photon flux are expected to be the primary sources of uncertainty.

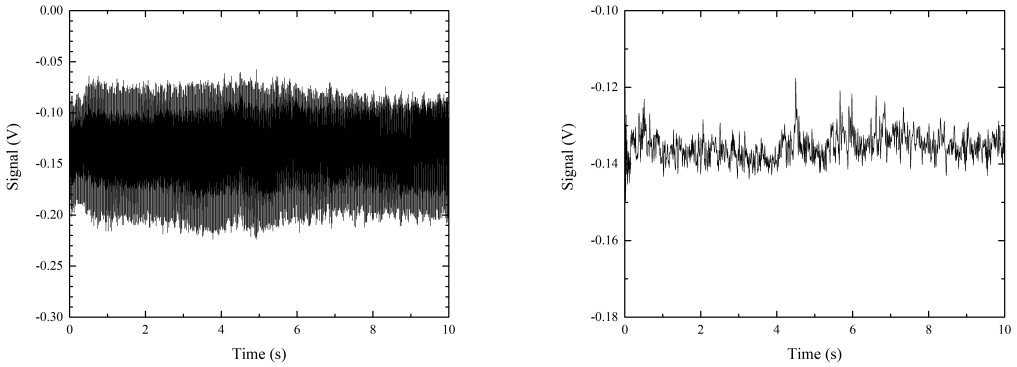

(a) (b)

Figure 3.3: Electrical noise from ThGEM under HV bias but with no illumination before (a) and after (b) 40Hz low pass filter

3.4 Gain Stability

An important part of the detectors performance is how stable the gain is over long operation periods. If the gain fluctuates over time, it will be difficult to quantify the light incident on the detector without constant calibration, the device may also drop to a sensitivity too low to detect what it is intended to, or it may increase to a gain that will cause a spark breakdown. This will obviously effect the detector's usefulness in applications where it is expected to be run over long periods.

In this section we will quantify the timescales and intensity of the short and long term gain fluctuations and attempt to find what the main causes of gain variations are in a sealed detector environment. Many factors may effect the response of the detector and cause variations over time, such as: small amounts of gas contamination, often from outgassing of components under HV bias; a change in ambient conditions such as temperature or humidity of the room, which

can change the pressure or humidity inside the chamber; charging up of insulating material or build-up of space charge in the gas, resulting in a change in the overall electric field strength. The variety of parameters effecting the gain stability and their difficulty to measure/control means that studies on the effect of these parameters on long term gain stability are not easily reproducible.
It is assumed that in a sealed detector environment that the charging up of surfaces exposed to drifting charge carriers and the polarization of the dielectric volume are the primary factors causing gain variation. Further information on the charging up effects in GEMs and studies in literature has been previously mentioned in section 1.4.5.

3.4.1 Photocurrent Measurements

In figures 3.4*a* & 3.4*b* the long term response is shown for a single ThGEM under different HV biases.

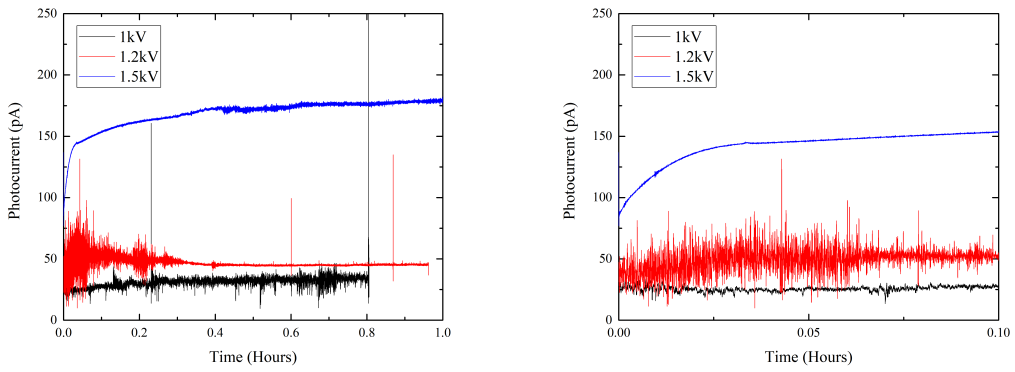

(a) (b)

Figure 3.4: Long term signal from standard ThGEM under illumination from deuterium lamp for over a period of a) 1 hour and b) 0.1 hours

This ThGEM is made from the standard pattern of 1.2mm etched holes with 2.5mm pitch and has 1.2mm diameter holes with no etched rim. The signal from the ThGEM has a short and long term rising behaviour for all three different voltage biases. This goes against the standard belief that gain should drop due to lateral diffusion of charge carriers due to the electric field, however as mentioned in section 1.4.5, rising behaviour has been attributed to charging up in dielectric rims around the holes. Whilst in this design there should be no rims due to drilled hole diameter being the same as the etched hole diameter, there will be some inaccuracies in manually drilling holes and therefore small dielectric rims around the holes could still be present.
The 1.2kV trace also appears to rise and then drop to settle off over the period of an hour. This shape matches that for a negative induction field (all ions collected on bottom electrode) from

Pitt et al. [64]. Which would agree with our case as we do not have a seperate electrode for measurement and therefore most of the ions will be collected on the bottom electrode, causing extensive charging up of the bottom electrode as well.
For the high voltage bias (1.5kV) the long term response also shows rising behaviour even over a period of 4000s. This could be due to an increase in the characteristic timescale of the charging of the top rim, which is also suggested to increase with gain and inverse of ETE, as shown in equation 3.2, taken from Pitt et al. [64] which shows the ratio of the characteristic time for increase in gain and decrease in gain,

$$\frac{\tau_{up}}{\tau_{down}} \propto \frac{G \times ETE}{(1-ETE)} \tag{3.2}$$

where τ is the characteristic timescale for rise and drop in gain, G is the gain and ETE is the electron transfer efficiency.
Therefore at higher biases it appears that the rising behaviour (attributed to charging of the dielectric rim on the top surface) dominates, causing the signal to rise, this is also a long process as the characteristic timescale increases with the gain of the device.
Renous et al. [98] also noticed that the performance of pre-used electrodes which had been

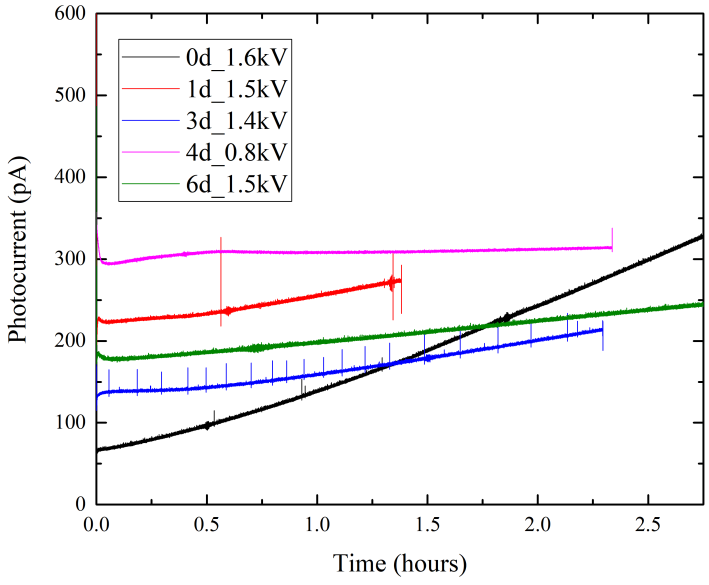

Figure 3.5: Photocurrent of Brasso polished ThGEM over a period of days under illumination of deuterium lamp. 1st number in the legend is number of days and second number is the bias. Between 1 day and 3 days the ThGEM was removed from the chamber.

exposed to radiation induced avalanche multiplication were found to perform differently. This has also been found to be true for our ThGEMs as well.
An example of this behaviour is shown in figure 3.5 which shows the response of a single

ThGEM over a period of a few days. The first measurement was taken at a bias of 1.6kV, as this was the HV required before an initial signal was visible. The bias was chosen for later days to have a similar photocurrent, as the original 1.6kV bias caused the signal to saturate the amp.
From this figure we can see there is a large increase in signal between 1 and 2 days and 3 and 4 days, the signal also dropped when the ThGEM was removed from the chamber and placed under nitrogen flow (between 4 days and 6 days). This could be because removing the device effectively removed the charge from the electrode, much like the initialization step in Renous et al. [98] which used an anti-static gun flushing the ThGEM with 1 minute jet of ionised nitrogen.
Both the long term rising over periods of hours and the effect of the charge history of the electrodes leave some difficulties in comparative measurements of signals as the characteristic time in which it takes for signal to settle off depends on each individual ThGEM, therefore enough time is needed to let the signal settle before comparing the response from different ThGEMs and their varying properties. However, this can be a very long time as shown in figure 3.5 where the initial rising shows no signs of settling off even after 2 and a half hours. Also as shown in figure 3.5, if a sample is left in the chamber it can have a drastically higher signal the next day.
In all our experiments following we have taken care to wait until the signal has settled to a point where it is not visibly rising or falling over time periods of interest. To further ensure that the rising in the gain does not effect measurements, recalibration of the signal can be performed after any experiment to check that the signal has not risen noticeably over the time period that the detector was being used for. Also when taking measurements, new samples are used to limit any affect from charge recollection.
Although this large long term rising effect is seen as mostly a negative aspect of the detector operation (due to its limitation on accuracy immediately on start up) the effect can be used to increase the gain of the detector and measure low photon fluxes that may have been hard to detect before. As shown in figure 3.5 after a few days the signal is as high as 300pA at a bias of 0.8kV where it was completely undetectable at this voltage on immediate start up. Also the long term signal is noticeably more stable than the other days, most likely due to the fact that the ThGEM is now being operated at a lower voltage bias.

3.4.2 Gas Contamination

A possible contributor to the overall gain stability is the gas mixture or amount of contaminants in the gas. Contaminants in the chamber can be from residual material in the chamber (i.e. condensation) or from outgassing of the components during operation.
To investigate the effect that contaminants have on the overall gain and its stability, the larger chamber was cleaned thoroughly and then baked overnight to remove any contamination. The old rubber hose normally used to transfer the gas was switched for a stainless steel gas line and the chamber was kept either vented with argon (when removing the window) or sealed in argon. However no noticeable difference was noted, this suggests that the gain instability is mainly

related to the detector element itself. This could be the charging up of the dielectric mentioned earlier, build up of space charge effecting the local electric field in the ThGEM or the components of the detector outgassing during operation.
Argon gas was also left flushing through the chamber for 12hours before measurement compared to the standard few minutes. However this was found to have no noticeable effect on the photocurrent measured nor the rising effect over long time periods. As such it can be concluded that if small amounts of gas contamination do have an effect on the stability or gain of the detector it is much smaller than other effects.
To check the amount of outgassing of the components during operation a smaller chamber was

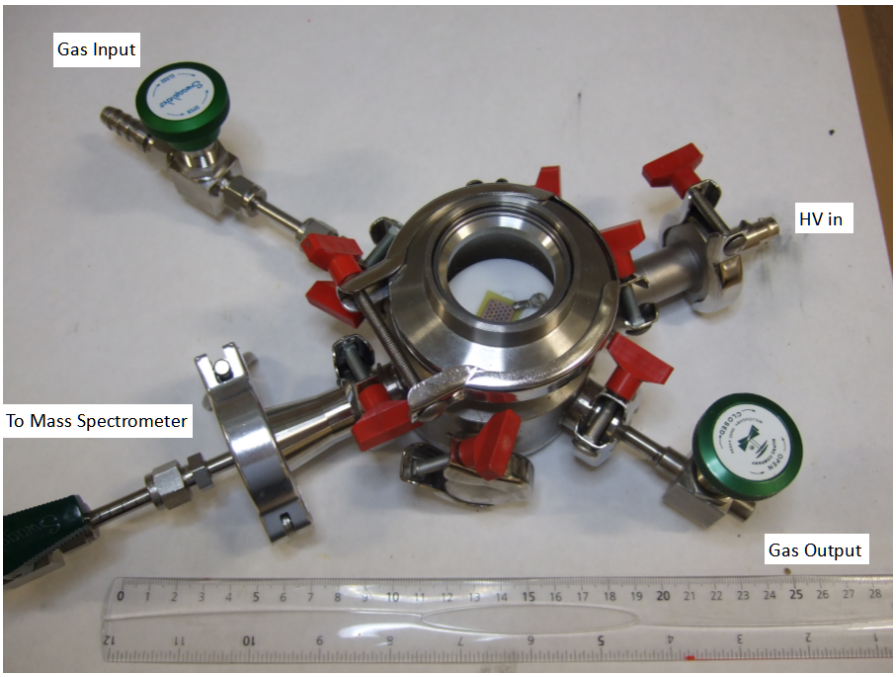

Figure 3.6: Smaller chamber used for mass spectrometry measurements

attached to a mass spectrometer, as shown in figure 3.6. This chamber was fitted with the normal PTFE table used in the other chambers and was attached to a mass spectrometer. This chamber was flushed with argon and then slowly pumped down overnight to viable operating pressure for the mass spectrometer. Then the ThGEM was placed under a 1kV bias and the gas was measured over a period of 14 hours.
The data taken is shown in figure 3.7*a* and 3.7*b* for over a period of 2 and 14 hours respectively. The main 2 contributors to the gas are at 40 amu and 28 amu, these will be mostly from Argon and Air respectively. Other branching fractions of 20 amu for Argon and 32 amu and 14 amu for Air can be seen. The only other noticeable contribution is at 18 and 17 amu which is most likely from water in the system.
First thing to note is that this experiment is not respective of our operation conditions as Argon is flowed into the detector even when it is sealed off so any drop in pressure is filled by Argon

and air should not leak in. Whereas in the case of this smaller test chamber, once it was sealed it was left so the increase in air and water content after about 3 hours is most likely not as pronounced in our detectors and also unlikely to account for the difference seen in gain over these time periods as mentioned in the previous section.

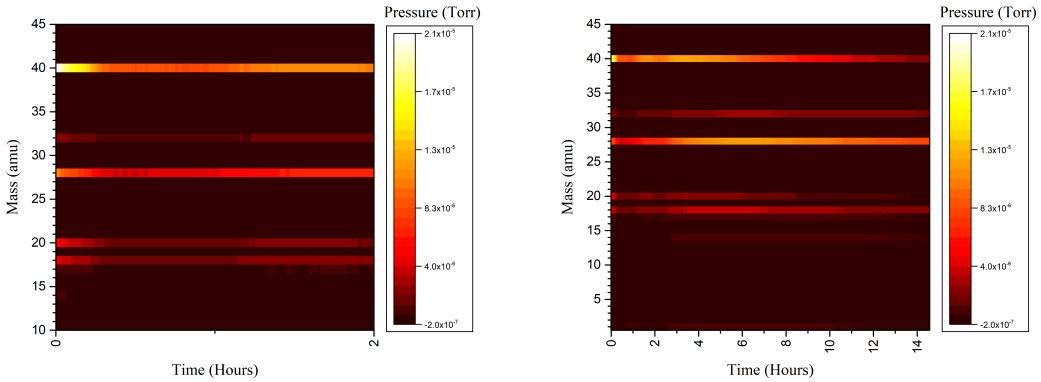

(a) (b)

Figure 3.7: Mass spectrometry measurement of residual gas in chamber over a)2 hours and b)14 hours

3.5 Gas Properties

3.5.1 Pressure

Pressure also has a large impact on the gain of the detector. It is well known that by increasing the pressure the maximum gain possible decreases with increasing pressures from atmospheric. Figure 3.8 shows how the signal changes at pressures lower than atmospheric pressure, for a 15mmx15mm Gaseous Gap Electron Multiplier or GGEM (which will be discussed later) under illumination from deuterium lamp. The chamber was pumped down with a rotary pump and slowly filled with pure Argon. The figure shows the bias needed to achieve a 300mV signal, as the pressure increases the bias needed to achieve the same gain increases.
Figure 3.9 shows how the signal changes for a standard ThGEM as the pressure is increased for pressures above atmospheric pressure. Most of the measurements for the rest of the thesis are done at sealed pressures of 1.4bar as this results in a large measurable signal, as can be seen from the figure.

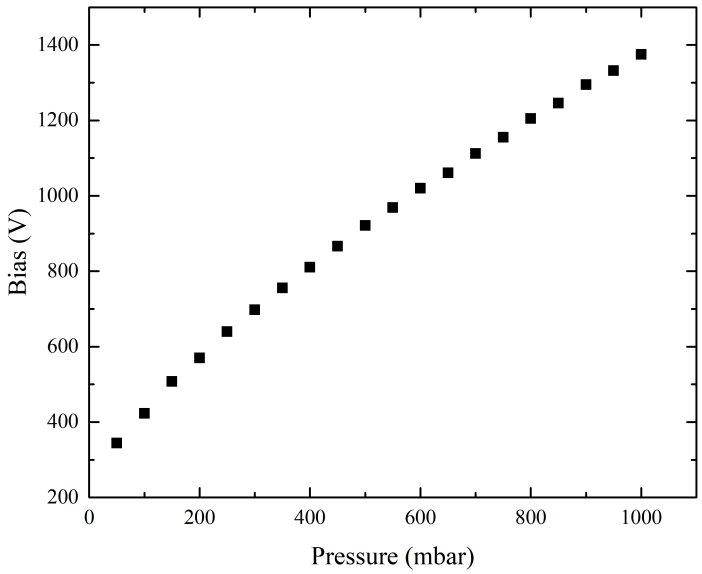

Figure 3.8: Bias needed for 300mV signal under deuterium lamp for increasing pressure

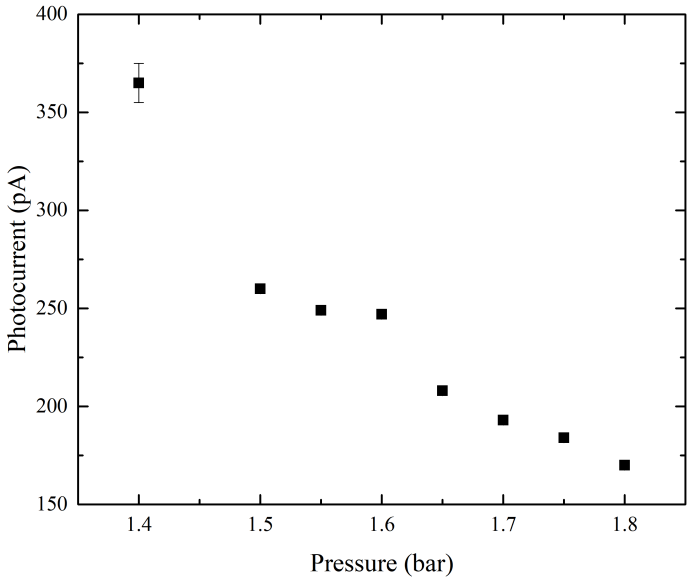

Figure 3.9: Photocurrent measured as function of pressure under illumination of deuterium lamp

3.5.2 Gas Mixture

Figure 3.10 shows the response of a single ThGEM under two different gas mixtures: pure argon ($> 99.9\%$) and an argon/CO_2 90:10 mix. These ThGEM were illuminated by the deuterium lamp

at the same voltage bias (0.8kV). As shown in the figure, in general the $ArCO_2$ shows a reduction in photocurrent measured. Also one might expect that with the addition of CO_2, which acts as a quencher, that any run-away charge build up in the gas might be reduced. However it is clear from the figure that the long term rising behaviour is not removed, and in this case appears to actually have increased. As such most measurements will be performed using the pure Argon gas, as this results in the highest signal.

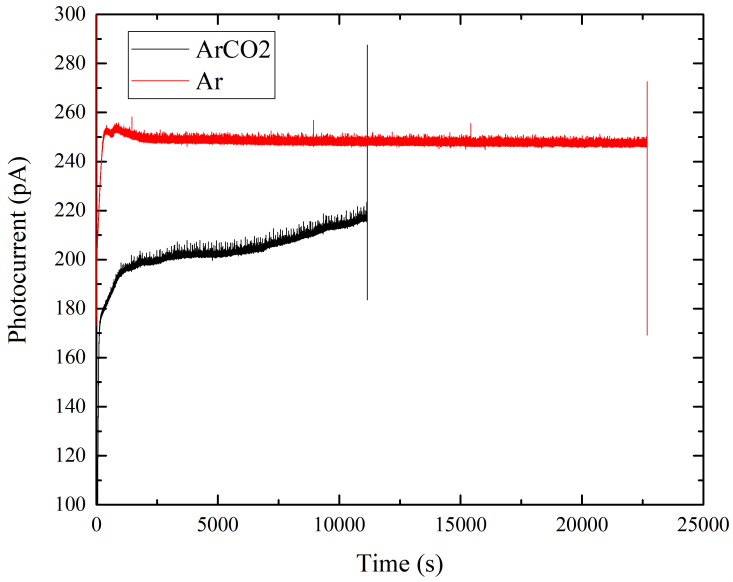

Figure 3.10: Comparision between two gas mixtures (Pure argon and Argon/CO_2 mix) at same HV bias under illumination of deuterium lamp

3.6 Geometrical Properties

Shalem et al. [99] presented a study of the signal from ThGEMs at atmospheric pressure with different geometrical parameters such as: thickness, hole diameter, etched rim and pitch. In this study it is stated that with decreasing hole diameter the electric field becomes more focused in the hole increasing the amount of multiplication in the hole. However, it is also stated that optimal geometrical parameters for maximum expected gain is $t/d \sim 1$ where t is the thickness and d is the diameter of the hole, due to a trade-off with the electron collection efficiency.
In this section of the thesis we will attempt to investigate the change in the effective gain of our ThGEMs by varying different geometrical parameters and comparing these changes to that found in the current literature.

Figures 3.11*a* and 3.11*b* show the measured photocurrent from ThGEMs with different hole

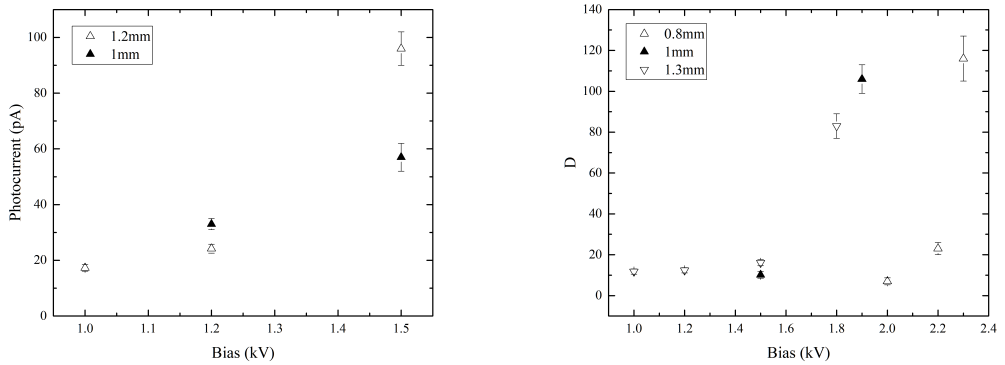

(a) (b)

Figure 3.11: Photocurrent measured under illumination of deuterium lamp for solvent cleaned samples with varying hole diameters, with different pitch masks used: a) 2.5mm and b) 3mm. The dimensions in the legend represent the diameter of drilled holes

diameters which have been mechanically drilled. Two different UV masks were used: the normal 1.2mm diameter with 2.5mm pitch as shown in figure 3.1 and a similar mask with 1.5mm diameter and 3mm pitch, this mask will have 9 holes in a 3x3 square array, instead of a hexagonal array of 14 holes. However as these designs have very similar active photocathode areas, we will not take into account any change in the incident flux on the surface.

Various hole diameters were mechanically drilled into these two different patterned ThGEMs, therefore the size of the etched rim around the hole depends on the size of the hole drilled and the pattern used i.e. a 1mm diameter hole drilled into the 2.5mm pitch pattern would result in a rim of thickness 0.1mm but in the 3mm pitch design it would result in a 0.25mm thick rim.

For all the measurements the mean output current is taken after the response appears to not be varying over a period of 1000 seconds. Also the ThGEMs measured in this figure were new so should not have any 'charge recollection' as mentioned in section 3.4.1. We are also focusing on the relative gain differences due to the electric field of the devices as we change the structure, as such, the QY of the photocathode surface has been ignored and assumed to be the same for the same cleaning method and age.

It appears that in general the ThGEMs with the 3mm pitch pattern (from figure 3.11*b*) have lower photocurrent values than the 2.5mm pitch pattern ThGEMs (from figure 3.11*a*) at the same HV bias. This is probably simply due to the fact that there are less holes in the 3mm pitch pattern, 9 instead of 14. If these are viewed as separate multiplication channels that have the same gain then the 3mm pitch pattern should on average have 9/14 times lower signal, however the signal difference between the two 1mm hole diameters is larger than that. A possible reason for this reduction could be due the much larger rim and larger spacing for the 3mm pitch design which could lower ETE and therefore the output signal.

It would suggest that the larger number of holes on the ThGEM surface the higher the resultant

gain, and therefore signal, would be. However, there will be a trade-off between number of holes and the active photocathode area. As these two patterns happen to have similar photocathode area the effect of a decrease number of holes is more prominent.

It can also be seen from the two figures, that the larger hole diameter have higher signal at lower

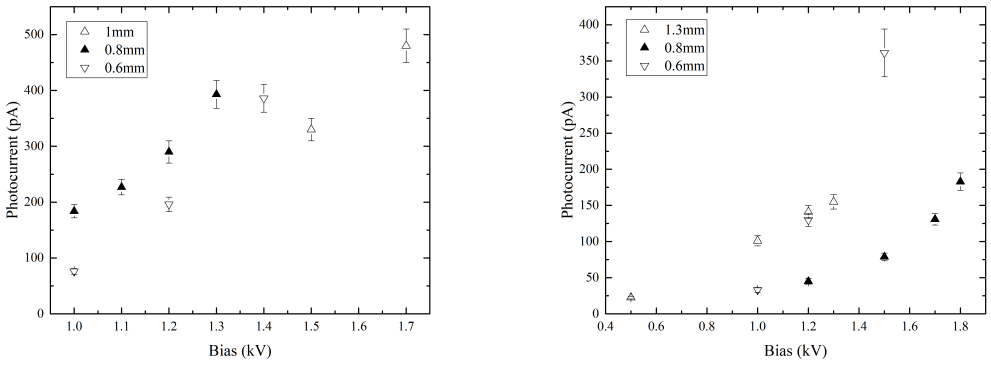

(a) (b)

Figure 3.12: Difference in photocurrent measured under illumination for different hole diameters for Brasso cleaned samples. For the two pitch patterns, a)2.5mm and b)3mm

HV biases (before rising effects take over). This suggests that the optimum t/d 1 is correct as the thickness of the ThGEMs is 1.6mm so the larger hole sizes appear to give a large signal, despite the fact that the electric field will be less focused in these holes.

Figures 3.12*b* and 3.12*a* show the photocurrent measured for samples mechanically polished

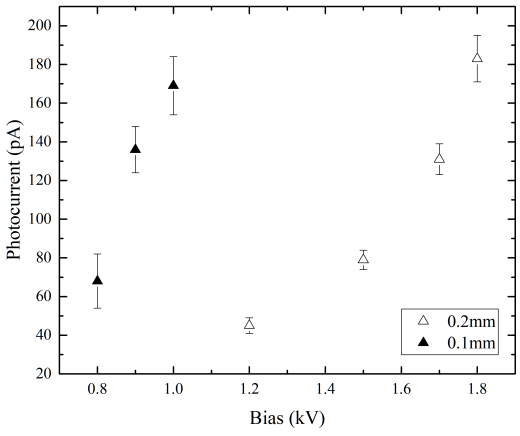

Figure 3.13: Difference in photocurrent measured for a ThGEM with 0.8mm diameter, 2.5mm pitch but with different etched rim thickness

using Brasso, which was found to increase the photocurrent measured. Just like the hole comparison for samples cleaned in solvent solution in general the 3mm pitch pattern has lower signal.

However in opposition to the solvent cleaned samples the smaller hole diameter of 0.8mm has a higher signal than the larger hole diameter of 1mm for the 2.5mm pitch pattern, this is most likely due to the rising signal present which adds significant error to the photocurrent measured using this method.

To investigate the effect of rim size on the output signal, another mask was created which was

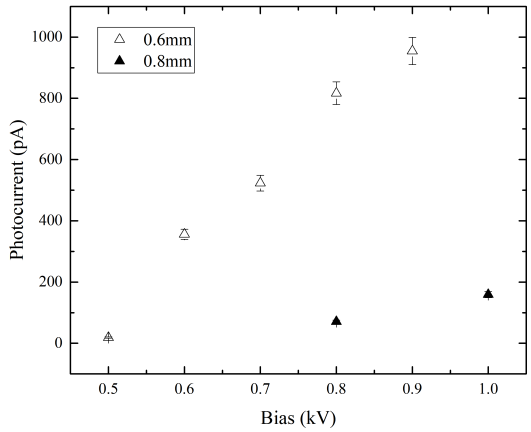

Figure 3.14: Photocurrent measured for 0.8mm thick ThGEM under illumination of deuterium lamp for different hole diameters

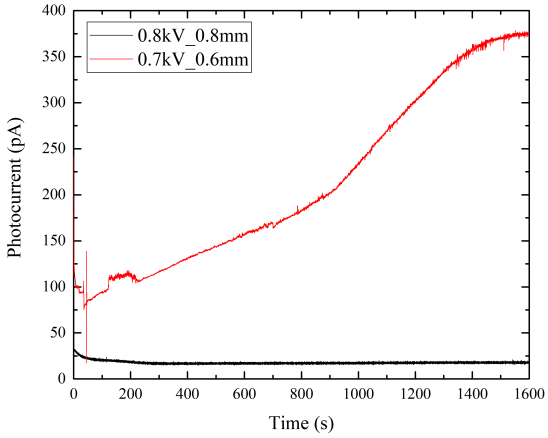

Figure 3.15: Response as function of time for 0.8mm thick ThGEMs with different hole sizes under illumination of deuterium lamp

identical to the 2.5mm pitch pattern except the hole diameter in the mask was 1mm instead of 1.2mm. Figure 3.13 shows the difference in signal between these two different ThGEM patterns. It can be seen that the pattern with the smaller etched rim has a larger signal, despite the presence of the rim causing a rising signal and therefore a larger signal measured as mentioned in section

3.4.1. This might be because the increase in rim size could reduce the collection efficiency. Figure 3.14 shows the photocurrent measured for ThGEMs with 0.8mm thickness, 1.6mm pitch and 2 different hole diameters 0.6mm and 0.8mm. It can be seen in this figure that the ThGEM with 0.6mm hole diameter has a much larger signal, this again appears to be at odds with the optimum t/d 1 stated by Shalem et al. [99]. However from Figure 3.15, which shows the response as a function of time for these 2 different ThGEMs, it can be seen that the ThGEM with 0.6mm hole diameter has a much larger rising behaviour which can be attributed to the charging up of the dielectric rim around the hole. This suggests that having an etched rim of 0.1mm thickness leads to the most amount of rising behaviour and therefore results in a larger signal after it settles, which could explain the deviation from the optimum approximation t/d 1 especially higher HV bias.

3.7 Gaseous Gap Electron Multiplier

In an attempt to investigate the effect of the FR-4 as a dielectric in the GEM device we constructed a new table out of Polyether Ether Ketone (PEEK) which was used to clamp two separate metallic foil squares with holes laser drilled into the surface, effectively creating a GEM device without the insulating dielectric structure in between the electrodes. Also by fabricating the holes using a laser drilling method we eliminate any worries about burrs, misalignment of the holes or etched rims and their subsequent effect on the gain. This device is coined in this thesis as a Gaseous Gap Electron Multiplier (GGEM).

3.7.1 Leakage Current

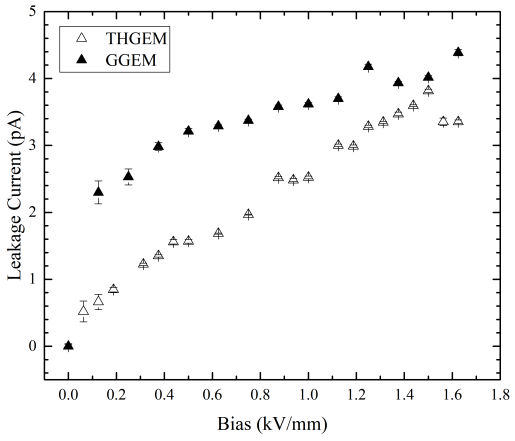

Figure 3.16: Comparative leakage current between 1.6mm ThGEM and 0.8mm GGEM

As in section 3.3 the leakage current of the new GGEM device is measured. In figure 3.16, the results of a GGEM with 0.8mm multiplication gap is compared to a standard 1.6mm ThGEM in figure 3.16. It can be seen that despite the removal of dielectric between the electrode plates the leakage current is still similar if not larger. This is most likely due to the fact that the GGEM plates are in contact with the PEEK material of the table.

3.7.2 Photocurrent Measurements

Gain Stability

As for the normal ThGEMs we will first investigate the long term gain stability. It is expected that due to the removal of dielectric around the holes in the device and therefore the removal of any possible exposed dielectric around the holes to charge up, that the rising in signal attributed to charging of the etched rims of ThGEMs should no longer be present.

Figure 3.17 shows the response of a GGEM with 0.8mm multiplication gap, 0.8mm diameter

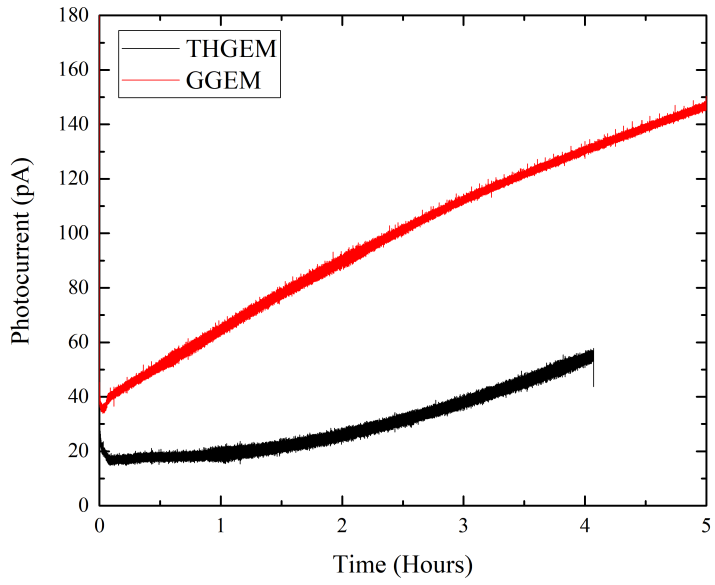

Figure 3.17: Response over long time period comparison between GGEM and ThGEM of same dimensions

holes with 1.6mm spacing at a a bias of 0.8kV under illumination from deuterium lamp compared to a normal PCB ThGEM of same thickness, hole layout and voltage bias.

There is still substantial rising in signal over a long time period, in figure 3.17. However the long term rise appears to be a different shape to the exponential rise from the ThGEM and appears to settle to stable values at a shorter timescale than the standard ThGEM. This suggests

that although the exponential rising in the signal (most likely due to charging up of the dielectric rims) is removed, there is still another long term rising mechanism involved.
A possible explanation for this is that the PEEK table used to clamp the 2 metallic plates could charge up in a similar manner to the etched rims. This would also explain why the rising behaviour is different or happens at shorter timescales due to lack of etched rims in GGEMs.
As well as the long term rising signal over a period of hours, the GGEMs also increase in signal

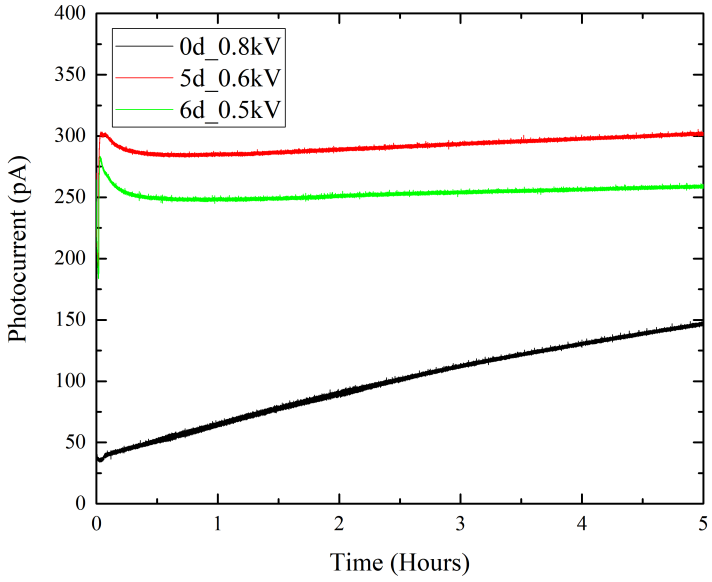

Figure 3.18: Response of GGEM under illumination of deuterium lamp for electrodes left in the chamber over period of days. The number on the left of the legend shows the number of days that the GGEM is left in the chamber and the number on the right shows the HV bias applied

when left in the chamber without any bias or illumination as shown in figure 3.18, just as in the case of normal ThGEMs.
To fully investigate the effect of charging up of dielectric material complete removal of any dielectric material in contact with the metal contacts is required. This is difficult to implement in practice as the two electrodes need to be electrically insulated from each other whilst maintaining structural stability.
There also appears to be a large difference between the small and large chambers in terms of both gain stability and relative gain. Figure 3.19 shows the same GGEM used in figure 3.18 but placed in the larger chamber. It can be seen that in this figure that the size of the rising in the large chamber appears to be much larger. Both setups use a table made of PEEK to mount the GGEMs in a similar fashion, further clarification and control of the various parameters effecting gain stability needs to be reached before we can say with certainty what is causing the rising gain behaviour observed.

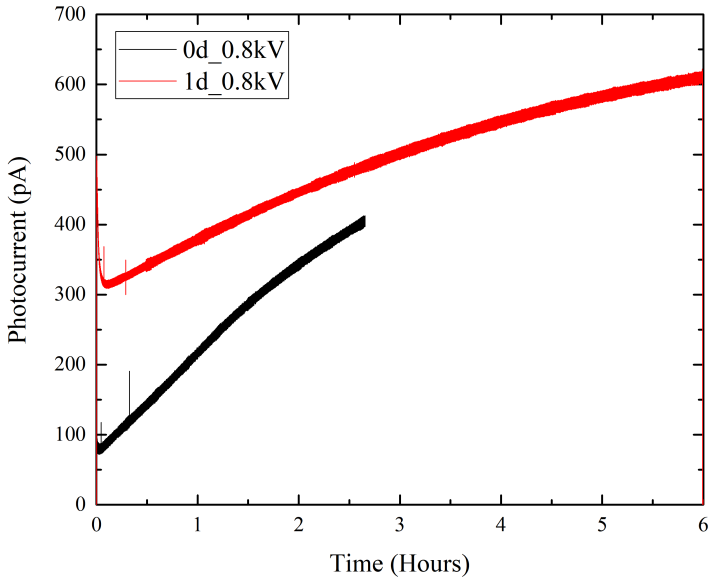

Figure 3.19: Photocurrent as function of time for GGEMs in the larger chamber under illumination of deuterium lamp

Relative Gain

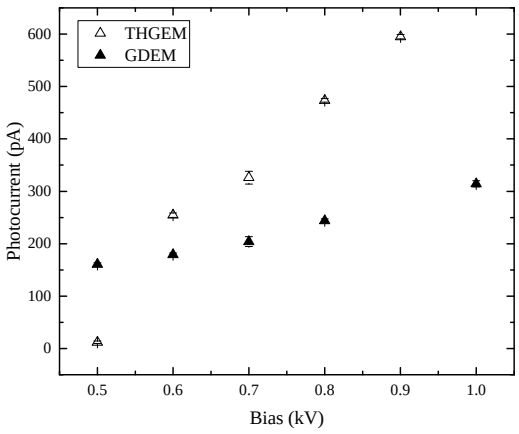

Figure 3.20: Average photocurrent curves for ThGEMS and GGEM.

Figure 3.20 shows the comparison between photocurrent curves of the GGEMs compared to 0.8mm thick PCB ThGEMs with the same pattern etched into the copper with 0.6mm holes that

are mechanically drilled into the surface. The surfaces of both the ThGEMs and the GGEMs were polished with Brasso to get the highest signal possible. The GGEM responses have been multiplied by the ratio of the active photocathode surface areas.
In figure 3.20 the GGEMs and ThGEMs appear to have similar responses, although the gain of the ThGEMs increases more rapidly with higher voltages. The main expected reason for the two structures to be different is the difference in the charging up of the top etched rim in the 0.8mm thick ThGEM. The slightly higher gain at lower biases (i.e. 0.5kV) of GGEMs is most likely due to an improved signal due to the extra yield from secondary photon effects.
Figure 3.21 shows the response of a much larger area GGEMs of 2.8cmx2.8cm. These GGEMS have a multiplication length of 0.8mm and hole sizes of 1.2mm and 1.6mm instead of 0.8mm of the smaller GGEMs. Both GGEMs are under a bias of 0.3kV and have a response of over 600pA for the 1.2mm diameter holes and about starting to settle at around 370pA for the 1.6mm diameter holes.
The current measured for the larger GGEMs is much larger than the smaller GGEMs. However, there are also larger fluctuations in signal compared to the smaller GGEMs, vibrations and microphonics could be likely cause of this extra noise.

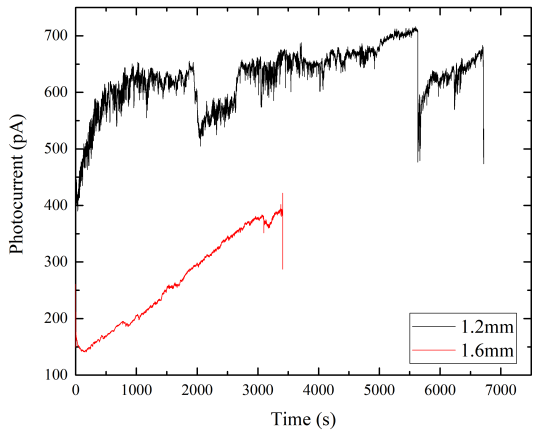

Figure 3.21: Response over time of the larger 2.8cmx2.8cm GGEM

3.8 Conclusions

In this section we have investigated the long term stability of both ThGEMs and GGEMs with different structural properties. In all cases there is always a large rising signal for new electrodes, with varying timescales from several hours to a much longer period of several days. This appears to match the hypothesis from Alexeev et al. [62] that gain stabilization is reached after the slow processes of charges moving within the dielectric along the electric field lines, which

can take on the order of days.
It has been suggested by Pitt et al. [64] and others that the long term increase is due to the charging up of the etched rim on the top electrode from electrons accumulating on this rim increasing the electric field strength. However, this rising behaviour has also been shown to be present for our novel GGEM devices where there is no dielectric in between the electrodes much less any etched rims. This suggests that the hypothesis that the rising signal is due entirely to the etched rims is wrong. However the charging up of dielectric around the electrode may still play a part as although there is no dielectric surrounding the holes in the electrode, there is dielectric surrounding both plates from the table that holds them in place. It is possible that charging up of this table is what causes the increase in signal.
The speed and size of long term rise in signal appears to increase with higher biases or gains. This also agrees with Pitt et al. [64] who showed via simulations that the ratio of long-short term stabilization time is dependent on the drift field as more electrons are collected on the top of the electrode. Also, while there is still some rising behaviour in GGEMs, the signal appears to settle off at quicker rate and does not have an exponentially rising signal present in normal ThGEMs. In fact GGEMs behave in a similar way to ThGEMs with no etched rims, but with a higher initial signal which could be due to secondary photons adding to the overall multiplication.
As well as the possible contribution of dielectric and the surrounding gas building and retaining charge. It is possible that the change in signal could be due to the gas mixture, i.e. from outgassing from components. However, flushing the chamber for 24 hours appeared to have no effect on the rising signal, in contrast to initialization measurements from Cortesi et al. [65]. Baking the chamber to remove residual contamination (such as water) from the chamber before measurement also appeared to make very little difference to the rising behaviour.
Also in an attempt to measure the amount of contamination from outgassing components we setup a small test chamber attached to a mass spectrometer. From the data gathered the only noticeable increase was from air and water, however during the operation of the detector argon is allowed to flow into the chamber which should reduce the amount of air and water leaking in. Also as the increase in gain happens almost immediately and is highly dependent on the HV bias it is much more likely that it is due to the charging up of either the dielectric or gas.
Another piece of evidence towards the rising gain behaviour being not primarily due to the gas mixture in the chamber is the fact that switching from pure Argon to an Argon/CO_2 mix (90:10) did not limit the rising signal, instead it appeared to only lower the gain at a given bias.
Also an important discovery made was that the signal increases for ThGEMs or GGEMs left in the chamber even if they are no longer under HV bias or illumination by light source. This suggests that the electrodes retain a history of their operation unless they are removed from the chamber. Whilst the reason for this is unknown it has also been discovered by Renous et al. [98] who suggested that flushing the electrode with 1 minute of ionized nitrogen removed the charge stored in the electrode. However, as this behaviour is also found to be present in GGEMs it must be the table itself as well as the dielectric between the plates that stores the charge.

Shalem et al. [99] suggested that the optimal geometrical properties for maximum gain is $t/d \sim 1$. However this does not appear to be the case with often slightly smaller hole diameter giving higher measurable photocurrent. However the error in measurement of exact values of photocurrent or relative gain is quite large due to the size of the large term gain fluctuations. Also as mentioned previously the size of the etched rim effects the gain along with its stability, therefore to get a proper comparison of structural properties removal of etched rims and better control of the operational conditions is needed.

Two different photolithographic masks were used to create hole patterns of 2.5mm pitch and 3mm pitch. The 3mm pitch pattern was shown to have smaller output signal, this is expected to be because of the decrease in the number of holes or multiplication channels. Therefore there will be an intrinsic trade-off between the active photocathode area and the number of holes in the ThGEM structure.

The amount of etched rim around the hole appears to also effect the signal, with smaller etched rims (0.1mm thickness) having more rising behaviour and hence a larger signal compared to larger etched rims. This could be due to a reduction of collection efficiency of liberated photoelectrons with the larger etched rim sizes, decreasing the overall gain.

Although it has been mentioned that the long term rise in gain is present in GGEMs, its behaviour does appear to have been changed with the signal settling over shorter time periods, with a less exponential rise present. This could suggest that although the rising behaviour has not been removed it has been reduced. An explanation for this is that the charging up of the table that surrounds the GGEM could be causing the rising in the case of GGEMs, however the removal of the presence of etched rims has reduced the exponential increase seen in ThGEMs.

It has been found that although ThGEMs have a higher signal at higher HV bias (due to the rising in gain) GGEMs have higher signal at lower HV bias. This is most likely due to an increase in gain due to secondary photons that are no longer blocked by the dielectric hole walls.

Whilst the mechanisms behind the long term gain fluctuations are still unknown, we have managed to find behaviour that matches that already found in the literature as well as proof that it is not entirely due to charge accumulation in the rims. Before more detailed structural comparative studies on relative gain are performed we need to understand the gain variation behaviour better and get better control over the operational properties. Further reduction in the dielectric present, i.e. by removing the table holding the GGEM, could allow us to get a better understanding of the charging up behaviour of the environment.

Although the rising gain behaviour is seen as mostly a negative aspect of the operation of the device, due to the large errors in calibration and comparison between different parameters. The rising behaviour can be useful as it vastly improves the signal obtained and once a plateau is eventually reached the signal is very stable and requires much lower HV bias to achieve the same output signal.

Chapter 4

Growth and Characterisation of Metal Oxides

4.1 Introduction

In this chapter we will investigate different potential materials for reflective UV photocathodes, in the UVC range (100nm to 280nm). By using a Kelvin probe to measure the work function and XPS for chemical composition, we will attempt to characterise how both the growth conditions and storage of photocathodes effect their chemical structure and optical properties.
We will also investigate how to effectively tune the work function and therefore the cut off wavelength of our detectors, either by controlling the growth conditions, addition of adsorbates onto the surface or by controlling the stoichiometry of metal alloys grown in vacuum. By having control over the work function of the photocathodes we will be able to determine different wavelengths using multiple photocathodes in a single detector.
The UV photocathodes most commonly used in particle physics consist mainly of either CsI, CsBr or Cs_2Te [100]. These photocathodes often come with the downside of requiring complex fabrication methods and have to be kept under clean vacuum conditions or their quality will quickly deteriorate. Cs_2Te, which is most commonly used for photodetectors has a detection tail out to 325nm which overlaps with the solar spectrum therefore requiring filters and/or expensive optics to make the device solar-blind [101]. As such recently there has been movement towards metal oxide films for solar-blind (SB) UV detection.
Metal photocathodes have been predominately used in high gradient RF guns [102]. Despite having low QY due to electron-electron scattering, metal photocathodes are useful due to their tolerance to vacuum contamination allowing them to be installed at atmospheric pressures and they can survive years at the high cathode fields required to produce high brightness beams.
Although optical properties of clean metal surfaces have been well understood and investigated [103, 104], native metal oxides have not been widely used. As such in this section we will investigate the potential usefulness of native metal oxides as potential UV photocathodes.

Two metal oxides are investigated in this thesis: magnesium oxide and zinc oxide. Polycrystalline magnesium has a work function quoted in literature of about 3.6eV to 3.8eV [105, 106]. Zinc has a work function of around 3.9eV to 4.2eV [107], higher than magnesium and much more similar to copper. However this means that unlike magnesium it is naturally solar-blind.
Alloying of metal and metal oxides has been used to tune the work function and bandgap of various materials. Alloys of GaN such as ($Al_xGa_{1-x}N$) have been widely used for emission and detection of VUV [108]. Whilst alloys of Mg-ZnO have been explored as an alternative to ($Al_xGa_{1-x}N$) [109, 110, 111]. Wurzite ZnO has a direct wide bandgap of 3.4eV compared to the much larger band gap 7.8eV of MgO, therefore the bandgap of ZnO can be easily tuned by addition of small amounts of Mg. Also as Mg ions have similar radii to that of Zn ions there is less strain and efficiency drop off concerns with increasing Mg content when compared to (Al)GaN alloys [112] and corresponding Al contribution. However, increasing the Mg content shifts the structure of the alloy from the hcp phase of ZnO to the fcc phase of MgO which is much more insulating and less suitable for device applications [101]. Bandgap engineering deeper into the UV spectrum has also been demonstrated by additional alloying with Al [113].

4.2 Copper

In this section, by measuring the work function of the standard copper surface of the PCB that is used to manufacture ThGEMs and using XPS data to investigate its chemical composition, we will investigate how different cleaning methods effect the oxidation state of the copper surface and, in turn, how this effects the work function measured.

4.2.1 Work Function Measurements

Many different factors can affect the work function measured and throughout the literature there is a large variance in the expected value. The work function of copper for clean polycrystalline copper is given as around 4.5eV by multiple references [114, 115] but can vary from 4.4 to 4.8eV [116, 117] with the surface roughness and strain on the surface. The absorption of oxygen is also known to cause the work function to increase anywhere from 0.125eV to 0.675eV for single crystal faces [118] and Cu_2O has been quoted to have a WF as high as 4.84eV [119]. As such it is difficult to know exactly what work function our copper surface will have and we have to rely on our KP measurements and calibration performed in section 2.2.4.
As mentioned previously by polishing the copper surface with Brasso, instead of the standard solvent cleaning method using in the fabrication of the ThGEMs, the photocurrent measured increases significantly. To investigate this effect further we will look at the CPD of the copper surfaces using the different cleaning methods.
Table 4.1 shows the average CPD and WF measured using the KP for copper surfaces under

different cleaning processes: A 5 minute ultrasonic bath of 50:50 acetone and isopropanol solution is always done first to remove the photoresist from the PCB then the surfaces are either polished with Brasso or subsequently cleaned with a solution of 5% Micro-90 cleaning solution and distilled water in an ultrasonic bath for 5 minutes.

From the table it can be seen that the main source of error is the determination of the tip work

Cleaning Method	CPD (mV)	Error	WF (eV)	Error
Solvent	-180	20	4.52	0.07
Brasso	-260	30	4.44	0.08
M90(5%)	-660	25	4.04	0.07
Water	-50	10	4.65	0.07

Table 4.1: CPD measured for copper surfaces under different cleaning methods

function (0.07eV). With the error during measurement and between samples of similar conditions having a smaller error.

The solvent cleaned copper has a very similar WF to that found for clean polycrystalline copper in literature [114, 115], where Brasso cleaned copper showed slightly lower WF, but still within error.

Interestingly, the samples cleaned in the micro90 solution resulted in much lower measured WF, this could be due to the absorbed water on the surface, as it has been shown that this can reduce the WF significantly. However, Cu surfaces cleaned in standard solvent and following distilled water bath showed a higher WF in contrast to the literature [120, 121] where the work function is shown to decrease as much as 1eV for water absorbed onto clean copper surface.

As well as absorption of water, oxygen and other contaminants can cause significant changes to the work function measured, there is often a large variation across different patches on a surface as shown by figures 4.1*a* & 4.1*b* which show the CPD measured over several points on the same sample surface for solvent cleaned and Brasso polished Cu surface respectively. The time in between each measurement was small, so significant changes due to absorption of contaminants are unlikely.

The standard deviation across a single sample is about 30mV for both samples, however for some samples this deviation can be even larger especially in the case of vacuum grown samples that can sometimes have non-uniform or patchy films. The size of this variance across a sample limits the ability to detect small work function changes on a sample, without having multiple scans across the sample surface or measuring the exact same position on the sample.

Despite causing a large increase in the QY, the WF of the polished copper surfaces is similar to fresh copper samples cleaned in solution. Further proof of polishing not affecting the work function of the copper surface is that polishing already measured solvent cleaned copper surfaces showed no measurable change. This suggests that the improvement in response is not due to a shift in the work function as any change measured is too small to explain the amount of extra output signal achieved. Therefore, it is more likely that the quantum yield has been increased

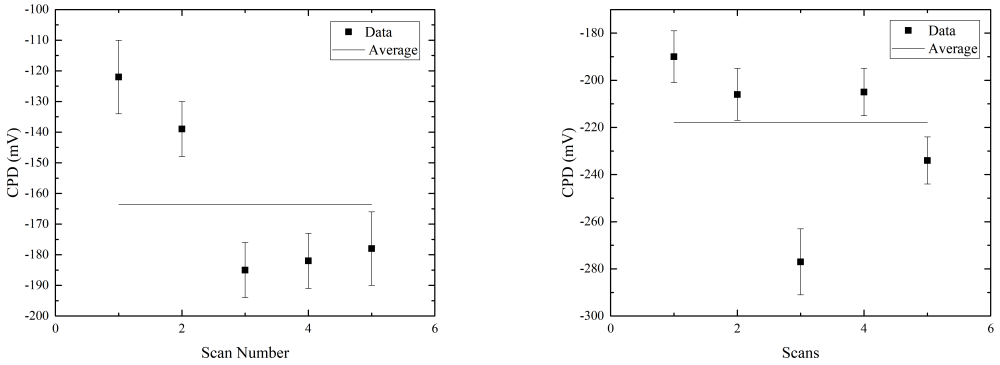

(a) (b)

Figure 4.1: CPD variations across a single copper sample for a) Solvent Cleaning & b) Brasso polished surface

instead, by a change to either the surface roughness or composition of the surface. Li et al. [116], showed a reduction in surface roughness causes the WF to increase. This change has not been noticed in the WF measurements between solvent cleaned and the polished Cu surfaces. Therefore the most likely candidate for increase in signal is a change in the composition of the surface.

Figure 4.2 shows the CPD measurements over a period of 20 days of copper surface both sol-

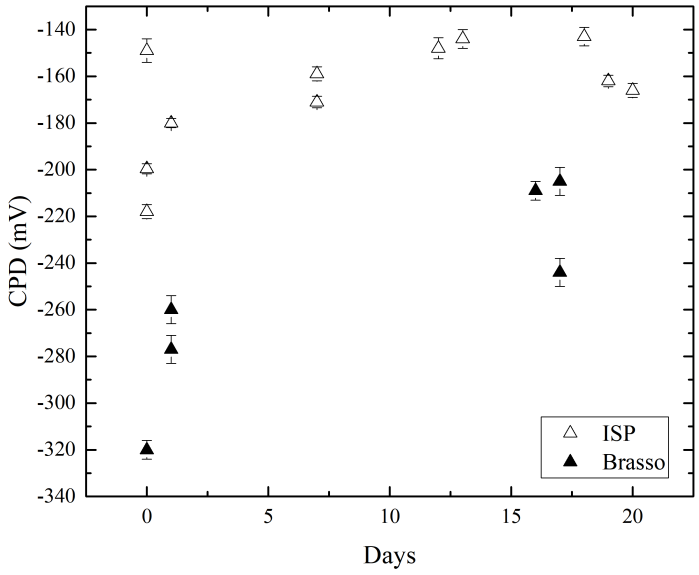

Figure 4.2: CPD measurements for a solvent cleaned ThGEM over a period of 20 days exposed to ambient air

vent cleaned and polished with Brasso exposed to ambient air. It can be seen that there may be an initial rise in work function, but this happens over a period of around a few days, after that the work function appears to remain reasonably stable. The initial rise is more noticeable for Brasso polished samples, with a ΔWF of about 0.1eV.

4.2.2 XPS Measurements

Fitting

The first step in fitting the XPS data is to fit C 1s and perform charge correction off the main C-C/C-H peak. A value of 285eV was chosen to correct the main peak to, although the value for adventitious carbon can be anywhere from 284.7eV to 285.2eV [122]. General adventitious carbon also have peaks at higher B.E.: C-OH and or C-O-C peak can be found around 1.5eV higher than the main peak with FWHM same as the main peak, C=O can be found 2.8eV to 3eV higher and a O-C=O can be found 3.6-4.3eV higher. An example fitted C 1s for the copper samples is shown in figure 4.3. Some of the copper samples show a separate peak in the C1s at around 6eV higher than the main C-C/C-H peak which has been attributed to a type of carbonate.

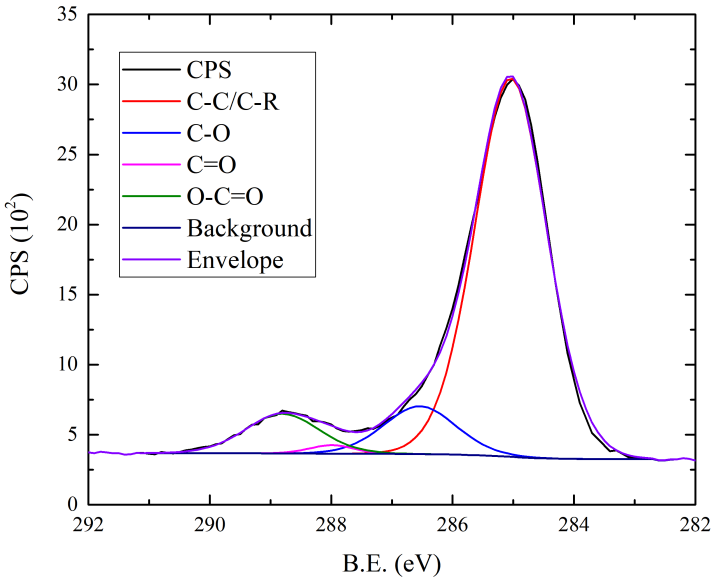

Figure 4.3: Example of fitted components of C 1s for Cu samples

The metallic peak in the Cu 2p region is agreed to be around 932.6 ± 0.2eV from multiple references [123, 122]. Copper also exists in two stable oxides (Cuprous oxide Cu_2O and Cupric oxide CuO).

Chemical determination of the oxide components from the Cu 2p3/2 region is difficult due to the overlapping of Cu_2O with the metallic peak and CuO with CuOH. However the introduction of copper oxide and hydroxide results in a satellite peak around 945eV. Borkar et al. [124] suggested that a weak satellite shows presence of Cu_2O and a large, broad satellite peak supports the presence of CuO.
To distinguish the chemical state of the copper oxides the copper auger spectra is also taken and the modified auger parameter is used to assign chemical state as there is a bigger chemical shift for the Cu LMM compared to the Cu 2p region.
As in the case of the Cu2p region the Auger spectra has overlapping peaks, a resultant shift to lower kinetic energies and a broadening of the main peak are indications of the presence of CuO and Cu_2O respectively.

Analysis

To investigate the reason for the large rise in signal from manually polishing the copper surface with Brasso, we have taken XPS data for both unpolished and polished copper surfaces.
Figure 4.4*a* & 4.4*b* show the Cu auger spectra for both solvent cleaned and polished copper sur-

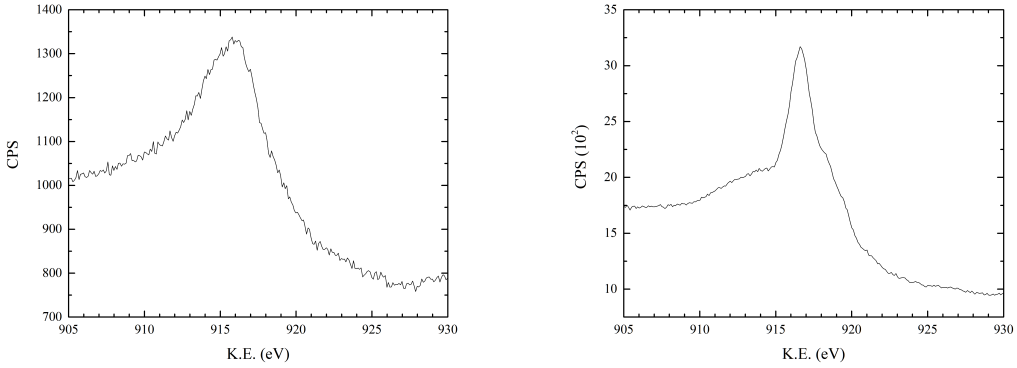

(a) (b)

Figure 4.4: Auger spectra for a) solvent cleaned copper & b) Brasso polished copper

faces. The solvent LMM spectra shows a much wider central peak which has also been shifted to a slightly lower K.E. which is respective of a larger contribution of Cu_2O and CuO, whereas the larger thinner central peak at about 917eV is more indicative of a strong metallic contribution.
Figures 4.5*a* & 4.5*b* show the Cu 2p3/2 region for untreated and treated copper respectively. The mechanically polished samples have a vast reduction in CuO and CuOH present, the peak shape for the polished copper matches that for sputter cleaned Cu surface from Biesinger et al. [122]. The lack of satellite peaks around 938-947eV in the polished copper 2p region is further evidence of lack of CuO and CuOH, as these satellite peaks are characteristic of divalent copper

[125].

All the peak shapes for the components in the Cu2p region are GL(30) except the small Cu_2O

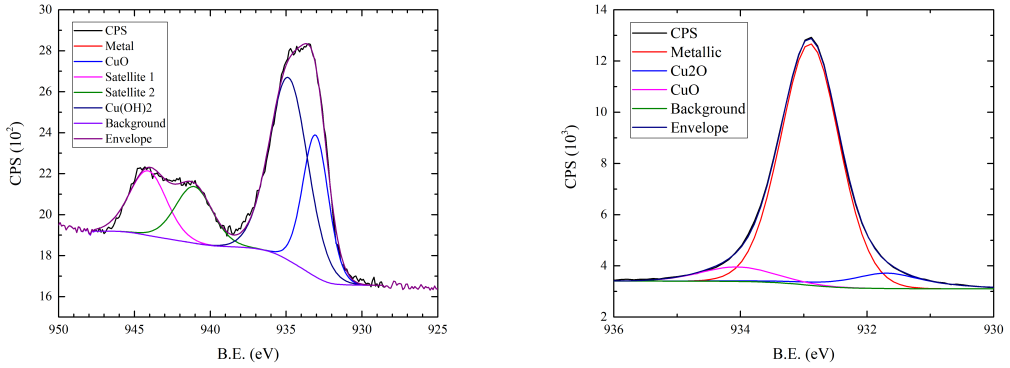

(a) (b)

Figure 4.5: XPS Cu2p3/2 regions for a) solvent cleaned & b) polished copper surfaces

component in the polished copper substrate which has a peak shape of GL(90) as suggested by Biesinger et al. [122].

The XPS spectra for the solvent and Brasso cleaned copper surfaces suggest that when the surface is polished with Brasso it removes most of the upper layer of CuO leaving behind pure metal with small amount of CuO and Cu_2O.

We have also taken XPS of copper surfaces cleaned with a solution of Micro-90 and distilled water. For these samples an extra peak at around 1071.7eV is present in the XPS spectrum. This has been attributed to a Na 1s peak and it matches very closely what was found in Kishi et al. [126] for NaCl deposited on Cu(100) surfaces. This is most likely because the cleaning solution contains 10 to 25% ethylene diamine tetraacetic acid tetrasodium (EDTA-Na_4) and some residual Na is left on the surface after cleaning. Apart from the extra Na 1s region present the Cu2p3/2 region for M90 cleaned copper surfaces looks very similar to the solvent cleaned copper samples.

It is possible that the Na ions on the surface of the copper results in a surface dipole effectively reducing the work function measured with the Kelvin probe. As alkali metals have a single valence electron that is weakly bound they are very electropositive and have low work function [127] and have been known to produce large changes in work function of various metals and metal oxides [128].

4.3 Magnesium Oxide Films

4.3.1 Work Function Measurements

As in the case for copper there is some discrepancy for the values of work function stated in the literature for magnesium and magnesium oxide. For clean polycrystalline magnesium a work function of 3.66eV has been measured via photoemission in Yuan et al. [106]. Hayden et al. [105] and Lange et al. [129] both measured the work function for single crystal magnesium samples with increasing oxygen exposure. They showed that the work function decreased by as much as 1.3eV for work function measured by photoelectric effect, also for samples measured by KP the reduction was less than 1eV for Mg(001) and slightly more than 0.5eV for Mg(100). Magnesium films are grown by PVD using the vacuum chamber described in section 2.1.1. During deposition the temperature of the crucible is measured and this is how the deposition flux is controlled.

The flux can be calculated by the Hertz-Knudson equation in section 2.1.1, however we are only interested in a qualitative comparison of work function measured versus amount of deposition. It can be seen from the Hertz-Knudson equation that at a given distance the flux at the sample is,

$$dN/dt \propto \sqrt{T}(p^* - p) \tag{4.1}$$

Using this equation, the measured CPD is plotted against a parameter called 'deposition amount' in figures 4.6*a* and 4.6*b*, which is $\sqrt{T}(p* - p)$ multiplied by the deposition time in minutes. Both the temperature T and the pressure in the chamber p were measured during growth. The vapour pressures at a particular temperature were taken from Yaws et al. [130].

From figure 4.6*a* it can be seen that for samples oxidised under vacuum, the measured work

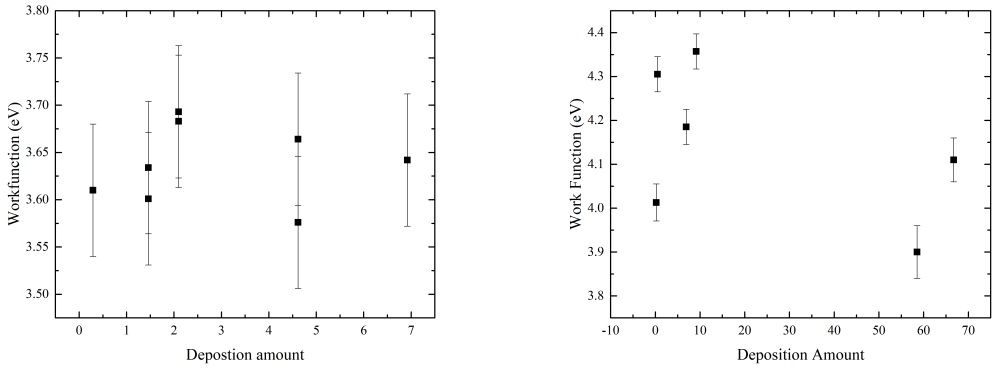

(a) (b)

Figure 4.6: CPD measured for magnesium oxide films grown via PVD with a) oxidation in vacuum during growth and b) letting samples oxidise naturally in ambient

function is consistent at about 3.64 ± 0.04eV. Alternatively, figure 4.6*b* shows the WF of MgO

films left to oxidise in ambient conditions, instead of being oxidised in vacuum during growth and the mean WF of these films is 4.15 ± 0.17eV.

The WF for MgO oxidised in vacuum is very close to the expected value of 3.66eV [131]. However, the samples exposed to ambient conditions without any oxidation in vacuum appear to have a higher work function than found in the literature.

Figure 4.7 shows the change in CPD over time for a MgO film left in ambient. The MgO film in question was deposited at a crucible temperature of $560°C$ for a deposition time of 20 minutes, and appeared to be a thick film fully coating the copper. This sample was oxidised using a leak valve attached to the main part of the chamber. From the graph we can see that the work function actually gets lower over time (more negative CPD). This suggests that the sample also continues to oxidise or change oxidation state after being left out in ambient air.

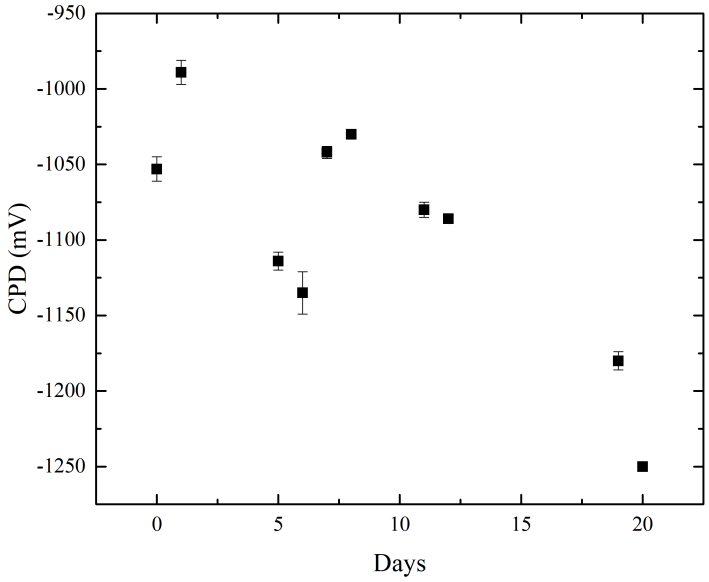

Figure 4.7: Multiple seperate CPD measurements of a single MgO film over a period of days

4.3.2 XPS Measurements

Fitting

As in the case of the copper photocathodes, we must first fit the C1s region and charge correct the spectrum by moving the main C-C peak to 285eV, this correction will then be used on the rest of the regions. The C1s region for Mg films has the same adventitious carbon component peaks present in the case of copper surfaces but there is additional peaks both about 5 eV higher and 2eV lower than the main hydrocarbon peak, these additional peaks have been attributed to

the $MgCO_3$ and graphite respectively as similar peaks were found to be present in Fournier et al. [132], who proposed the explanation that graphite particles are formed by decomposition of hydrocarbon molecules.

To figure out the chemical state of the magnesium atoms in the film we need to fit the different components in the Mg2p region, however the binding energy shifts between the different chemical states are very small and they can overlap causing difficulty in fitting, in particular MgO and $Mg(OH)_2$ have been found to have almost the same peak binding energy [132]. The metallic peak has the largest B.E. shift from the Mg^{2+} components and is therefore the most discernible. Different sources state the peak binding energy of the metallic peak to be between 49.6eV and 50.2eV [132, 133, 134], however these values have been charge corrected using a value of 286eV for the C-C peak so our expected B.E. for the metallic peak should be 1eV lower.

Another difficulty is that the spin-orbit splitting of Mg $2p_{1/2}$ to $2p_{3/2}$ is very small (only about 0.28eV), therefore the two contributions overlap adding to the complexity of fitting the 2p region, whilst fitting the Mg 2p region we need to add both peaks with the constraint that the areas will have a 1:2 ratio as explained in section 2.3.

We will also fit the O 1s region to try to get an idea on the oxidation state of the magnesium film by using the intensity ratios. Just as in the case of the Mg2p region there are only small shifts between the different components, however in this case it is the $Mg(OH)_2$ & $MgCO_3$ components that have the most similar peak binding energies. The peak binding energy of MgO is cited to be between 530.9eV and 531.7eV, with $Mg(OH)_2$ having peak binding energy about 0.9eV to 1.4eV higher and $MgCO_3$ 1.5eV to 2.3eV higher [132, 133, 134].

To fit the Mg2p region Fournier et al. [132] estimated the intensities of the peaks from the stoichiometry of the elements in the different compounds. Using the ratios shown below we will estimate the intensities of MgO and $Mg(OH)_2$ from their respective peaks in the O1s region as they have larger B.E. separations.

$$\left(\frac{I_O}{I_{Mg}}\right)_{MgO} = 5.7 \tag{4.2}$$

$$\left(\frac{I_O}{I_{Mg}}\right)_{Mg(OH)_2} = 12 \tag{4.3}$$

For samples that have undergone solvent cleaning before Mg deposition all show a Cl 2p peak present as well, same as in the case of copper samples.

Analysis

To investigate the effect of oxidising the Mg films in vacuum compared to out of vacuum we have done XPS on several samples oxidised in different ways.

Figures 4.8*a* and 4.8*b* show the fitted C1s regions for samples oxidised in air and oxidised in vacuum during growth, respectively. The sample that was oxidised in air was measured to have a work function of 4.36 ± 0.07eV and the sample oxidised in vacuum was found to have a work

function of 3.9 ± 0.08eV, both samples having higher WF than that found in literature for that of polycrystalline Mg.

It appears that the sample oxidised in air has a larger carbide and C-O component and a smaller

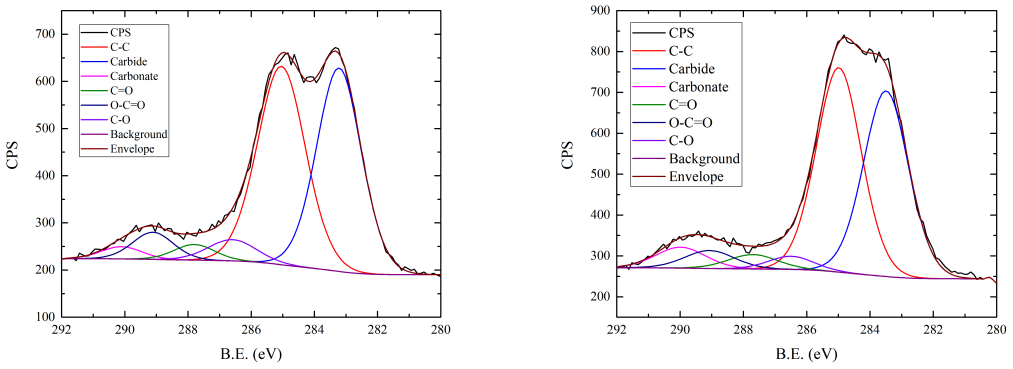

(a) (b)

Figure 4.8: Fitted C1s regions for Mg films a) oxidised in air & b) oxidised in vacuum

carbonate component, suggesting there is actually more $MgCO_3$ on the surface of samples oxidised in vacuum compared to in ambient.

Figures 4.9*a* and 4.9*b* show the corresponding O1s region for these two samples. The $Mg(OH)_2$ component was fitted around 1.4eV higher than the MgO and the $MgCO_3$ was fitted around 1.9eV higher and MgO was fitted at around 530eV to match the values from Fournier et al. [132].

From the O1s regions we can see that the sample oxidised in ambient conditions has a larger

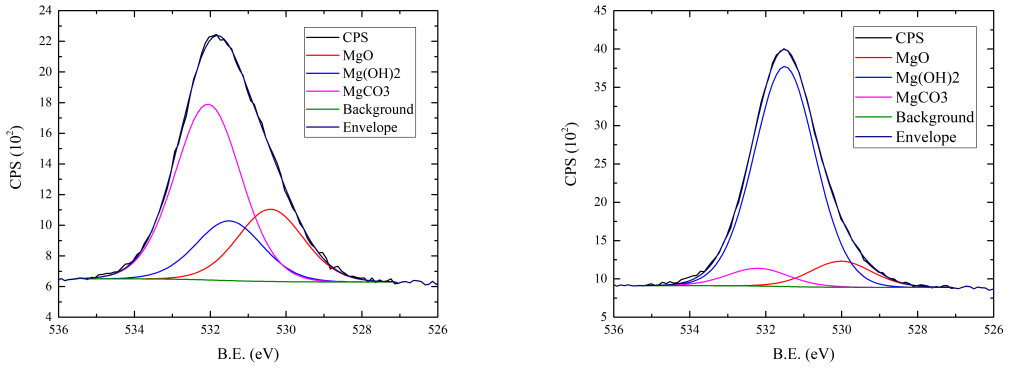

(a) (b)

Figure 4.9: XPS spectra of O1s region for Mg films oxidised a) in ambient air and b) during growth in vacuum

$MgCO_3$ component in contrast with the C1s region, with the sample oxidised in vacuum having most of the oxygen present in $Mg(OH)_2$. This is most likely due to the difficulties in getting

quantitative measurements out from the data due to the overlapping of different components and the contribution of organic C-O and C=O peaks, however we can make some relative comparative measurements from the C1s region.

It is surprising that the sample oxidised under vacuum conditions has a larger $Mg(OH)_2$ component as it would be expected that the sample with increased exposure to ambient conditions (and more importantly humidity) would have a larger $Mg(OH)_2$ component.

Figures 4.10*a* & 4.10*b* show the fitted Mg2p regions for these two samples, using the intensity

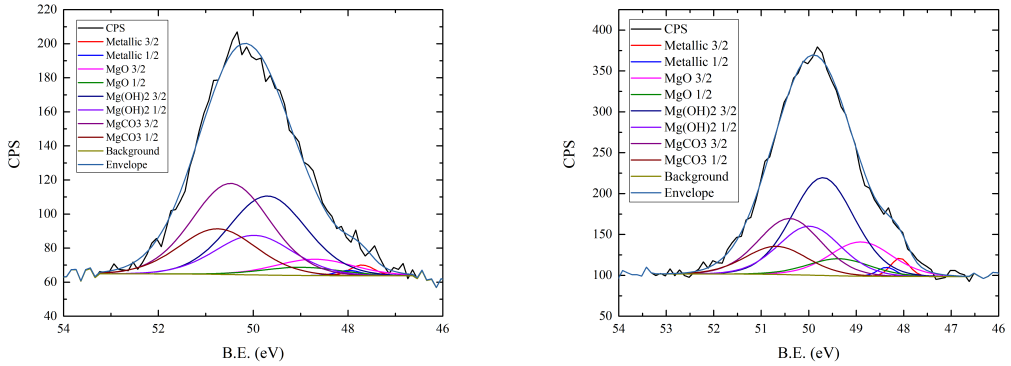

(a) (b)

Figure 4.10: Fitted Mg2p region for a) sample oxidised in ambient and b) oxidised during growth under vacuum

ratios from equations 4.2 & 4.3 to constrain the intensities of the MgO and $Mg(OH)_2$ peaks. Although there is difficulty in quantification due to the overlapping peaks we can compare the two samples by their relative concentrations of Mg and their corrosion products. Also the O1s region, the sample oxidised under vacuum shows a large $Mg(OH)_2$ component as well as a larger metallic component suggesting a thinner corrosion product layer.

We also performed XPS on a variety of films left in ambient conditions for a range of time from over a year to a couple of days.

Figures 4.11*a* & 4.11*b* show the Mg 2p region for two samples: one left in ambient conditions for over a year and one left in vacuum storage for a couple of days.

The sample left in ambient conditions for over a year was found to have a stable WF of 3.64 ± 0.07eV and the sample grown and kept under vacuum conditions was measured to have a WF of 3.48 ± 0.08eV. Despite relatively similar WF the two have very different chemical structures, the sample left in ambient conditions appears to have a much larger metallic component than the sample stored in vacuum conditions, although this may seem surprising it could be explained by the fact that the film on the sample left in ambient conditions being much thicker. Another noticeable difference between the two films is that the samples left in vacuum conditions had a larger carbonate component in the corrosion products layer, whereas in the case of the sample left in ambient although there was still a large carbonate component there was an increase in the

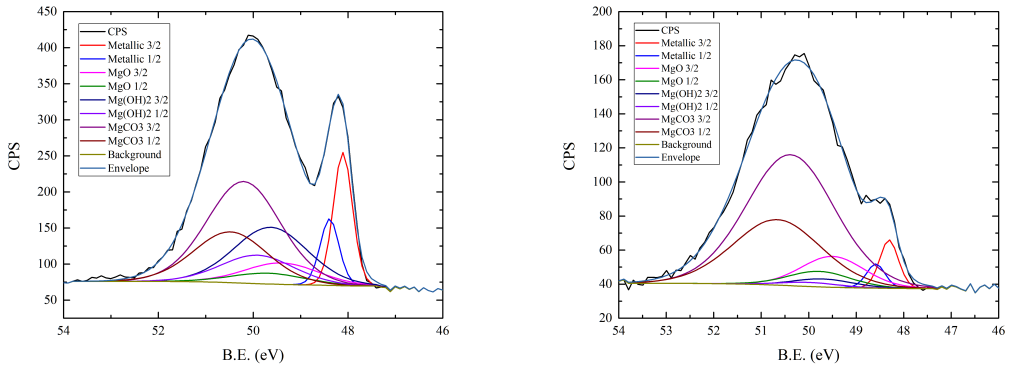

(a) (b)

Figure 4.11: Fitted Mg2p region for a) MgO film left in ambient conditions for a long period and b) MgO film recently deposited in vacuum

amount of MgO present. This suggest the decrease in WF observed from samples being left in ambient conditions could be due to an increase in the amount of MgO in the corrosion product layer.

4.4 Zinc Oxide Films

Just as in the case of copper and magnesium photocathodes, zinc photocathodes also have a range of possible work function values across the literature. Klein et al. [135] gives a range of work function values between 3.5eV and 5.2eV for magnetron sputtered zinc oxide films. The range of values of work function were attributed to a change in Fermi level which was dependent on oxygen content of the sputtered gas.

Moorman et al. [136] measured the work function of single crystals of zinc oxide using the Kelvin method. The work functions were found to be 4.45eV (zinc face) and 4.75eV (prism face) for freshly cleaved samples which then decreased to 3.9eV (zinc face) and 4.55 (prism face) with subsequent annealing to 700K.

Gutmann et al. [107] found using ultraviolet photoemission spectroscopy (UPS) and low intensity x-ray photoemission spectroscopy (LIXPS) that the work function for an annealed ZnO film is 4.22eV.

4.4.1 PVD

As in the case for MgO films, we plot the measured work function of deposited films as a function of a quality called 'Deposition Amount' ($\sqrt{T}(p^* - p)$). The vapour pressure at a particular temperature was calculated from an analytical equation from Aldred and Pratt [137].

Figure 4.12 shows the WF of zinc oxide films grown with oxygen leaked in during growth, these films have a reasonably consistent work function with a mean of 4.11 ± 0.06eV. Figure 4.13 shows the work function of ZnO films oxidised in ambient, these films have a slightly higher WF of 4.35 ± 0.12eV. Also the standard deviation for samples oxidised in ambient is larger, suggesting that the oxidation is less controllable outside of vacuum conditions. The average work function measured however matches with a reasonable degree that found for freshly cleaved zinc [107].

Figure 4.14 shows the average work function measured for ZnO films left in ambient conditions

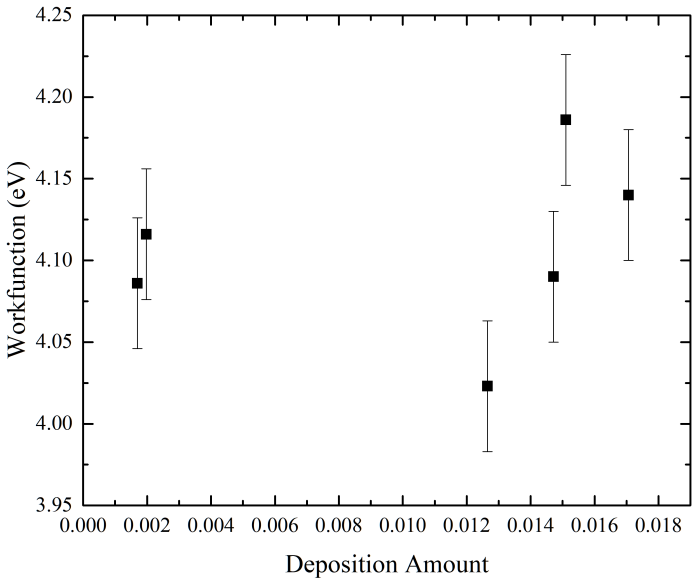

Figure 4.12: CPD measurements of ZnO films grown in vacuum with oxygen leaked in during growth

over a period of 8 days. As can be seen from the graph the work function tends to increase to about 4.35 ± 0.11eV, similar to the values of single crystal fresh cleaved ZnO from Moorman et al. [136], or the values of WF measured for samples oxidised in ambient conditions. This value of work function does not change over very long periods of time, samples measured over a year later showed little to no change in their measured work function.

4.4.2 Electrochemical Deposition

This section shows the KP measurements of zinc films deposited electrochemically using the setup described in section 2.1.2.

Figure 4.15 shows the work function of various electrochemically deposited zinc films all performed at a bias of 1.3V for varying deposition times. Despite the large spread in the data with

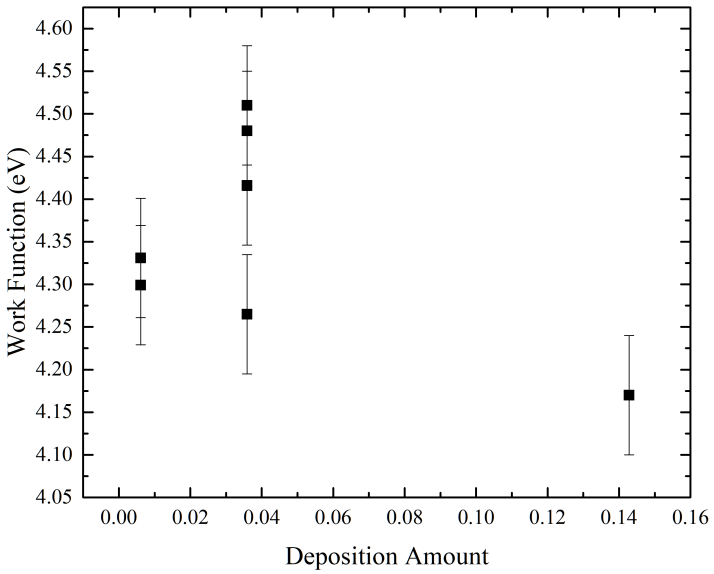

Figure 4.13: WF measured for ZnO films oxidised in ambient

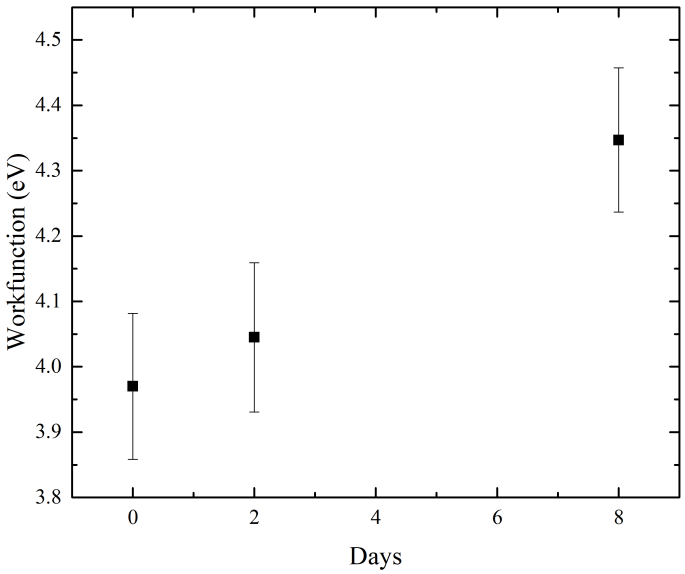

Figure 4.14: Mean work function of samples left in ambient over a period of 8 days

increased deposition time the measured WF appears to be decreasing to a value similar to the values of the samples grown via PVD. For the samples for lower deposition time the average WF is 4.4 ± 0.16eV.

Figure 4.16 shows the work function of two different zinc samples electrochemically deposited, with exposure to ambient air over a period of 20 days. It can be seen that the film with a thicker zinc coating and more negative CPD increases to a similar value to the less negative CPD sample and also the PVD sample. This suggests that this is when the chemical state of the zinc film has settled to a stable state at the point of 8 or 10 days of exposure to ambient air where it settles to a work function of about 4.35 ± 0.04eV, which is a very close value to where the PVD samples settle.

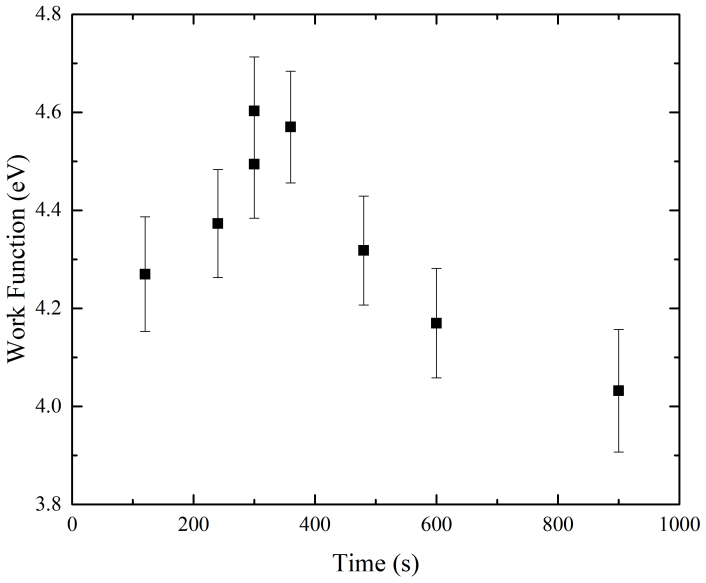

Figure 4.15: Work function measurements performed using Kelvin Probe for various electrochemically deposited zinc films as a function of deposition time

4.4.3 XPS Measurements

Fitting

Much like in the case of the Mg samples we first do a charge correction on the data by fitting the C 1s peak and correcting the C-C component. However this time the C-C is moved to 285eV, close to the value of 284.8eV used in Diler et al. [138] . This correction is then propagated to the rest of the regions in that sample. Then the separate narrow scan components can be fitted. The 2p3/2 region is the most intense therefore this is the one that we use for fitting the different components. The fitting of Zn 2p3/2 and its corresponding components is non-trivial due to the spread in data from literature and the overlapping of various states and components. As such, the modified Auger parameter α' (mentioned in section 2.3, is useful as a marker of specific

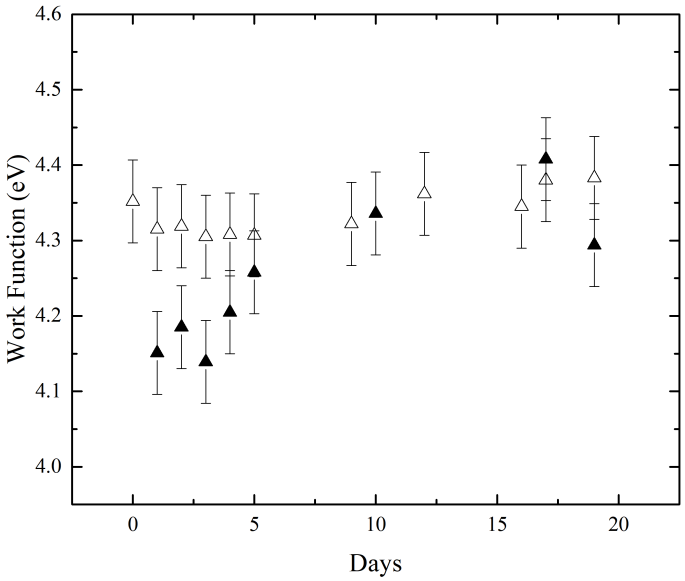

Figure 4.16: CPD measurements over a period of days exposure for electrochemically deposited zinc films

chemical state, especially for ZnO which has a very small binding energy shift from the metallic peak, but its value of α' is very consistent. Due to the non-conducting properties of ZnO films there is significant charging effect which does not effect the modified auger parameter.

Dake et al. [139] measured a large number of zinc compounds and established tables of B.E.

Component	2p3/2 B.E. (eV)	LMM K.E. (eV)	alpha' (eV)
Zn	1021.6	992.2	2013.8
ZnO	1022	988.1	2010.1
$ZnCO_3$	1022.3	987.4	2009.8
Hydrazincate	1022.5	987.1	2009.5
$ZnCl_2$	1023.5	986.2	2009.7
$Zn(OH)_2$	1022.7	986.5	2009.2

Table 4.2: Binding energies and modified auger parameters for Zn and its components taken from Dake et al. [139]

and α' as shown in table 4.2. Although as a starting point there are some discrepancies throughout the literature on these values, mostly with $Zn(OH)_2$ which has been reported to be 2009.9 and 2010.4eV by Deroubiax et al. [140] and Moretti et al. [141] respectively.

A potential explanation of the variance of α' of $Zn(OH)_2$ is hypothesised by Duchoslav et al. [142] who suggested that $Zn(OH)_2$ decomposes to ZnO at lower temperatures when undergoing XPS, which explains why it reaches values close to $\alpha'_{ZnO} = 2010.1 - 2010.4eV$.

Another indication of the oxidation state of the zinc oxide films can be found in the O1s region

as it is well documented that there are two peaks one at around 530eV which is known to be attributed to the ZnO lattice [122] and one at 532eV which is attributed to $Zn(OH)_2$ and other contaminants [140, 138].

4.4.4 Analysis

To investigate the effect of oxidisation in vacuum for the ZnO films grown we have done XPS on films that have been oxidised during growth and after growth, both via leaking in O_2 using a leak valve. Figure 4.17 shows the LMM spectra of 3 different samples, a clean sample oxidised under vacuum (WF=3.72 ± 0.09eV), an older sample left in ambient air (WF=4.06 ± 0.03eV) and a sample grown via electrochemical deposition (WF=4.37 ± 0.04eV).

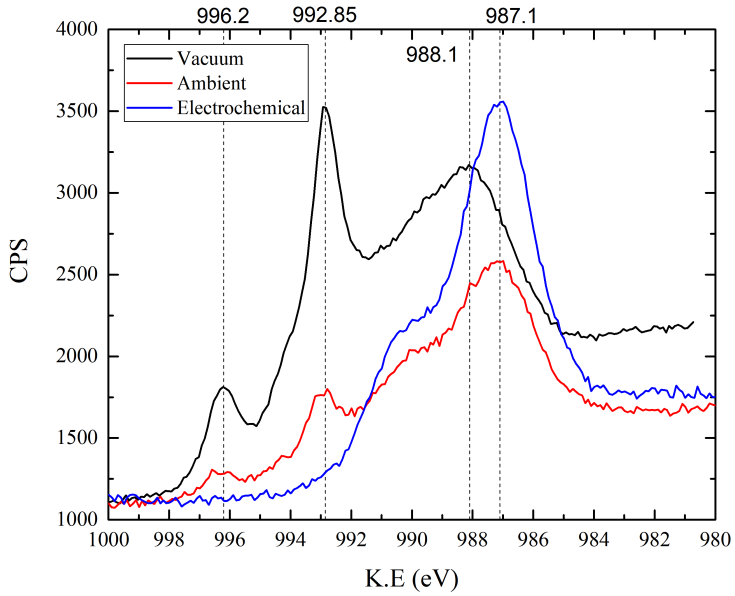

Figure 4.17: LMM spectra of 3 ZnO films: oxidised in vacuum, left in ambient and grown via electrochemical deposition

The sample oxidised in vacuum shows a strong peak at 992.85eV and 996.2eV which although a bit different from the values in Dake et al. [139] is attributed to the metallic Zn. This sample also has its other peak shifted to lower binding energy compared to the ambient and electrochemical sample. The peak at 987.1eV is from the $Zn(OH)_2$ or other hydroxide components, which are likely to be high in electrochemical deposition as it is deposited in solution with distilled water, whereas the peak at 988.1eV will be a convolution of ZnO and $ZnCO_3$.
Figure 4.18*a*, 4.18*b* and 4.18*c* show the O1s region for the same three samples. From these figures it can be seen that the electrochemical and ambient sample show a larger $Zn(OH)_2$ to ZnO

ratio, which confirms the hypothesis that this was the reason for the shift in the kinetic energy of the LMM spectra.

It appears that the larger ZnO component results in a lower the work function of the sample and the more $Zn(OH)_2$ or hydrazincite present the higher the work function. Figures 4.19*a*, 4.19*b* and 4.19*c* show the Zn 2p3/2 region for the same three samples, using the modified auger parameters to label the components to their possible chemical states, the peak shape LA(1.4,2,2) was used for the metallic component as in Biesinger et al. [122]. From the 2p3/2 region it can be seen that the sample oxidised in vacuum has a much larger metallic contribution which again matches the auger spectrum. Also the electrochemically deposited ZnO film has even smaller metallic component suggesting that there is an even thicker hydrazincite layer.

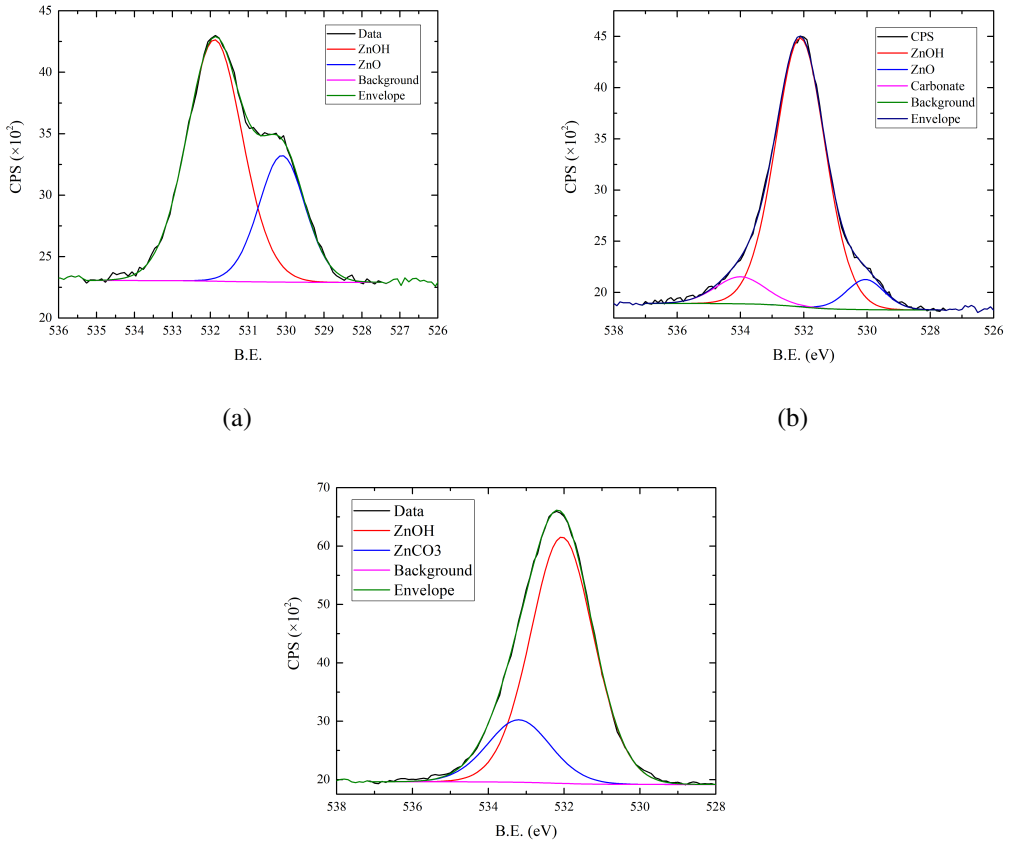

Figure 4.18: O 1s region for ZnO films a)oxidised in vacuum, b)left in ambient conditions and c)deposited via electrochemical deposition

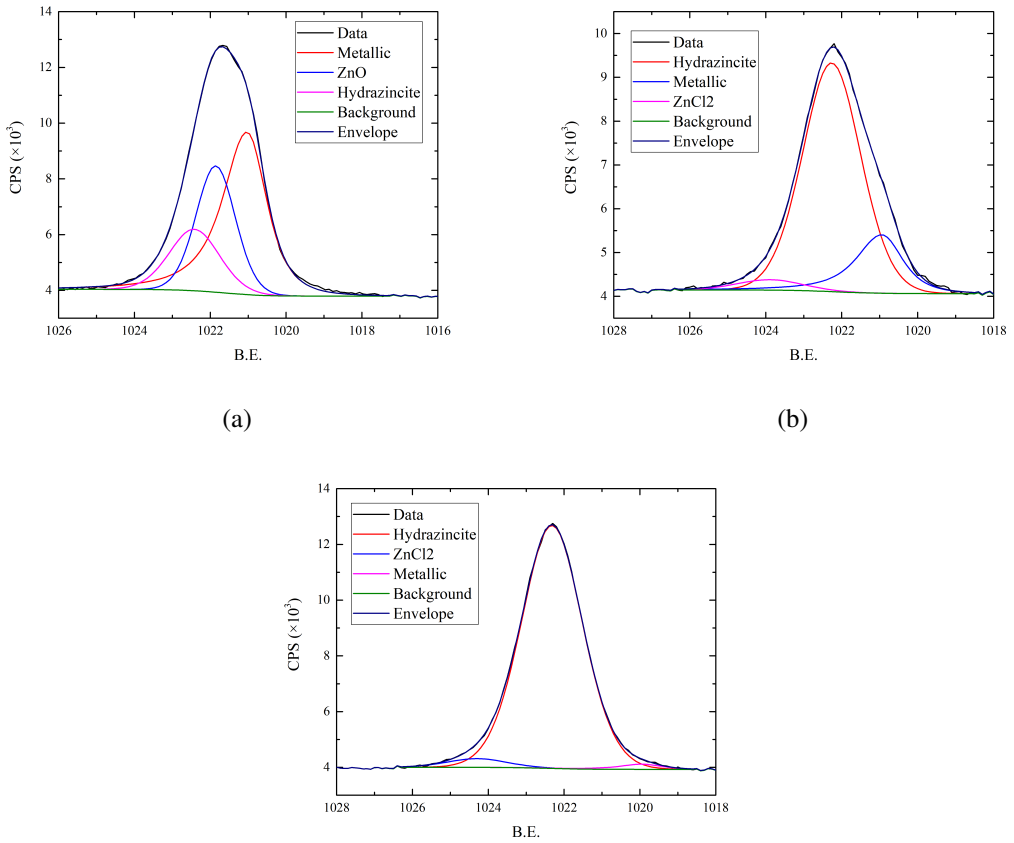

Figure 4.19: Zn2p3/2 region for a)sample oxidised in vacuum b)left in ambient and c)electrochemically deposited

4.5 Work Function Modifiers

Also of interest is the possibility of tuning or modifying the work function of our photocathodes using post-deposition treatment. One particular way of doing so is to coat the photocathodes in an ultrathin layer that is chemically or physically absorbed onto the surface which creates a strong interface, molecular dipole or contribution of both which in turn will induce a shift in the Fermi level of the conductor and lower the work function.

Zhou et al. [143] showed that polymers with simple aliphatic amine groups, polyethylenimine ethoxylated (PEIE) and branched polyethylenimine (PEI), could reduce the work function of a variety of different conductors. Chemisorption of tetrakis(dimethylamino)ethylene (TDAE) has also been demonstrated to cause reductions in work function for Au [144]. However, due to TDAE's instability in air it has found limited use, whereas PEI & PEIE can be easily processed in air from dilute solutions of water or alcohol, which remain stable for more than a year in ambient conditions.

Zhou et al. [143] also showed, by washing away islands of thicker PEIE without the WF being affected, that only a ultra-thin layer is needed to produce the WF changes seen. Whilst extra PEI or PEIE seemed to not affect the work function, it was found to hinder device performance with increasing PEI/PEIE thickness due to its insulating nature.

Zhou et al. [143] gave KP measurements of the work function changes in air, with a 0.98eV, 1.2eV, 0.9eV & 0.65eV ΔWF for ZnO, Au, Ag & Al respectively after depositing a thin layer (10nm) of PEIE on the surface and 1.16eV, 1.16eV, 1eV for ZnO, Au & Ag with a deposition of a thin layer (10nm) of PEI.

In this section we will coat layers of PEI and PEIE of varying thickness on our various photocathodes and measure the WF reduction using the Kelvin probe.

Figure 4.20 shows the change in work function from copper films coated in PEI at different

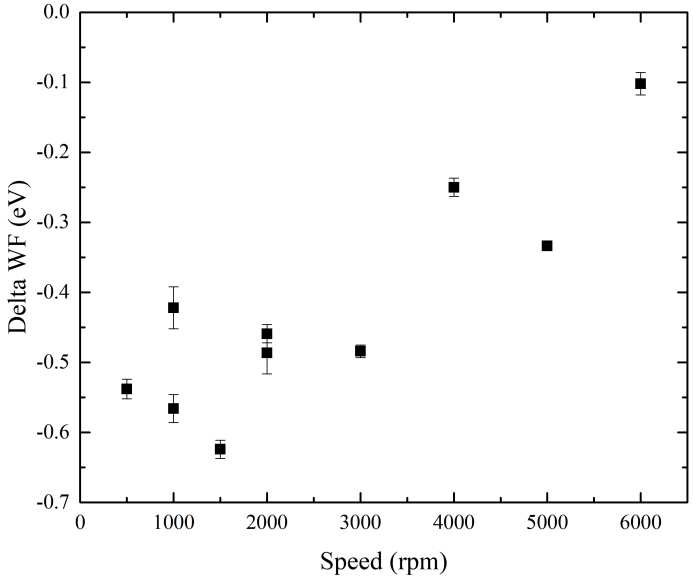

Figure 4.20: Work function changes from spin coating thin films of PEI on copper at varying spin speeds

spin speeds. It can be seen that at very high speeds ($>$ 4000rpm) there is a lower change in work function. This suggests that at thinner PEI films the work function reduction is not as strong. This seems to be at odds with the results in Zhou et al. [143], where even ultra-thin films resulted in large work function changes.

Low spin speeds ($<$ 2000rpm) resulted in films that were patchy and not fully coated. As such 2000rpm is the standard speed used for coated films of PEI as it results in large ΔWF but maintains a visually uniform film. The average ΔWF for speeds less than 2000rpm is -0.52 ± 0.07eV, similar reduction to that found for aluminium [143].

To investigate the air shelf life of the PEI coating a series of KP measurements were taken over a

period of several days. The results are shown in figure 4.21. Here it can be seen that for PEI left in ambient the ΔWF drops rapidly to much smaller values even over a period of a day, whereas the PEI coatings left in a nitrogen flow are relatively stable for about a week with little change in the ΔWF. However eventually all samples return to standard copper WF values. Samples stored in Nitrogen are naturally exposed to air during measurement which could be the primary cause for their decay.

Although this does not take into account the fact that the WF of the bare copper also changes with time. However from figure 4.2 this was found to be negligible in comparison, especially for solvent cleaned copper, therefore the drop in work function must be due to a removal of the PEI from the surface.

As such PEI-coated photocathodes may be stable in a gaseous environment such as that present in ThGEMs, but without measurements of WF under this gaseous environment it is impossible to say for certain as even a small amount of exposure to ambient conditions could effect the reduction caused by the PEI.

Figure 4.22 shows the ΔWF of PEI coated on ZnO films, a spin speed of 2000rpm and solution

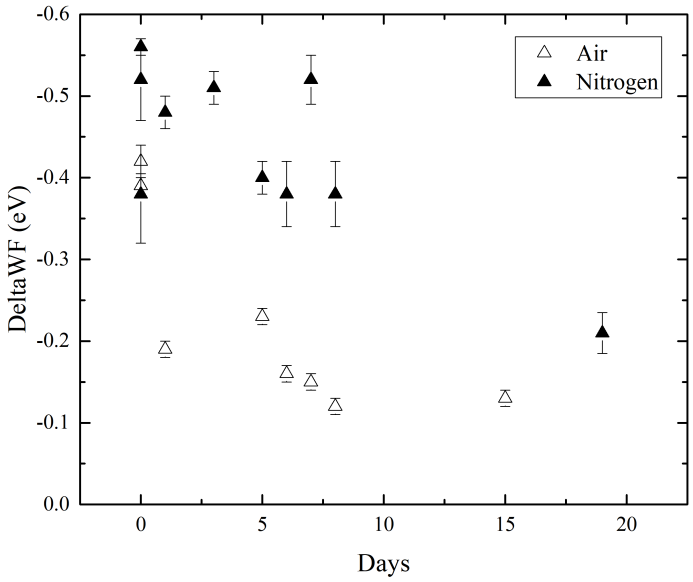

Figure 4.21: KP measurements of PEI coated Cu surface over a period of days

concentration of 0.7% by weight of PEI is used. The figure is plotted as a function of the WF measured for the sample before coating with PEI, it can be seen that samples with higher WF initially show a larger ΔWF than samples that already had a lower WF. However even the largest ΔWF of -0.39 ± 0.04eV is well below the change in WF for ZnO from Zhou et al. [143]

It was found that PEI coated on MgO films appeared to make little difference to the WF only appearing to actually increase it by 0.17 ± 0.06eV on average.

As such it appears that the initial work function of the photocathode effects the amount that the PEI effects the work function. This is most likely due to a decrease in the electronegativity at the surface and the addition of PEI causes less of a dipole at the surface.

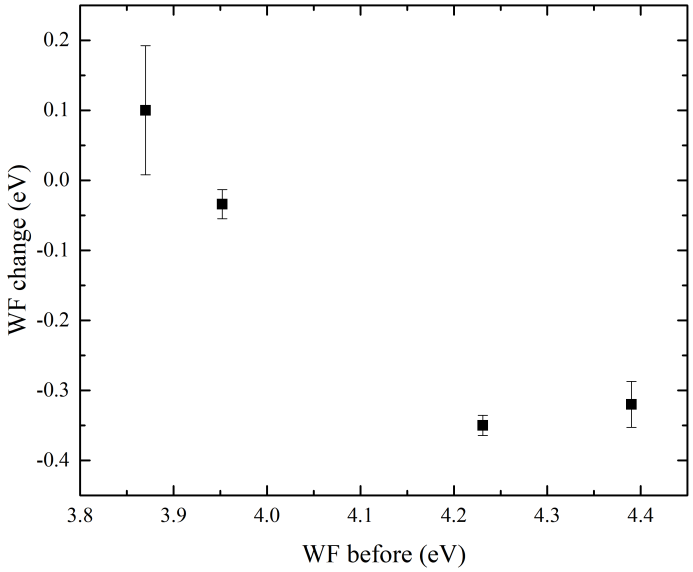

Figure 4.22: ΔWF of ZnO films spin coated with PEI as a function of initial WF

4.6 Summary

The standard deviation in WF measurements across a surface were found to be about 0.03eV which is smaller than the error on the WF on the tip of the KP 0.07eV, meaning we can get more accurate determination of relative changes compared to the actual WF values.

It was found that polishing a copper surface with Brasso instead of the standard solvent cleaning method resulted in a much larger signal under illumination. Despite this, on average, polished copper surfaces showed only slightly lower WF (about 0.08 ± 0.04eV). Also, polishing samples already measured showed little to no change in work function, therefore this is unlikely to be the reason for the increased signal seen under illumination.

From the XPS data, the polished copper surfaces showed a marked reduction in the satellite peaks at 940eV and above, which is attributed to the Cu^{2+} components such as CuO and CuOH. The reduction in this oxide layer was further evidenced by a larger metallic contribution in the LMM Auger spectrum as well. Therefore we can say that polishing samples removes the top oxide layer exposing the metallic layer underneath which causes the increase in signal seen under illumination.

Samples that were cleaned in a solution of Micro-90 and distilled water showed much lower work function of about 4.01 ± 0.11eV. The large change in work function when Micro-90 was used as cleaning solution could be explained by the introduction of a Na 1s region in the XPS spectra. Micro-90 cleaning solution contains 10 to 25% of ethylene diamine tetraacetic acid tetrasodium (EDTA-Na_4) which could explain the introduction of Na to the XPS spectrum. The Na 1s on the surface could cause a surface dipole lowering the work function measured.

Copper shows remarkable stability over time with almost no change in work function over a period of 20 days. There does appear to be a small increase in the WF measured after exposure to ambient air over a couple of days which is more pronounced for the polished samples. This is most likely due to oxidation or addition of water to the surface after being exposed to ambient conditions. After this initial increase in WF, however, the samples showed no change in work function.

For the deposited films of MgO and ZnO it was found that the work function is dependent on the thickness of the overlayer coated on the copper substrate. With thinner layers having work functions somewhere between the saturated overlayer value and the substrate layer.

Table 4.3 shows the average WF measured for MgO and ZnO films grown via PVD under two

Material	Vacuum WF (eV)	Ambient WF (eV)
MgO	3.64 ± 0.04	4.15 ± 0.17
ZnO	4.11 ± 0.06	4.35 ± 0.12

Table 4.3: Average WF for MgO and ZnO under different oxidation methods

different oxidation conditions: letting oxygen leak in during growth under vacuum and letting the sample oxidise naturally in ambient air by opening the chamber straight to air. Both MgO and ZnO show an increase in WF for samples oxidised under ambient conditions compared to samples oxidised under vacuum. MgO shows a much larger change in work function for samples oxidised in ambient compared to samples oxidised under vacuum conditions, which are consistently around a value which is similar to that found for clean polycrystalline magnesium [106].

It was found from the O1s region that the sample oxidised under vacuum conditions had a larger $Mg(OH)_2$ component, whilst the sample allowed to oxidise naturally under ambient conditions had a larger $MgCO_3$ component.

Unlike the standard copper photocathodes, the deposited Mg films were found to actually decrease in work function during exposure to ambient air. From the XPS of samples left in ambient for a long period (6 months) the XPS shows a larger metallic component in the Mg 2p region suggesting a thinner oxide layer. There does not appear to be any relation to the amount of metallic component present to the work function, instead the O 1s region is still the best indicator of work function (with increasing $Mg(OH)_2$ showing lower work function). There is also a much larger MgO component present in the XPS spectra of the sample left in ambient, which could be the reason for the decrease in WF over time.

The average work function for ZnO films oxidised in vacuum is similar to the value for zinc

annealed under vacuum [136], where the average work function for ZnO films oxidised in ambient conditions is more similar to the freshly cleaved ZnO single crystals in Moorman et al. [136]. ZnO films that were deposited using electrochemical deposition were found to have a mean work function of 4.4 ± 0.2 quite similar but a little higher than ZnO films oxidised in air. Almost all the ZnO samples left in ambient conditions all appear to tend to and settle at the slightly higher work function of 4.35 ± 0.11eV, which is closest to the value of ZnO films grown via electrochemical deposition.

It was seen from the LMM spectra for ZnO films that samples oxidised in vacuum showed a much larger metallic component as shown by a much larger peak at 992.85eV and 996.2eV, with a secondary peak at 988.1eV which almost perfectly fits the LMM value for ZnO from Dake et al. [139]. Samples oxidised in ambient showed a small metallic component but much less than samples oxidised in vacuum, also the secondary peak was shifted to a lower K.E. at around 987.1eV, which again fits perfectly the LMM value for hydrazincate from Dake et al. [139]

Further evidence for an increased $Zn(OH)_2$/$ZnCO_3$ or hydrazincite component in ambient oxidised and electrochemically deposited films is shown in the O 1s and Zn2p regions. Whereas, vacuum oxidised samples show largest ZnO component along with a large metallic contribution, ambient oxidised samples show a large $Zn(OH)_2$ but small $ZnCO_3$ and electrochemically deposited samples show almost no ZnO but the largest $ZnCO_3$ and the smallest $ZnCO_3$ contribution. Therefore it can be summarised that the formation of a mixture of $Zn(OH)_2$/$ZnCO_3$ or hydrazincite raises the WF of the film and this will form naturally over time if left out in ambient conditions.

Finally PEI coatings on various photocathodes were investigated in attempt to lower the work function of our photocathodes. It was found that at lower speeds ($<$ 2000rpm) the ΔWF is larger. However at very low speeds the film was visibly patchy so as a standard the speed of 2000rpm was used.

For speeds $<$ 2000rpm the average ΔWF for copper was found to be -0.52 ± 0.07eV.

The reduction in work function was found to decrease with exposure to ambient conditions, with only a day reducing the ΔWF by 0.2eV and eventually going back to the original WF. However, the WF reduction appeared to remain reasonably constant when left in nitrogen. This suggests that although care will have to be taken with depositing and storing the devices, PEI could be used in a gaseous environment to reduce the work function of a photocathode with higher work function such as copper.

It was also found that if ZnO had low work functions (4eV and lower) the ΔWF was very small or negligible, whereas ZnO films with higher WF (4.2 and above) had a ΔWF of -0.39 ± 0.04 on average. MgO films were found to actually increase after being spin coated with PEI with a ΔWF of 0.17 ± 0.06 on average. Therefore it appears as if the ΔWF from coating materials in PEI actually depends on its initial WF. This is likely due to the fact there is already a strong surface dipole on the MgO and ZnO films with low WF, therefore adding PEI does not help with a contribution to the surface dipole.

However this does not match exactly the results found for Zhou et al. [143] as they found the largest work function reduction for Au, which has a higher WF than the other materials tested.

Chapter 5

Photoemission Yield of Metal Oxides

5.1 Introduction

In this section we will investigate the output photocurrent of ThGEMs coated with various photocathodes under illumination with light sources of different wavelength and power. From this data we will look at how the work function measured in the previous section effects the photocurrent measured and therefore the quantum yield of our photocathodes. We will also attempt to use the spectral calibration of the light sources performed in section 2.5 to get relative quantum efficiency values. We will also attempt to get values of direct QY by illumination of the photocathode surface and collection of photoelectrons via a drift field created by a high voltage mesh above the surface.

As mentioned before the photocurrent collected on the electrode is proportional to the product of the quantum yield of the photocathode (QY), electron transfer efficiency (ETE), the multiplication (M) of the ThGEM and the incident flux (ϕ_i). We can get values of incident flux for our light sources via the calibration performed in section 2.5. By dividing the photocurrent by the flux times the charge on an electron, we will get the product of the three values (QY, ETE & M), this is referred to as the relative quantum efficiency (RQE), which is the total collected number of electrons compared to the total electrons ejected from the photocathode surface via the photoelectric effect. Therefore, if we assume that the gain is constant for an identical ThGEM structure (hole diameter, pitch, etc.) and identical gas properties (pressure, temperature, mixture, etc.) we can derive a relative quantum yield from the value of RQE.

The assumption that the gain is constant for ThGEMs of the same structural properties is not entirely true as it has been shown in Chapter 3 that the gain stability appears to vary quite a lot between samples. All photocurrent measurements in this section were allowed time for the signal to plateau and then the resultant value of the photocurrent was measured. Also as the data taken was for samples that had not been illuminated before, the issue found with electrodes retaining charge is also not thought to be present.

The photocurrent in this section is measured using the standard chamber setup as described in section 2.4. The ThGEMs used unless stated otherwise have a standard structure of 1.6mm thick

PCB, 15x15mm design with 1.2mm etched holes, with 2.5mm pitch as shown in figure 3.1 with 1mm diameter holes mechanically drilled into the surface. The fabrication process is the same as described in section 3.2.

5.2 Copper

The first photocathode material we will investigate is the basic copper surface on the PCB which ThGEMs are fabricated from.

To achieve a RQE value as a function of wavelength, a tuneable UV laser from the Transient Electronic Absorption Spectroscopy (TEAS) equipment from the Warwick Centre for Ultrafast Spectroscopy was used. The power of the laser was simultaneously measured during the experiment. As the data obtained is already normalised to the incident power on the ThGEM we can easily get a value for the relative QE for the wavelength used by dividing through by the energy of the photons at each point and the charge of an electron, the data for both solvent and Brasso cleaned copper ThGEMs are shown in figure 5.1.

From the figure we can see that the polished copper surface has a much higher RQE at lower

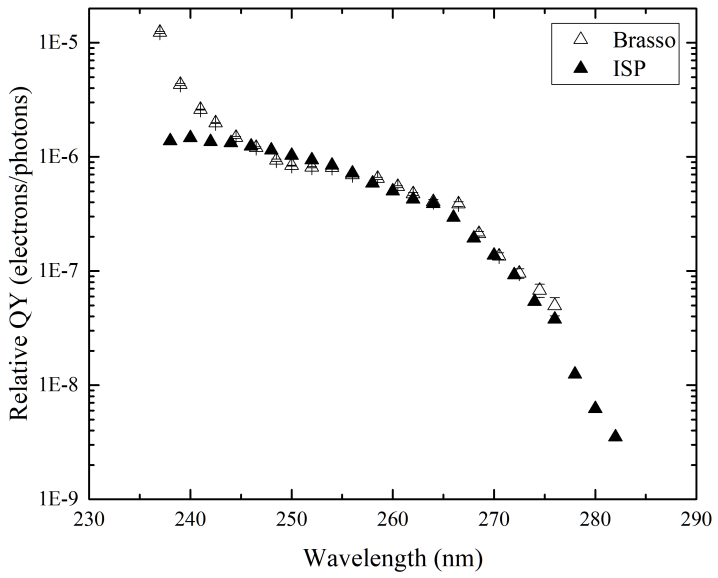

Figure 5.1: Calculated RQE from TEAS data for both solvent and Brasso cleaned copper. The solvent cleaned ThGEM was held at 0.6kV, where the Brasso cleaned copper surface was held at 1kV

wavelengths ($<$ 245nm) which could explain the large increase in signal when illuminated by the deuterium lamp which has its peak wavelength at around 205nm.

It is perhaps surprising that the data for the Brasso ThGEM is not larger due to the fact that the bias is higher so the gain should also be larger. This could be due to the fact that the Brasso sample had been exposed to ambient air for a couple of days before measurement where the copper sample was placed in the chamber almost immediately after cleaning. It could also be due to instabilities of gain in the timescales during measurement.

Figure 5.2 shows the photocurrent measured for standard 1.6mm thick PCB ThGEMs under

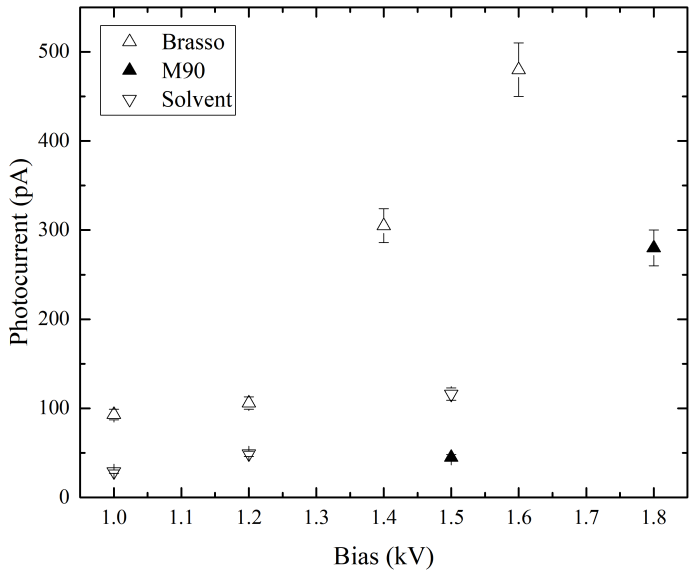

Figure 5.2: Photocurrent measured for standard 1.6mm thick PCB ThGEMs under different cleaning conditions under illumination from deuterium lamp

different cleaning conditions: solvent cleaned, mechanically polished with Brasso and ultrasonic cleaning with a solution on Micro-90. From this figure it can be seen that despite the much lower work function of copper photocathodes cleaned in a solution of Micro-90, it does not lead to a much higher QY, rather instead, it appears to have a lower signal than ThGEMs with polished copper photocathodes which have similar work function to the solvent cleaned copper surfaces. This suggests that the QY depends on much more than simply the work function of a material.

Figure 5.3 shows the experimentally measured values for QY for clean copper surface under vacuum, for the wavelengths of interest as measured by Krolikowski et al. [2]. Although our values for QE are going to be different, as these measurements were performed in vacuum and do not take into account backscattering in gas, we can use the general shape of this graph to estimate the contribution to the overall signal from the different wavelengths. Unfortunately the measurements are only up to around 260nm, but the deuterium lamp has a continuous emission from 160nm to 400nm, although wavelengths higher than the work function of copper should not have any effect.

To estimate the contribution at wavelengths lower than 260nm we have fitted a basic power

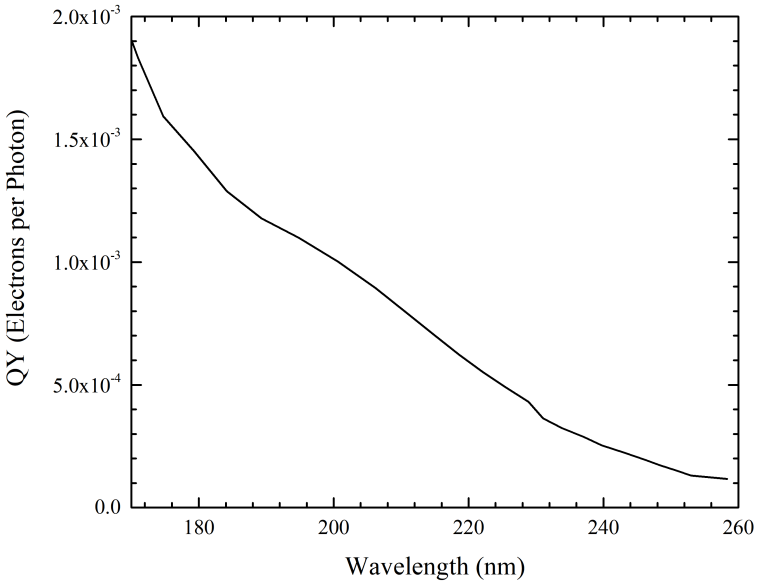

Figure 5.3: Experimentally measured values of QY from Krolikowski et al. [2] for clean copper surface under vacuum

function as shown,

$$y = (a + bx)^{1/c} \tag{5.1}$$

This function was chosen as it appeared to fit the experimental data reasonably well and gave a cutoff at around 300nm which would be expected for the work function of copper.
Figure 5.4 shows the fitted function compared to the experimental data from Krolikowski et al. [2] for the wavelength range of interest.
The incident flux is measured by taking the spectral irradiance calculated in section 2.5 and then using the inverse square law to work out the values at distance of interest and then multiplying by the area and dividing through by the photon energy at each point.
By multiplying the incident flux by the QY values from Krolikowski [2] et al. and multiplying by the charge of an electron we can calculate the current expected with these QY values. However it is clear that this gives us much larger values than what is measured. However by normalising the curve to the photocurrent measured under illumination we can achieve values of RQE using the shape of the QY curve from Krolikowski et al. [2]
Table 5.1 shows the calculated RQE values at 210nm (the peak wavelength of the deuterium lamp) for copper samples cleaned under 3 different condtions: polished with Brasso, ultrasonic bath in solvent mix and ultrasonic bath in M90/distilled water solution. Here we can see that Brasso has much larger RQE than solvent or M90 cleaned solutions with the RQE being 2.8 ± 0.3 times larger than solvent cleaned samples at the same HV bias and8 ± 2 times larger than sam-

ples cleaned in M90 solution.

To compare the RQE measured using this method compared to that found by illumination of

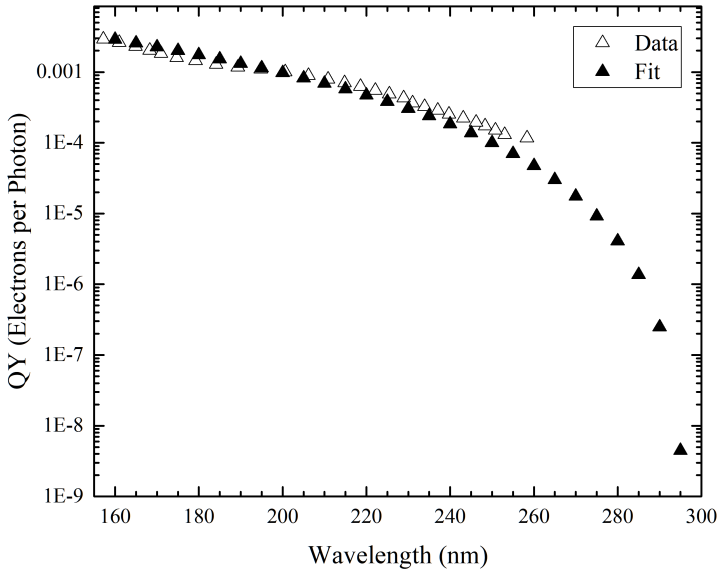

Figure 5.4: Comparison between power fit and experimental data from Krolikowski et al. [2]

Sample	Bias (kV)	RQE (10^{-6}e$^-/\gamma$)	Error (10^{-6}e$^-/\gamma$)
Brasso	1.5	8	1
	1.2	2.1	0.4
	1	1.85	0.3
Solvent	1.5	2.3	0.4
	1.2	0.98	0.16
	1	0.58	0.1
M90	1.8	5.6	1
	1.5	0.9	0.16

Table 5.1: Calculated RQE values for standard ThGEMs under illumination of deuterium lamp for different cleaning methods

the TEAS laser, the calculated RQE for Brasso and ISP at 1kV bias are shown with the corresponding TEAS data in figure 5.5*a* and 5.5*b*.

From figures 5.5*a* and 5.5*b* we can see that the shape of the RQE as a function of wavelength is different for the values obtained from the TEAS laser and those calculated from the response from deuterium lamp. The most likely reason for this difference would be the fact that the QY values from Krolikowski et al. [2] are not indicative of our copper surfaces as they are for clean copper under vacuum conditions.

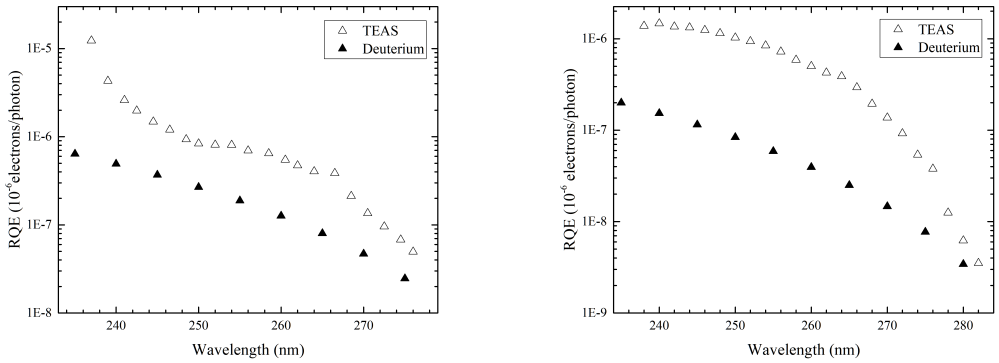

(a) (b)

Figure 5.5: RQE comparison between those calculated from deuterium lamp and from the TEAS laser for a) Brasso and b) solvent cleaned copper surfaces

5.3 Metal Oxide Films

As in the case for the copper surfaces we will first investigate the RQE as a function of incident wavelength by using the tuneable TEAS laser for the thin metal oxide films grown in UHV. Figure 5.6 shows the RQE calculated for ZnO and MgO films with the previous data for solvent

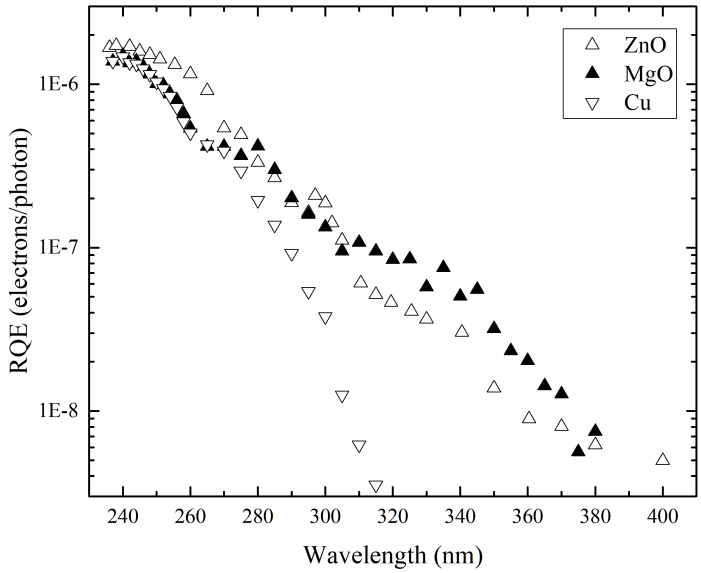

Figure 5.6: RQE values calculated for solvent cleaned copper, MgO and ZnO films under illumination using TEAS laser

cleaned copper using the tuneable TEAS laser.

The solvent and MgO film were placed under 0.6kV bias where the ZnO film was at a 0.5kV bias. First thing of note is that the ZnO film gave the best signal overall which could be due to level of air contamination each film has been exposed to. The MgO and ZnO film showed similar signal values for wavelengths longer than 280nm, however no signal was detected at wavelengths longer than 360nm (3.44eV) for the ZnO film.
Both ZnO and MgO films show a signal well beyond their KP measured work function. Although the reason for this is not known, it is assumed that due to the high power density of the beam there may be a 2 photon effect adding to the signal.

5.3.1 Magnesium Oxide Films

In this section we will investigate how the WF, chemical structure and growth conditions, from section 4.3, effect the signal received from MgO films, as well as calculate RQE values for a variety of light sources.
Figure 5.7, shows the photocurrent measured under illumination from the deuterium lamp for

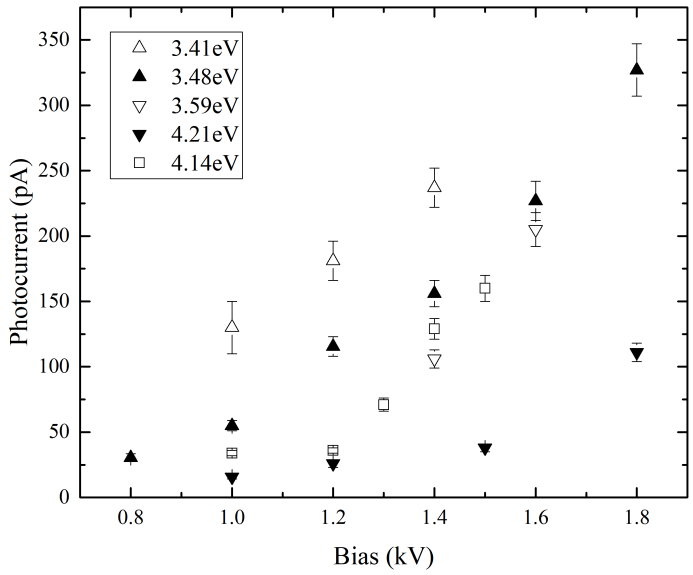

Figure 5.7: Photocurrent received under illumination of deutrium lamp at a distance of 95mm for several Mg films.

a variety of films deposited via PVD as a function of work function. Although there is not a huge change in response the samples with more negative CPD (lower work function) do appear to produce slightly higher photocurrents, as shown in figure 5.8, which shows the response as a function of work function for 1kV and 1.2kV. Smaller HV biases were used as the shape of the curves are different meaning the gain is not consistent at a particular HV bias, most likely due

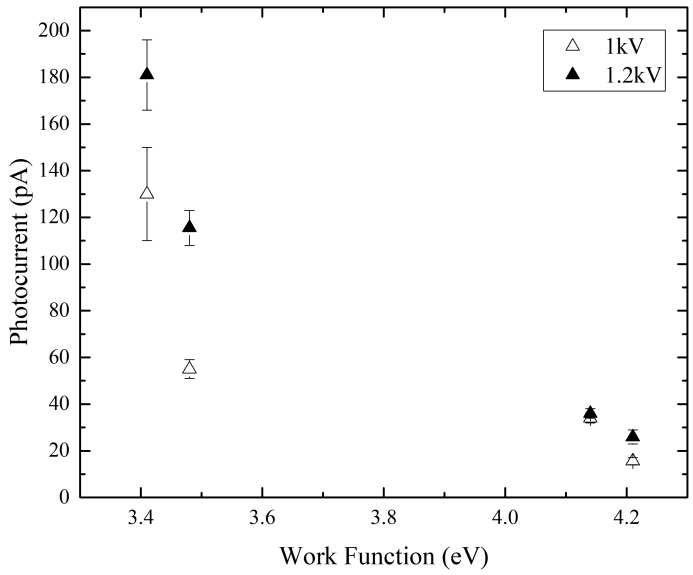

Figure 5.8: Response under illumination of the deuterium lamp as function of work function. Legend shows the HV bias.

to the rising behaviour mentioned in chapter 3 which is exacerbated at higher voltage biases.

Figure 5.9, shows the QY of a magnesium disk under vacuum, for photons with wavelengths

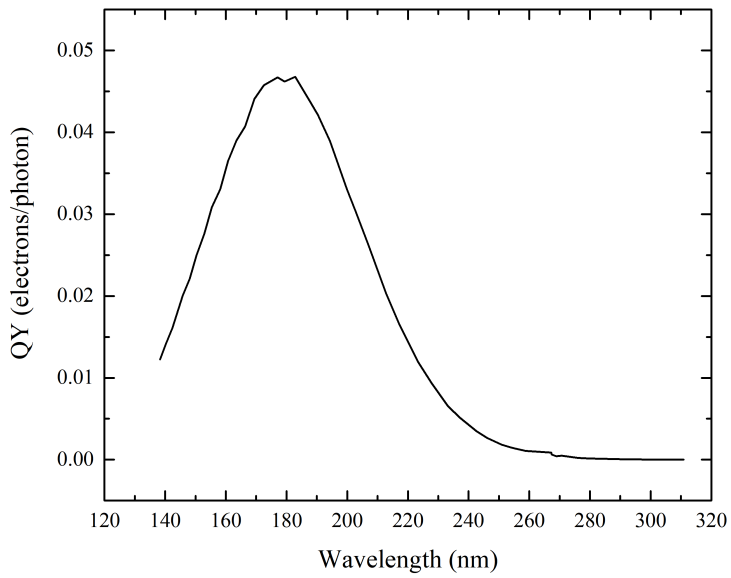

Figure 5.9: QY for Magnesium disk in vacuum as measured by Palmer et al. [3]

from 138nm to 310nm, taken from Palmer et al. [3]. As in the case of the copper photocathode it is expected that the values from this figure will be significantly higher than our values as they are for clean pure magnesium metal instead of native MgO under ambient conditions. However it could be possible to use the shape of this data to get the contribution from the different wavelengths using the deuterium measurements from figure 5.7 and the irradiance from the deuterium lamp.

Much like in the case of copper ThGEMs we will calculate the RQE values under illumination of the deuterium lamp using the measured QY from Palmer et al. [3] as a basis for the contribution at each wavelength. Table 5.2 shows the RQE calculated using this method for the MgO films from figure 5.7.

Figure 5.10, shows the data both from measurement under TEAS laser and the RQE values

Work function (eV)	Bias (kV)	RQE ($10^{-6}e^{-}/\gamma$)	Error ($10^{-6}e^{-}/\gamma$)
3.41	1.4	8.5	2
	1.2	7	1
	1	5	1
4.21	1.5	1.4	0.3
	1.2	0.95	0.2
	1	0.57	0.12
4.14	1.5	6	1
	1.2	1.3	0.3
	1	1.2	0.3

Table 5.2: Calculated RQE for illumination under the deuterium lamp for MgO films

calculated using the deuterium lamp. The data matches reasonably well however the TEAS data is under a HV bias of 0.6kV where the deuterium data shown is for a bias of 1kV, despite this the TEAS data still has a slightly higher RQE. Either we have overestimated the photon flux from the deuterium lamp or the TEAS laser shows an improvement in signal due to the 2 photon effect which we used to explain the response found at wavelengths much longer than the work function of the material.

Table 5.3 shows the response and RQE value calculated for MgO film with a WF of 4.21 ± 0.11eV using the pond lamp. The spectrum of this particular light source, shown in section 2.5, is primarily at a narrow peak at 253.7nm. Using the power measurements of 1.45E-4W for the Thorlabs sensor at 50mm gives a flux of about 9.8E13 photons/s at 75mm.

The RQE value at 1kV is very similar to the value for the deuterium lamp at 210nm, however according to Palmer et al. [3] the QY at 210nm should be about 15 times higher than the Thorlabs power meter cannot be trusted as the calibration of the QY at 253.7nm. This gives further evidence that the power measurements from the Thorlabs power meter is most likely wrong.

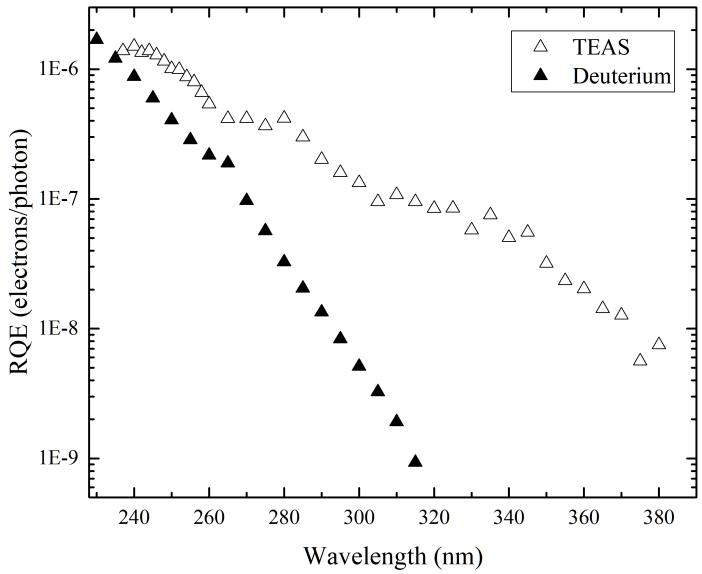

Figure 5.10: Comparison between TEAS laser and Deuterium lamp calculated RQE values for MgO film

Bias (kV)	Photocurrent (pA)	Error (pA)	RQE ($10^{-6}e^{-}/\gamma$)	Error ($10^{-6}e^{-}/\gamma$)
1.2	35	2	2.23	0.11
1	21	1.3	1.34	0.07

Table 5.3: Photocurrent measurements and estimated relative quantum efficiencies for magnesium film under illumination of pond cleaning lamp

5.3.2 Zinc Oxide Films

The response of different ZnO coated films under illumination of the deuterium lamp is shown in figure 5.11*a* for films of varying workfunction as a function of HV bias applied. The response is also plotted as a function of workfunction for two different HV biases in figure 5.11*b*. Just as in the case for MgO films we can see that the curves as a function of HV bias from figure 5.11*a* have varying shapes which suggests that the gain is again not constant with HV bias, as mentioned before this is attributed to rising gain behaviour discussed in chapter 3. However from figure 5.11*b*, we can see there is a general trend of larger photocurrent with decreasing WF in the same way as MgO despite some fluctuations for samples with similar WF which is most likely due to changes in the gain of the detector.

Figure 5.12 shows the response of electrochemical deposited zinc under illumination of the deuterium lamp. As in the case of PVD samples the lower WF sample has a higher photocurrent signal. However the difference in this case is much more noticeable, with the sample with WF of 4.25eV having photocurrent values similar to the PVD sample with WF of 3.72eV. This appears

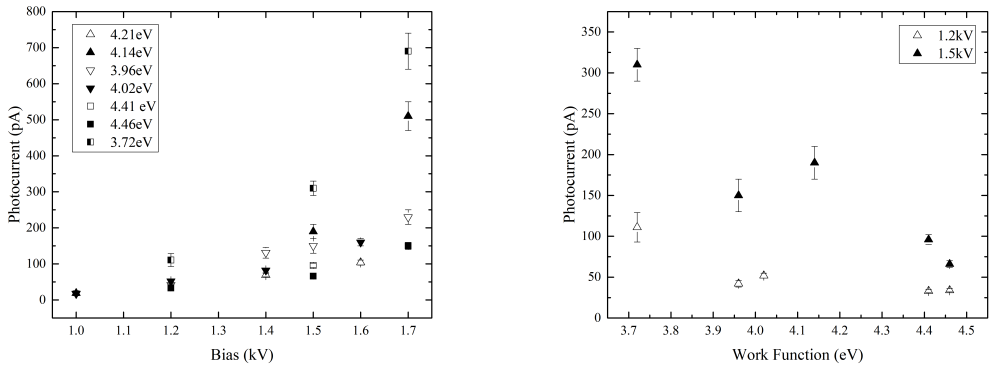

(a) (b)

Figure 5.11: Photocurrent measured for ZnO films under illumination of the deuterium lamp. a) Photocurrent as function of HV bias, legend shows WF measured b) Photocurrent as function of WF measured, legend shows HV bias

to go against the trend that lower WF gives a higher signal. It is also not likely to be due to a rising signal as both samples are given the same time for the signal to settle, therefore it is likely something about the chemical composition of the electrochemical deposited samples results in a higher signal.

Figure 5.13 shows the QY measured by Mosteller et al. [145] for cleaved crystals of Zn in UHV.

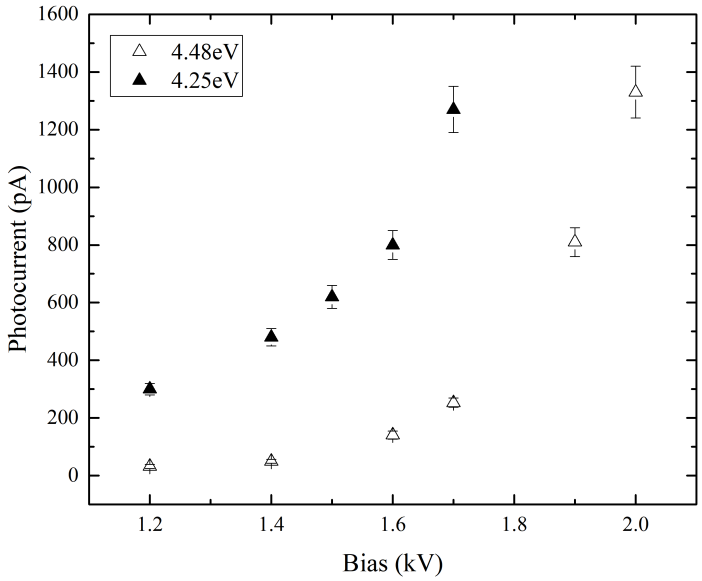

Figure 5.12: Photocurrent received under illumination of deuterium lamp for several Zn films electrochemically deposited

These values are expected to be higher than the values we find for ZnO films in ambient, but as before we will use the general shape. A simple allometric fit ($y = ax^{-b}$) was used to achieve values for longer wavelengths that were not measured (> 160nm).

Using the shape of the QY from figure 5.13 the RQE for illumination under the deuterium

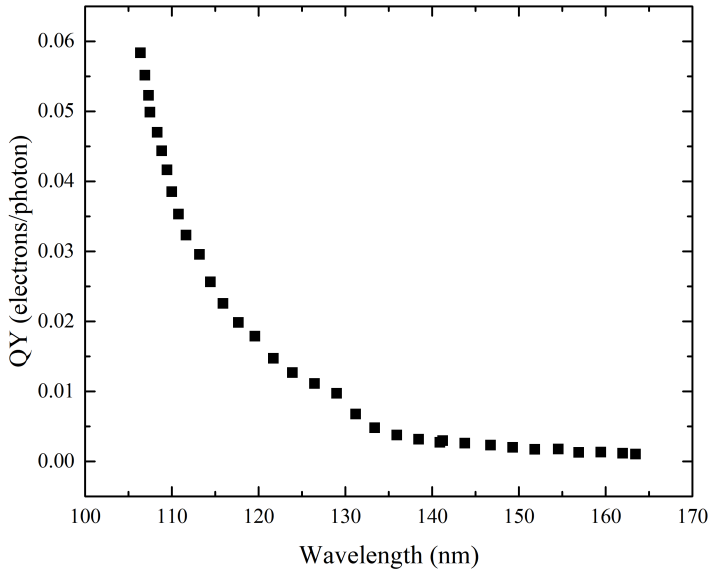

Figure 5.13: QY of cleaved Zn single crystals in UHV as measured by Mosteller et al. [145]

lamp is calculated for ZnO films with varying wavelengths. Table 5.4 shows the calculated RQE values at 210nm for PVD films and table 5.5 shows the calculated RQE at 210nm for electrochemically deposited films.

Figure 5.14 shows the RQE values calculated under illumination of deuterium lamp compared to the data taken using the TEAS laser for two ZnO films with similar WF. It can be seen that the RQE values are much higher, this is especially unexpected as the deuterium lamp measurements are performed at 1kV instead of 0.5kV for the TEAS measurements. Large errors are incurred from rising behaviour of the signal so it is unclear if this is the main reason for this difference.

The calculated RQE using the 250J LED has also been done for a new ZnO film oxidised in vacuum, with a work function of 3.91 ± 0.07, is $0.48 \pm 0.03 \times 10^{-6}$ at a HV bias of 1.2kV at 250nm. From the data from figure 5.13 the QY at 210nm should be about 6 times larger than the QY at 250nm. If we look at the RQE for a fresh ZnO film calculated using deuterium lamp with work function 3.72eV it gave a RQE of $(7 \pm 2) \times 10-8$electrons/photon at 250nm which is much lower.

Work function (eV)	Bias (kV)	RQE ($10^{-6}e^{-}/\gamma$)	Error ($10^{-6}e^{-}/\gamma$)
3.72	1.7	7.5	2
	1.5	3.5	1
	1.2	1.2	0.3
3.96	1.7	2.5	0.6
	1.5	1.6	0.4
	1.2	0.45	0.1
4.46	1.7	19	4
	1.5	8	2
	1.2	3	0.7

Table 5.4: Caclulated RQE values for PVD ZnO under illumination of the deuterium lamp

Work function (eV)	Bias (kV)	RQE ($10^{-6}e^{-}/\gamma$)	Error ($10^{-6}e^{-}/\gamma$)
4.48	1.7	2.7	0.5
	1.2	0.35	0.1
4.25	1.7	14	3
	1.5	7	2
	1.2	3.5	1

Table 5.5: Calculated RQE for electrochemically deposited films under illumination of the deuterium lamp

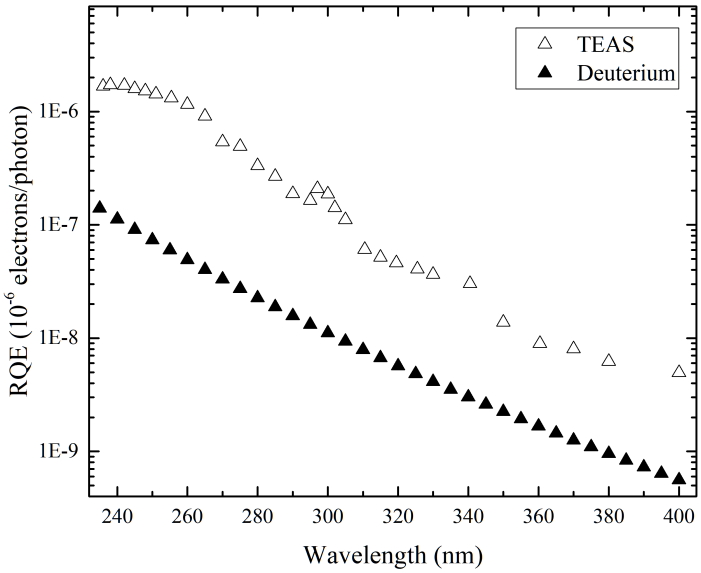

Figure 5.14: Comparison between calculated RQE values from illumination under deuterium lamp and TEAS laser for two ZnO films with similar WF

5.4 Direct Quantum Yield Measurements

5.4.1 Introduction

Whilst we have obtained values of RQE from the photocurrent measurements of deposited films, due to gain stability issues and errors in incident photon flux, it is difficult to get actual values of

QY from these measurements. To measure the photoelectric quantum yield directly the amount of flux at the sample needs to be known and direct collection of the photoelectrons needs to occur via a drift field and collection anode. These measurements are normally performed under vacuum [146] but this will give different values of QY in air or other gases as it does not take into account any interaction or scattering that the photoelectrons would have with the surrounding gas.

5.4.2 Experimental Setup

To measure the direct QY from the photocathode surface a new table is constructed which consists of a mesh suspended above the sample surface to be measured and a single connection on the top surface of the ThGEM leading to the same amplifier used in the photocurrent measurements. A positive HV bias is placed across the mesh to create a drift field. Therefore, when electrons are liberated from the surface of the photocathode they will drift towards the mesh and the induced current will be read out through the amp. In this setup the multiplication stage of the ThGEM is not used so the photocurrent measured is entirely from emission from the photocathode. By simply dividing the received signal by the incident flux and the charge on an electron, we will be able to calculate values for the QY of the photocathode surfaces.

5.4.3 Results

Figure 5.15 shows the photocurrent measured for illumination of a MgO film with Xenon photoionisation discharge (PID) lamp. This lamp is uncalibrated so cannot give us actual values of QY but has a very intense, high energy (9.6eV) photon emission. Using this lamp we can achieve large signals without the need of the multiplication stage normally used in our detectors. The chamber was sealed at atmospheric argon.

The signal as a function of bias as shown in figure 5.15 appears to have two distinct curve shapes: an initial levelling off of the signal which then exponentially rises with increasing bias. It is hypothesised that this initial levelling off of the signal is heading towards all the electrons emitted from the ThGEM surface and after a certain voltage the gain from high electric field around the wires that comprise the mesh start to take effect. Although it is hard to distinguish these two effects from each other, we can get very rough values of QY if we take the value of the stationary point as where the total signal from the photocathode is collected. However, we cannot use the values that we got for the collected charge under illumination of different light sources as accurate values of QY.

However, we will use the deuterium lamp with this new setup to give relative QY to compare to the RQE values calculated in the previous sections. Measurements were taken in low pressure argon by simultaneously letting argon flow through the chamber and pump the chamber with

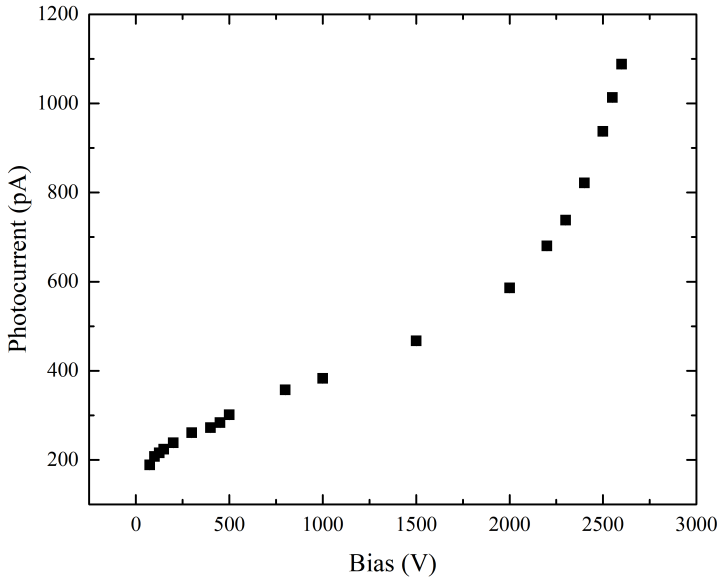

Figure 5.15: Measured photocurrent for MgO film under illumination of Xe PID lamp as function of HV bias across the mesh

a rotary pump. The signal had a S-shape like in figure 5.15 but appeared to settle at 150V so we take this bias as the maximum collection of the photoelectrons with minimum gain from the mesh. The QY values calculated at 150V for 210nm are shown in table 5.6.
However the QY values from this table are basically the same as the RQE values calculated in the previous sections but the RQE values include the gain of the detectors which should be noticeable at 1.2kV. Therefore, there is obviously some gain mechanism even at these voltages as such we cannot use the measured QY values from this method.

Material	QY (10^{-6}e$^-/\gamma$)	Error (10^{-6}e$^-/\gamma$)
Copper (polished)	4	0.05
CuO	0.309	0.006
ZnO (4eV)	8.7	1.2

Table 5.6: Calculated QY values for illumination under deuterium lamp in low pressure argon

5.5 Summary

From the response as a function of wavelength using the TEAS laser, we have found that polished copper surfaces have drastically higher RQE at lower wavelengths ($>$ 245nm). This suggests that the shape of the QY curve measured by Krolikowski et al. [2] may be different depending on the

chemical composition of the copper. As the measurements were performed for clean metallic copper instead of the native oxide of copper. As shown by the XPS data from section 4.2.2 only copper surfaces polished with Brasso show a metallic component in the surface.
Also from the TEAS data all photocathodes showed signal for longer wavelengths than would be expected from the work function of the various photocathodes and the signal was much larger than using the deuterium lamp. We have attributed both of these effects to a possible two photon contribution to the signal due to the high power density of the TEAS laser.
RQE values (i.e. Gain and QY) have been calculated using the shape of the QY measured by Krolikowski et al. [2] for illumination under deuterium lamp. Comparing the shape of these calculated RQE values to the calculated RQE from the TEAS data we can see a large difference in the shape of the RQE as a function of wavelength. This suggests that the shape of QY from Krolikowski et al. [2] does not match our materials QY.
Table 5.7 shows the calculated RQE values for copper, MgO and ZnO using the deuterium lamp and QY curves found from literature [2, 3, 145]. From this table it can be seen that both MgO and ZnO have a wide range in their calculated RQE values and thus the signal measured. However there does seem to be a trend in the work function with low work functions producing higher signals in general so on average MgO gives higher RQE values but in some cases the ZnO films can have superior RQE. In particular the electrochemically deposited ZnO has much higher signal although the reason for this is not known.
In attempt to directly measure the QY of photocathodes, we used a mesh to collect the electrons

material	RQE ($10^{-6}e^{-}/\gamma$)	Error ($10^{-6}e^{-}/\gamma$)
Cu (polished)	3.7	0.4
CuO	1.7	0.2
MgO (3.41eV)	7	1
MgO (4.14eV)	1.3	0.3
ZnO, EC (4.25)	3.5	1
ZnO (3.72eV)	1.2	0.3
ZnO (4.46eV)	3	0.7

Table 5.7: RQE values calculated for copper, MgO and ZnO under illumination of the deuterium lamp at a HV bias of 1.2kV

directly emitted from the photocathode surface. For the measurements in argon after a certain voltage bias (V) show an exponential rise in the photocurrent measured which must be due to some multiplication due to the high electric field around the wires. This limits the accuracy of the measurements of QY as it is difficult to tell where the signal from collection of electrons emitted from the photocathode ends and the signal from multiplication around the wires start. Therefore we could not use this method to measure the QY of our photocathodes.

Chapter 6

Potential Applications

6.1 Introduction

GPMs based on GEM elements have already found success in Cherenkov and other HEP experiments [147, 148]. In RICH detectors in particular, the use of cascaded GEM elements coupled with bialkali photocathodes allowed the first demonstration of DC-operated visible-sensitive GPMs with single photon detection efficiency.
GPMs have also been used in liquid noble gases for rare-event experiments and fast-neutron and gamma-ray imaging [149, 150] and has found potential interest in other applications such as: Spark, flame and dangerous gas detection [151] and biomedical applications [152].
In this chapter we will look at some novel applications of GPMs, as well as some reflection and absorbance measurements from different materials.

6.2 NLOS communications

6.2.1 Introduction

UV communication was first proposed by Harvey et al. [153] and has had noticeable attention over the past decade. Current research into this field, focuses mostly on improving the range and data rate of NLOS UV communication. Sun et al. [154] have achieved a data rate of almost 1Mbps at a distance of 150m using a UV LED array of 50mW luminous power at 266nm and Wang et al. [155] showed that it is possible to extend the transmission range to over 1km. Also the possibility of under-water NLOS communication has been investigated by Sun et al. [156] at slighter longer wavelengths (375nm).
Many benefits exist of using UVC light for NLOS communications: more effective scattering in the atmosphere than visible or infra-red meaning accurate positioning of emitter and receiver is not required and very low levels of background, due to ozone absorption of UVC in the stratosphere.

NLOS is also of interest for military applications, due to its inherent secrecy, as UVC attenuates quickly over large distances due to its relatively high levels of molecular absorption even at low altitudes [157].
The characteristics of UV propagation through atmosphere leads naturally to a wide field of view (FOV) solar-blind receiver, as the maximum amount of light can be received without the usual penalty of an increase in the overall background level. This is where a ThGEM-based GPM device could potentially be very useful due to its properties such as: cost-effective large areas, large acceptance angle coupled with high gain, stability and capability of being solar-blind via proper coating of a photocathode.
Currently detectors such as multiple photomultiplier tubes are used as receivers as in the case of Wang et al. [155], although PMTs have very high gain they are expensive when covering large areas as multiple PMTs are needed.

6.2.2 Experimental Results

The largest signal achieved for our ThGEMs was for a Cu photocathode polished with Brasso, ThGEM with 0.6mm hole diameter, 0.1mm etched rim and 0.8mm multiplication gap. This ThGEM gave a total photocurrent of 763 ± 4pA at 0.9kV bias under illumination of deuterium lamp at a distance of 95mm.
Using the spectral irradiance for the deuterium lamp from section 2.5, we calculate the photon flux at 95mm to be $(2.08 \pm 0.01) \times 10^{14}$ photons/s. Therefore the normalised response at this HV bias is $3.7 \pm 1.2 \times 10^{-12}$pA/photon/s. The average noise of the measurements after being filtered using a lowpass filter is about 0.2pA. Therefore the minimum incident photon flux needed for a signal to noise ratio of > 1 is $(5.4 \pm 1.3) \times 10^{10}$ photon/s.
Using a simple inverse square law, at 1km distance as done in Wang et al. [155] the deuterium lamp would have a photon flux of 2.23 ± 0.01E10photons/s/m^2 meaning a detector of active surface area of $2.4 \pm 0.6 m^2$ would be required to get a measurable signal with direct line of sight. This is obviously a large detector area especially as the actual signal would be lower as it would not be in line of sight. However, by using a more powerful light source or cascading ThGEMs it should be possible to achieve much higher signals.
Chen et al. [158] developed a path loss model built on extensive field test results up to a distance between transmitter and receiver of 100m. It was found that the power loss (P_t/P_r) was proportional to r^{α} where alpha is a function of the apex angle, approaching unity for transmitter and receiver apex angles of 90° and for apex angles at 30° or 45° gave α in the range of 1.4 to 1.7.
Figure 6.1*a* & 6.1*b* show the response of a standard polished Cu ThGEM as a function of detector angle with respect to the normal incident to the UV light source for a distance of 90mm and 220mm respectively. Figure 6.1*a* shows almost linear decrease in signal with increasing detector angle in degrees from the light source normal.
Table 6.1 shows the calculated α where $S_{90mm} \times (90mm/220mm)^{\alpha} = S_{220mm}$. From this graph

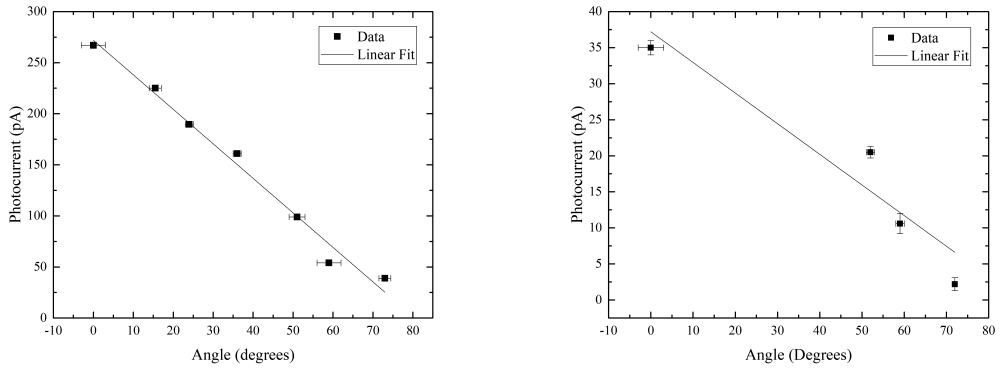

(a) (b)

Figure 6.1: Photocurrent measurements under illumination under deuterium lamp as a function of angle for at a distance a)90mm and b)220mm. ThGEM used was the standard 1mm diameter hole, Brasso polished ThGEM operated at a bias of 1.5kV for both distances

it can be seen that for a receiver angle of 50 to 60 degrees with respect to the optical axis and the transmitter angle the reduction in signal is less than if it was directly emitted, also at 72 degrees the signal is a lot lower probably due to the fact that the transmitter solid angle and receiver solid angle no longer intersect, however the fact there is still some signal shows that there must be some scattering in the air despite both the low power of the UV light source and the small distances used.

Reciever angle (degrees)	α	Error
0	2.27	0.14
52	1.66	0.11
59	1.71	0.16
72	3	0.3

Table 6.1: Calculation of the extinction power law as function of receiver angle

We have not changed the transmitter angle to see how this effects the signal. Also due to it facing along the optical axis, some of the emitted cone will connect with the ground after some distance and therefore it would be better to repeat measurements for a larger transmitter angle. The deuterium lamp that we use in the lab does not have enough power to measure the scattering in the atmosphere. So although there is a proof of concept we have not investigated its proper capability as a detector for NLOS communication. We either need a more powerful UV light source or increase the gain from our detector to further investigate the capability of GPMs as a possible detector for NLOS communication devices.

6.3 Water Monitoring

6.3.1 Introduction

Chemical measurements have historically been the popular way for water contamination monitoring. The laboratory standard is the dichromate method where the amount of oxygen needed for oxidation of all organic substances in water, known as the chemical oxygen demand (COD), is determined using the digestion of chromic acid of organic matter. However this method needed 2 hours for oxidation and used hazardous chemicals making it unsuitable for in-line water contamination measurements [159].
UV spectroscopic measurements are of particular interest in real-time monitoring of contaminations or pollutants in water and both florescence and absorption techniques have been used to detect organic matter and other contaminants in a variety of different water conditions [12, 160]. Due to the fact that many hydrocarbons absorb strongly in the UV, the high optical transparency of UVC in water and lack of contamination of any chemical reagents, there has been a substantial shift to these optical devices for in-line water monitoring.
In particular benzene rings have a large absorption cross section at about 253nm (2.19E-18cm^2) [161]. Historically UV absorbance at 253.7nm has been used to evaluate the total organic carbon (TOC) content in water, due to it corresponding to the sharp spectral line of low-pressure mercury lamps, strong absorption from hydrocarbons and lack of absorption from other soluble products such as inorganic salts.
Optical methods have also been used to detect the different types of chemicals present as well as the total organic carbon (TOC) content. For example, Vogt et al. [162] developed a UV spectroscopic method able of distinguishing between five different benzene derivatives. Accurate concentrations of species in mixtures of various chemicals was achieved by Ultraviolet Dynamic Derivative Spectroscopy (DDS) that generates optically an approximation of the first and second derivative of the transmission spectra with respect to wavelength. These derivatives are used for evaluation in order to enhance spectral features. To generate the derivatives of the absorbance with respect to wavelength, the emitted wavelength selected by a monochromater is varied sinusoidally.
In this section we investigate the amount of absorption at different wavelengths for a selection of water solutions with various contaminants to investigate the ability of ThGEMs as the detector element in a water monitoring device.

6.3.2 Experimental Setup

The standard ThGEM housing as described in section 2.4 is used to house the ThGEM detector element and a metal cuvette holder is fitted onto the front of the chamber as shown in figure 6.2*a* and 6.2*b*. This cuvette holder has a cut out in the shape of the quartz cuvettes used so they can slot in and the cuvette holder simply slots over the top of the front section of the ThGEM

chamber. This means the UV light will pass through the cuvette before illuminating the detector surface. The absorption can then be measured via comparison to the light that passes through the empty cuvette.

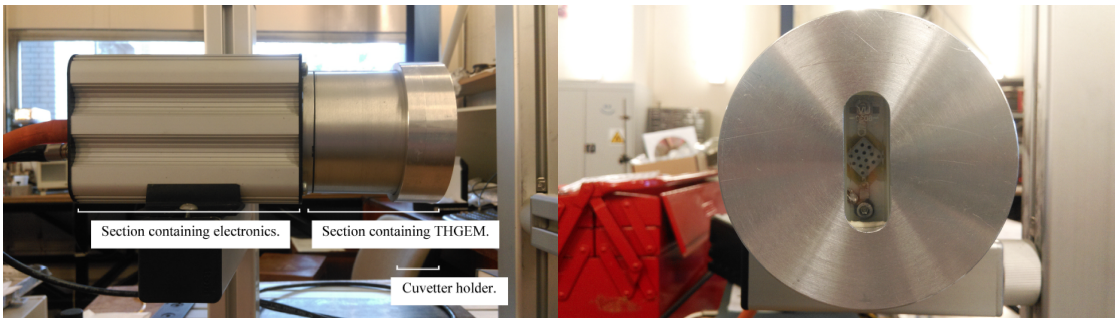

(a) (b)

Figure 6.2: Photo of ThGEM chamber and cuvette holder, a) side view b) front view.

6.3.3 Results

Table 6.2 shows the absorption of different water samples taken from lakes across the campus at University of Warwick and distilled water as a reference, under illumination from the deuterium lamp. Table 6.3 shows the absorption for these samples under illumination from the 250nm LED.

The lake sample #2 was much dirtier with visible sediment in the sample retrieved, this is shown

Sample	Absorption (%)	Error (%)
Lake Sample #1	36.5	0.4
Lake Sample #2	86.9	0.4

Table 6.2: UV absorption measured for different water samples under illumination of deuterium lamp

Sample	Absorption (%)	Error (%)
Lake Sample #1	33.9	0.5
Lake Sample #2	80.8	1

Table 6.3: UV absorption measured for different water samples under illumination of 250nm LED

in its marked improvement in UV absorption. Whilst this method does not tell us exactly chemicals are present in the samples, it does give an indication of the general contamination levels. As the absorption is about the same for the two different UV light sources it suggests a wide absorption spectrum for the two water samples, peaking at lower wavelengths than 250nm. This can be from contribution of several peaks as there will be a mixture of different contaminants.

We will now look into the absorbance of single chemicals often found in water sources. The first chemical that we will investigate is Potassium Hydrogen Phtalate or KHP. KHP is used in large quantities in industry and large quantities of organic waste containing KHP is also generated [163].

The next chemical we will measure the absorption of is the pesticide clothiandin. Currently thiamethoxam and its breakdown product clothiandin dominate usage in North America cropping systems [164]. Whilst posing only a low risk to vertebrates if disposal instructions are followed, it is still shown to have high invertebrate mortality rate with high concentrations. Therefore it is important to be able to measure the contamination levels in waste water [165].

Finally the last chemical that we have investigated is an amino acid called tryptophan. Although tryptophan is present in most protein-based foods or dietary proteins the RDA is 5mg/kg for adults 19 years and over [166], as excess amounts of tryptophan can be toxic [167, 168]. Tryptophan-like fluorescence has also been used to measure the dissolved organic matter (DOM) content as micro-organisms have been shown to fluoresce at the same wavelength (280nm) as tryptophan [169, 170].

Figure 6.3*a*, 6.3*b* and 6.3*c* shows the chemical structure of KHP, clothiandin and tryptophan respectively. As each of these chemicals have benzene rings/derivatives it is expected that there will be a strong absorbance at around 250nm.

Figure 6.4 shows the absorption of a solution of KHP with varying concentration under illumi-

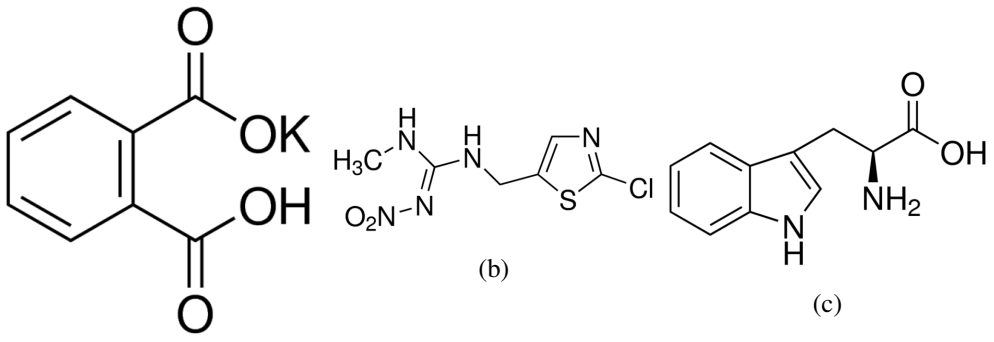

(a) (b) (c)

Figure 6.3: Chemical structure of a) KHP, b) clothiandin and c) tryptophan

nation under deuterium lamp and LED250J. From this figure it can be seen that KHP strongly absorbs in the UV and can be easily detected at concentrations as low as 5mg/L for both light sources although there appears to be more absorption for the deuterium lamp.

Figure 6.5 shows the absorption of solutions of varying concentrations of clothiandin in distilled water under illumination under 250J LED. First to note is that clothiandin appears to absorb more strongly at 250nm than KHP measured previously. Also from the figure it can be seen that concentrations as small as 0.1mg/L can be measurably detected, however in actual water samples the concentration of clothiandin is often a lot lower than this so an increased gain on

the detector would be needed [165].
Figure 6.6 shows the absorption of tryptophan solutions in distilled water under illumination of 250J LED. It can be seen that solutions of concentrations as small 1mg/L can be measurably detected.
All three of these contaminants have been proven to be measurable even down to small concentrations using UV transmission, this can further be improved with an increase to the gain or intensity of light source. Whilst using this method it would be impossible to distinguish between these 3 chemicals in a mixture, there exists possible ways of doing so using UV transmission such as DDS mentioned in the introduction of this section.

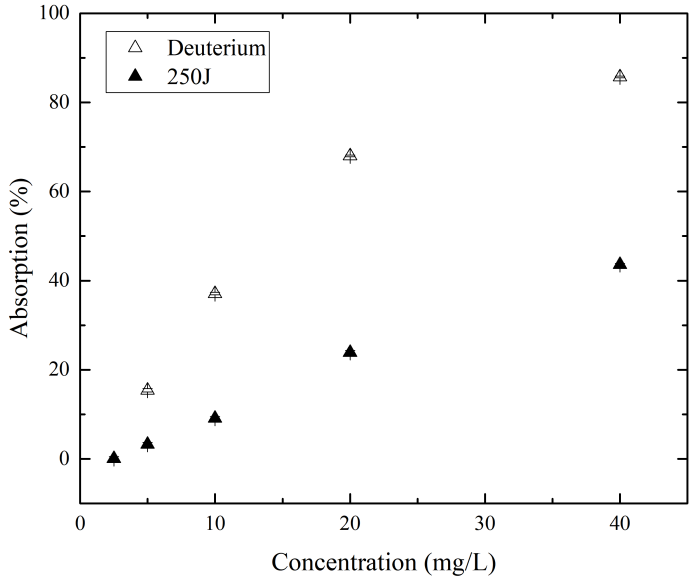

Figure 6.4: Absorption as function of concentration of KHP under illumination of deuterium lamp

6.4 Landing Assistance in Adverse Weather Conditions

6.4.1 Introduction

Another promising application of ThGEM-based GPM devices is in helping aircrafts land under bad visibility conditions. Currently only a certain number of runways are able to operate under CATIII weather conditions ($<$ 700ft visibility) and these runways are costly to operate and to install [171].
When landing under poor visibility conditions a pilot uses a precision landing system until a certain height called the decision height, here he must visually acquire the runway environment

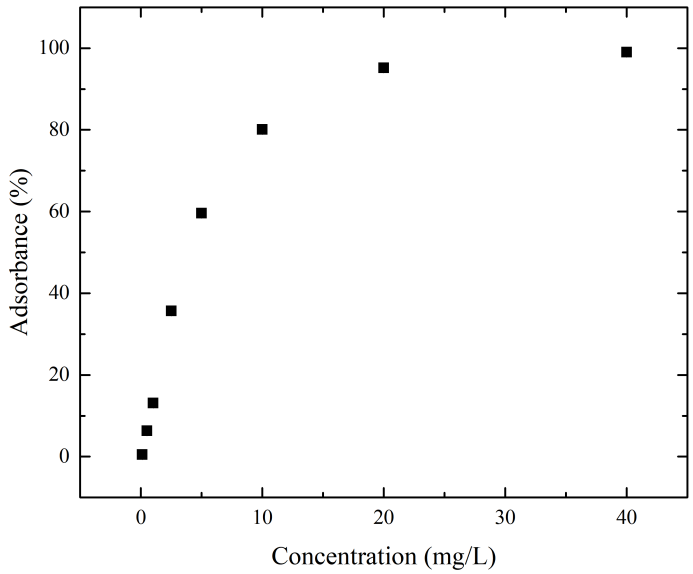

Figure 6.5: Absorption of different concentrations of clothiandin in distilled water solution under illumination of 250J LED

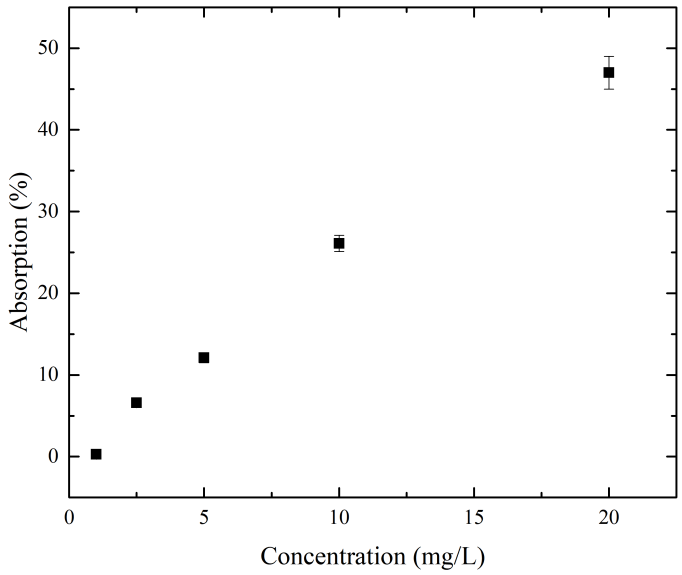

Figure 6.6: Absorption of Tryptophan in distilled water solutions with varying concentrations under illumination of 250J LED

[171]. Airport lights aid in defining the runway edge but under poor visibility conditions, very intense lights must be used which causes the high operation costs.

In the atmosphere shorter visibility weather is often defined as visibility less than 1km with the range of visibility between 1km and 500m called haze and visibility less than 500mm called fog. Haze consists of fine dust or small droplets suspended in air, where fog is when water droplets of a few microns up to a few tens of microns forms over the haze particles [172].
In 2001 Norris [171] outlined how UV technologies may be used to help with landing assistance. In the paper he introduces a optical sensor called "FogEye", which operates in the solar-blind part of the UV spectrum, using photomultiplier tubes to amplify the signal.They also proved its capability to see UV emitting runway lights at distances exceeding 2800 feet during 700 feet visibility conditions.
In this section we investigate the absorption of our UV light sources through foggy conditions and compare this to the absorption using an IR LED and photodiode system. To create the fog in the lab we use liquid nitrogen and by blowing air into the container of liquid nitrogen we can create something simulating atmospheric fog as shown in figure 6.7.

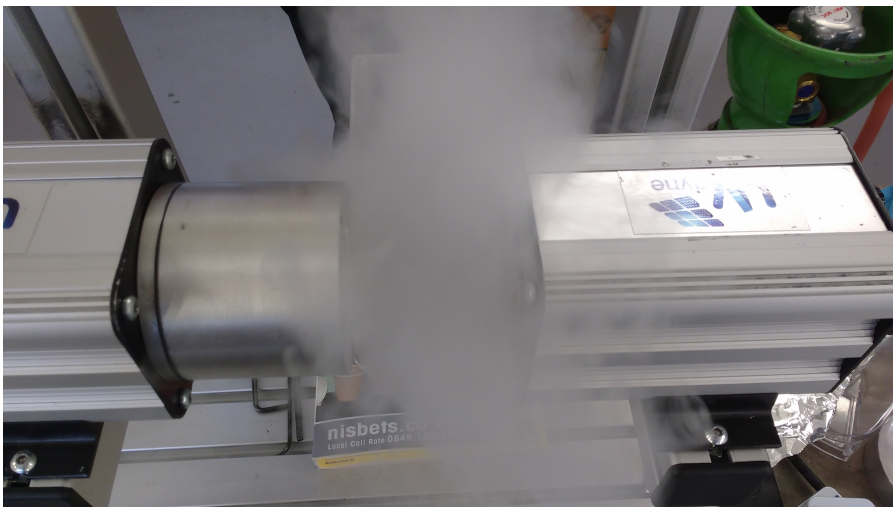

Figure 6.7: Experimental setup for fog absorption measurements. Left shows the detector and right the LED housing.

6.4.2 Experimental Results

Figure 6.8 shows example traces of absorption through fog for the IR and UV light sources. The 260nm LED was used for the UV LED source and a 950nm LED was used as the IR light source. The ThGEM was operated at reasonably low gains, which is the reason for the large noise in the trace. However due to the much lower reduction for UV it can be seen how useful UV light and detector system could be over IR or visible light systems. On average the IR LED is shown to have about a $(75 \pm 2)\%$ decrease in signal after exposed to 'fog' with the largest absorption of 80% of the original signal. Whereas for the 265nm LED and normal copper ThGEM, the mean absorption was much lower at $(27 \pm 1)\%$. Therefore it can immediately be seen that the UV part of the optical spectrum would be superior for any optical sensing in foggy conditions.

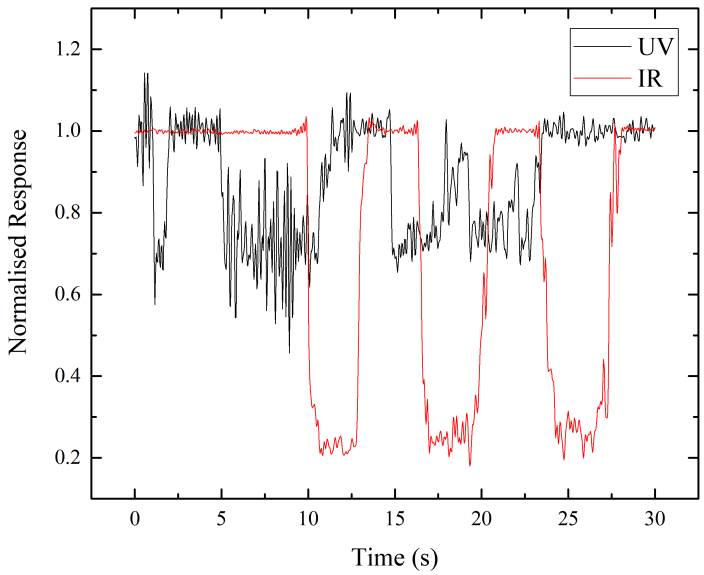

Figure 6.8: Normalised Response of UV and IR LEDs after exposure to fog

6.5 Reflection Measurements

6.5.1 Introduction

UV reflection measurements have not been investigated thoroughly due to the lack of experimental use of UV light for applications using reflection. However with the increase of cheap, high energy UVC LEDs the possibility of applications using UV reflection has increased. In particular UV reflection systems could be useful in vehicles for collision avoidance (for both automobiles [173, 174] and airplanes [175]), road monitoring [176] and/or sensors in self-driving cars.

In this section we will outline the reflection of various materials under different wavelengths of UV. We will also investigate reflection in terms of potentially being used in automotive sensors. A collision avoidance sensor could consist of a forward facing sensor element made from GPMs and a periodically pulsed UV light source. Reflections from the car in front or other reflective surfaces and the delay in measurement can give a direct measurement of how far away they are and the speed at which they are travelling. Also complete blocking of the light may warn the driver of potential risks such as pedestrians. Similar to the Light Detection and Ranging (LiDAR) systems already used, which use pulses of infra-red lasers to map the local enviroment and directly measure distance and velocities of objects [177].

Perhaps a more simple sensor to use on a vehicle would be a reflection off the road surface

which could be used to warn the driver of icy conditions or other hazards in the road (such as potholes and debris in the road). Also another use of UV reflection off the road surface could be in ensuring the car stays within a lane, via use of reflective strips or paint in the road, which could be very useful for self-driving cars. UV sensors have also been suggested for residual salt monitoring of road surfaces for applications in winter maintenance. [176]
Near-Infrared detection of the presence of water is well understood from the absorption of water at these wavelengths [178], however there is an interest in being able to distinguish water from other forms such as ice and snow. UV reflection measurements coupled with the current infrared detectors could allow the ability for real-time remote sensing of road conditions with the ability to distinguish between water, ice and snow.

6.5.2 Results

Coloured Paper

Figure 6.9 shows the reflectivity of different coloured paper under the illumination from the deuterium lamp for 2 different runs with different biases. A plain Cu GGEM was used to measure the reflectivity from the samples. The signal shown is the percentage increase from the reflectivity from black foam which was measured before and after each sample. This can be a control and removes problems from an increase or decrease in gain over time.

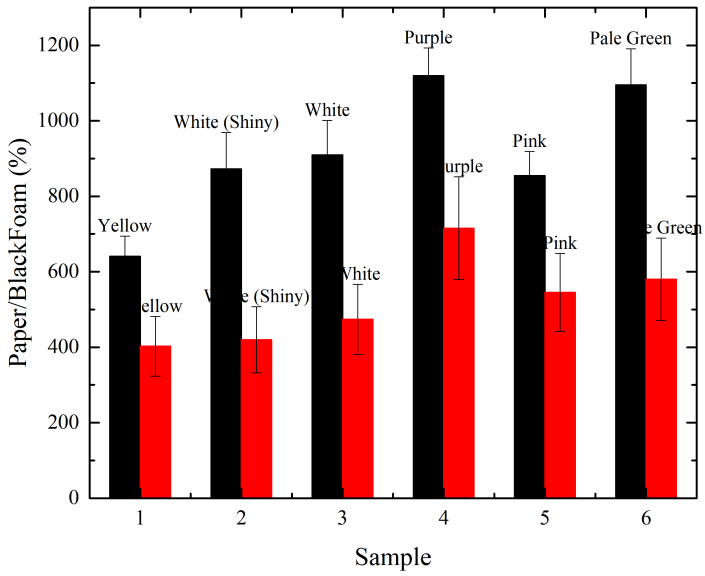

Figure 6.9: UV reflection from different coloured papers under illumination from deuterium lamp

Despite the large spread in the data from one bias to the other, in both runs the purple and pale green card gives the highest and second highest response. The shiny white card gave less signal than the white card for both runs, whilst the pink card was higher for low bias but smaller for high bias run. For both runs the yellow card gave the lowest signal. This suggests that more brightly coloured surfaces will reflect more UV light.

Ice on Tarmac

To investigate the potential usefulness of ThGEMs as a road monitoring detector, we compared reflection measurements of both tarmac and ice. To create the ice on the tarmac liquid nitrogen was used to rapidly cool water poured onto the surface of tarmac.
An example measurement of reflection off both tarmac and ice is shown in figure 6.10. Here it can be seen that the reflectivity of the ice is about 6 times greater than that of tarmac, the light source used for these measurements was the pond lamp with peak wavelength emission at 253.7nm. An example measurement of reflection off both tarmac and ice is shown in figure 6.10. Here it can be seen that the reflectivity of the ice is about 6 times greater than that of tarmac, the light source used for these measurements was the pond lamp with peak wavelength emission at 253.7nm.

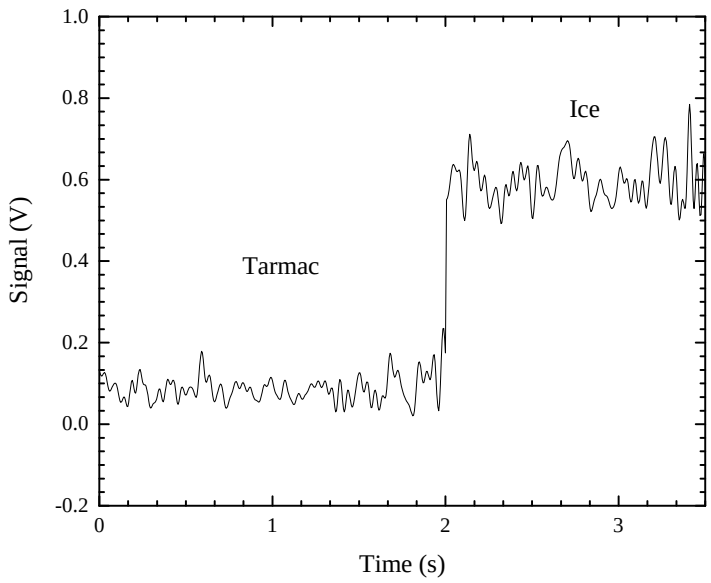

Figure 6.10: Reflection off tarmac and then ice for a ThGEM with Mg photocathode under a bias of kV and illumination using the 11W pond lamp.

6.6 Conclusions

Several applications of THGEM-based UV GPMs have been investigated with some promising results.

To investigate the functionality of GPMs as a possible receiver for a NLOS communication system we have investigated the signal as a function of distance and receiver angle to the optical axis and the transmitter. It was found that the power of the experimentally determined extinction law is lower for 50 to 60 degrees than compared to direct line of sight. It was also found that at higher angles (70°) the signal suffers an extra drop most likely due to the fact that the emission solid angle no longer directly enters the window of the detector, however the fact that some signal is still present is a strong indicator of scattering in the atmosphere despite the low power UV light source and small distances used in our experiments.

Unfortunately our limitation of UV light sources in laboratory have limited our testing of scattering in the atmosphere and subsequently the effectiveness of the GPMs as a detector for a NLOS communication system. Also it was found that large detector areas would be needed to receive measurable signals even with direct line of sight. Therefore the gain of the detectors would first need to be improved. The most simple way of achieving this would to be operate at lower pressures or to cascade several ThGEM elements.

The GPM devices also showed that they can work as water monitoring sensors due to the strong absorption at UV ranges of hydrocarbon compounds such as benzene. Common water contaminants such as KHP, clothiandine and tryptophan were investigated and concentrations were detected at 5mg/L for KHP, 0.1mg/L for Clothiandin and 1mg/L for tryptophan. However for trace contamination in water supplies often resolutions of μg/L is needed. As in the case of the NLOS communication by improving the gain on the ThGEM system we could improve the sensitivity of these detectors.

Although species determination in a mixture is not possible with the measurements done in this thesis due to overlapping and broad absorption peaks of various chemicals, it can be taken further by analysing the derivatives from varying wavelengths using DDS [162] as discussed.

We have also investigated the transmission of UV through fog and its possible application to guiding aircraft through landing procedure under poor visibility conditions. It was found that with the 'artificial fog' produced in the lab that 260nm showed much less attenuation than 950nm, with on average only a $27 \pm 1\%$ reduction in signal compared to a $75 \pm 2\%$ reduction in signal.

Finally we investigated the reflectivity of different materials, including coloured paper which showed that the purple colour seemed to reflect the most UV. Whereas, other bright colours and shiny paper (reflective in the visible) showed no improvement in reflectivity in the UV. We also investigated the difference in reflectivity of ice formed on tarmac, in the view of a road monitoring sensor on vehicles. Although small, there is a increase in reflectivity when comparing ice to tarmac. Therefore it should be possible to use a ThGEM-based GPM device to monitor a road surface and relay if there are icy conditions on the road.

Chapter 7

Conclusions and Future Work

7.1 Conclusions

In chapter 3 the photocurrent from both ThGEMs and the novel design, GGEMs were investigated over long time periods. It was found for both designs that there was long term rising in the signal over a period of hours to days. The timescales and size of rising appeared to vary from sample to sample suggesting that it depends on local variations in either the environment or the detector element itself.

The fact that GGEMs still exhibit this rising behaviour when they have no dielectric between the holes and therefore no etched rims, appears to contradict the assumption from Pitt et al. [64] that the long term rising effect was due to an accumulation of charge on the top rim. It is possible, however, that the dielectric in the table used to hold the device in place (PEEK in the case of the GGEMs) could be charging up in the place of the etched rims.

However it did appear that the size of the etched rims changed the rising behaviour of the ThGEMs with 0.1mm etched rims showing the most rising behaviour and bigger or smaller rims resulted in a rising behaviour very similar to that of the GGEMs.

Another possible contributor to the change in signal over time are residual contamination in the gas or outgassing of components under HV. Flushing the chamber through a period of 24 hours and baking the chamber to remove residual contamination from the chamber made no noticeable difference and therefore it was assumed that this had little or no effect on the rising signal. Outgassing of components was measured using a mass spectrometer, but the results were inconclusive, however no noticeable change the mass spectrum was noted over time from outgassing components.

It was found that Brasso polished copper ThGEMs had a much higher increase in signal under illumination than solvent cleaned copper despite having a similar or only slightly smaller work function. In chapter 5 the RQE was measured using the TEAS laser and it was found that the RQE was much higher at lower wavelengths (< 245nm).

Using XPS it was discovered that polishing the copper surface removed the $CuO/Cu(OH)_2$ from the surface leaving behind a strong metallic component. This could be the reason for the change

in signal but CuO must have a similar work function to the metallic copper.
It was also found that cleaning the copper in a solution of Micro-90 and distilled water significantly reduced the work function to about 4eV. From the XPS data it was found that there was a extra peak associated to Na present, this was believed to come from the Micro-90 cleaning solution as it contains 10 to 25% of ethylene diamine tetraacetic acid tetrasodium (EDTA-Na_4). The Na could act as a surface dipole causing the work function to drop. The effect of alkali metals reducing the work function of thin metal oxide layers and transition metals has been found in literature [128, 127]
ThGEMs cleaned in M90 solution were found to have worse photocurrent under illumination than samples that are solvent cleaned or polished despite having a lower work function.
As well as the investigation of the behaviour of ThGEMs with the standard copper from the PCB being used as a photocathode. ZnO and MgO films were deposited and characterised using XPS and KP measurements for chemical determination and work function measurements respectively.
In chapter 4 MgO was found to have a mean work function of 3.64 ± 0.04eV when oxidised under vacuum conditions but a much higher work function of 4.15 ± 0.17eV when oxidised in air. The work function of 3.64eV is similar to values of work function found in literature such as 3.66eV from Michaelson et al. [131] however the value of 4.15eV is quite a bit higher than found in literature, approaching the values of WF for zinc instead.
From the XPS data it can be seen that the sample oxidised in vacuum had a much larger $Mg(OH)_2$ component and the sample oxidised in ambient conditions had a larger $MgCO_3$ component.
The work function of MgO films were also found to decrease over time when left in ambient. XPS of samples of MgO films left in ambient conditions showed that there was a larger metallic component in the Mg2p region suggesting that the oxide layer is somehow removed over time, this could be from an unstable surface or abrasive contact when moving around samples. As well as this however they showed an increase in the MgO component in the O1s region, which could explain the decrease in work function over time.
In chapter 5, MgO films were also shown to have a large spread in the relative quantum efficiency (RQE) under illumination, with high work function films of 4eV and above giving worse signal than even solvent cleaned copper but some MgO films with much lower work function giving almost twice the RQE at 210nm. This suggests that the QY of metallic Mg is quite high but samples with a large $MgCO_3$ component have poor QY.
In chapter 4, the mean work function of ZnO oxidised in vacuum was measured to be 4.11 ± 0.11eV which is quite similar to the annealed surface measurement from Gutmann et al. [107]. Whereas the ZnO oxidised in ambient where found to have slightly higher work function of 4.35 ± 0.12eV, which was more similar to the freshly cleaved single crystals of ZnO from Moorman et al. [136] and samples deposited electrochemically were found to have work function of 4.4 ± 0.2eV on average.
From the LMM spectra ZnO films oxidised in vacuum were found to have a larger metallic

and ZnO component and ambient oxidised and electrochemically deposited samples main peak matched almost perfectly with the LMM peak for hydrozincite ($Zn_5(CO_3)_2(OH)_6$) from Dake et al. [139].

This suggests that the higher WF from ambient samples and electrochemically deposited ZnO films comes from a higher concentration of $Zn(OH)_2$ and $ZnCO_3$, possibly in the state of hydrozincite. This was further evidenced in the O 1s region where samples left in ambient showed mainly $Zn(OH)_2$ component and electrochemically deposited films showed almost no ZnO and more $ZnCO_3$.

In chapter 5 we investigated the photocurrent under illumination of a variety of ZnO films. Again as in the case of magnesium there appears to be a weak dependency on the work function measured and the photocurrent measured with samples with lower work function giving greater photocurrent under illumination.

The RQE values for ZnO have a wide range from 4.5E-7 to 3.5E-6 electrons per incident photon for a 1.2kV bias, which gives it very similar values to that for MgO films. But for the same WF ZnO appears to have a higher RQE, which matches with the TEAS data which showed much higher response for ZnO film. Also electrochemically deposited films appear to have the highest RQE despite having higher WF than the PVD samples.

We attempted to measure the QY directly emitted from the photocathode surface using a mesh at +ve bias a short distance away from the sample surface, however it was noted that large values of photocurrent were measured and at a certain bias there was an exponential rise in signal suggesting that some multiplication around the wires of the mesh was occurring, limiting the ability to accurate measurements of QY.

Work function reduction was achieved by coating our photocathodes with ultra-thin layer of PEI using the spin coater. It was found that on copper surfaces lower speeds resulted in a larger ΔWF but at very low speeds some uniformity issues arose so a spin speed of 2000rpm was used. It was found that the WF degraded to the initial WF over a period of a month and suffered a big drop over a day of being left in ambient conditions. This somewhats limits its use in gaseous detectors as it does not have long term stability.

PEI was also coated on MgO and ZnO films, it was found that the change in WF appeared to be dependent on the initial WF with ZnO films having lower work function beforehand showing little to no change after being coated in PEI and magnesium showing an increase in work function.

In Chapter 6 we investigated the potential usefulness of ThGEM-based GPMs in a variety of experimental applications, one of these applications was NLOS communication. It was found, using a simple $1/r^2$ power extinction law that to achieve measurable signals at long distances (1km) for a LOS system a detector area of $2.4 \pm 0.6\text{m}^2$ would be needed and therefore even larger detector area would be needed for a NLOS system. However it should be possible to reduce this number by either cascading ThGEMs to approve the overall multiplication of the detectors or by using a more powerful UV light source.

The signal was also measured as a function of detector angle with respect to the optical axis and transmitter. It was found that the power of the extinction law was around 1.7 between 50 and 60 degrees and at higher angles (70°) the power goes up to about 3. This is most likely because at 70 the emission solid angle no longer directly enters the detector window and we are relying purely on scattering in the atmosphere.
Successful water absorption measurements for 3 different chemicals (KHP, clothiandin and tryptophan) was achieved with sensitivities of 5mg/L for KHP, 0.5mg/L for clothiandin and 2.5mg/L for tryptophan. However the quantities that would need to be measured would be more on the order of μg/L, therefore as in the case of NLOS communication an increase in the detectors gain is needed before it can be implemented into a water monitoring device.
Another possible application investigated was guiding airplanes towards runways under poor visibility conditions. Using liquid nitrogen we simulated foggy conditions in the lab and compared the absorption of 260nm LED using our ThGEM detector and a 950nm LED using a photodiode. It was found on average that the absorption of the 260nm LED was $27 \pm 1\%$ whereas the absorption from the 950nm LED was found to be much higher at $75 \pm 2\%$.

7.2 Future Work

By removing the table support to the GGEMs and removing any dielectric in contact with HV bias, we can investigate the contribution of the charging of the dielectric to the rising in signal over time. If the long term rising is still present after the removal of all the dielectric in contact with the electrode it would mean that the rising in signal must be from the gaseous properties instead.
Further investigation of the gas mixture during operation as a GPM using the mass spectrometer could also help determine the dominant contribution to the rising signal.
XPS measurements of the same sample with increasing exposure to ambient conditions (such as O_2 and H_2O) could give us more accurate representation of how the change in the surfaces chemical structure effects the work function and QY of our photocathodes grown.
By better control of the two fluxes from Mg and Zn effusion cells, it should be possible to grow MgZn alloys which have WF somewhere between MgO and ZnO i.e. 4eV which can be solar blind but still hopefully give a high QY under illumination of UVC light.
Recalibration of the light sources is needed to determine accurate photon flux at the surface during photocurrent measurements. Especially for the deuterium lamp as the RQE calculated is lower than expected from the other light sources. A powermeter capable of going to lower wavelengths is needed to measured the power and spectrum from the deuterium lamp.
To remove the problems of gain from the wire mesh used to collect the photocurrent, future QY measurements would need to be done in vacuum conditions so that there is no electron avalanche effecting the results of QY.

Although initial measurements suggest that it should be possible to use ThGEM-based GPMs as the detector element in a NLOS communication system. To investigate further either a larger gain is required (i.e. by cascading ThGEM elements) or a more powerful UV light source is required. It would also be useful to look into the extinction law as function of both transmitter and receiver angle rather than just reciever angle.

Bibliography

[1] Fabio Sauli. Radiation imaging with gaseous detectors. *Nuclear Instruments and Methods in Physics Research Section A: Accelerators, Spectrometers, Detectors and Associated Equipment*, 878:1–9, 2018.

[2] WF Krolikowski and WE Spicer. Photoemission studies of the noble metals. i. copper. *Physical Review*, 185(3):882, 1969.

[3] DT Palmer. A review of metallic photocathode-research. *SLAC Publications and Report No. SLAC-TN-05-080*, 2005.

[4] Alex M Boehm, Jochen Wieser, Kamal Butrouna, and Kenneth R Graham. A new photon source for ultraviolet photoelectron spectroscopy of organic and other damage-prone materials. *Organic Electronics*, 41:9–16, 2017.

[5] Yoshihiko Muramoto, Masahiro Kimura, and Suguru Nouda. Development and future of ultraviolet light-emitting diodes: Uv-led will replace the uv lamp. *Semiconductor Science and Technology*, 29(8):084004, 2014.

[6] MA Juárez, JA Martínez, G Vázquez, JM Sosa, PR Martínez, I Villanueva, and R Osorio. A model for electrical characteristics of high power uv led. In *Power Electronics (CIEP), 2016 13th International Conference on*, pages 110–115. IEEE, 2016.

[7] Wenhong Sun, Vinod Adivarahan, Maxim Shatalov, Youngbae Lee, Shuai Wu, Jinwei Yang, Jianping Zhang, and M Asif Khan. Continuous wave milliwatt power algan light emitting diodes at 280 nm. *Japanese journal of applied physics*, 43(11A):L1419, 2004.

[8] V Adivarahan, S Wu, JP Zhang, A Chitnis, M Shatalov, V Mandavilli, R Gaska, and M Asif Khan. High-efficiency 269 nm emission deep ultraviolet light-emitting diodes. *Applied Physics Letters*, 84(23):4762–4764, 2004.

[9] V_ Adivarahan, W_ H Sun, A Chitnis, M Shatalov, S Wu, HP Maruska, and M Asif Khan. 250 nm algan light-emitting diodes. *Applied physics letters*, 85(12):2175–2177, 2004.

[10] Hideki Hirayama, Noritoshi Maeda, Sachie Fujikawa, Shiro Toyoda, and Norihiko Kamata. Recent progress and future prospects of algan-based high-efficiency deep-

ultraviolet light-emitting diodes. *Japanese Journal of Applied Physics*, 53(10):100209, 2014.

[11] Christian A Gueymard. The suns total and spectral irradiance for solar energy applications and solar radiation models. *Solar energy*, 76(4):423–453, 2004.

[12] Elfrida M Carstea, John Bridgeman, Andy Baker, and Darren M Reynolds. Fluorescence spectroscopy for wastewater monitoring: a review. *Water Research*, 95:205–219, 2016.

[13] Jian Chen, Stephanie Loeb, and Jae-Hong Kim. Led revolution: fundamentals and prospects for uv disinfection applications. *Environmental Science: Water Research & Technology*, 3(2):188–202, 2017.

[14] H Peng, E Makarona, Y He, Y-K Song, AV Nurmikko, J Su, Z Ren, M Gherasimova, S-R Jeon, G Cui, et al. Ultraviolet light-emitting diodes operating in the 340 nm wavelength range and application to time-resolved fluorescence spectroscopy. *Applied Physics Letters*, 85(8):1436–1438, 2004.

[15] Harvey Lui, Haishan Zeng, Calum E MacAulay, Branko Palcic, and David I McLean. Fluorescence scope system for dermatologic diagnosis, February 1 2000. US Patent 6,021,344.

[16] Zhengyuan Xu and Brian M Sadler. Ultraviolet communications: potential and state-of-the-art. *IEEE Communications Magazine*, 46(5):67–73, 2008.

[17] Z Alaie, S Mohammad Nejad, and MH Yousefi. Recent advances in ultraviolet photodetectors. *Materials Science in Semiconductor Processing*, 29:16–55, 2015.

[18] D Renker and E Lorenz. Advances in solid state photon detectors. *Journal of Instrumentation*, 4(04):P04004, 2009.

[19] A Breskin, V Peskov, M Cortesi, R Budnik, R Chechik, S Duval, D Thers, AEC Coimbra, JMF Dos Santos, JAM Lopes, et al. Csi-thgem gaseous photomultipliers for rich and noble-liquid detectors. *Nuclear Instruments and Methods in Physics Research Section A: Accelerators, Spectrometers, Detectors and Associated Equipment*, 639(1):117–120, 2011.

[20] Amos Breskin. Liquid hole-multipliers: A potential concept for large single-phase noble-liquid tpcs of rare events. In *Journal of Physics: Conference Series*, volume 460, page 012020. IOP Publishing, 2013.

[21] Samuel Duval, Lior Arazi, Amos Breskin, Ranny Budnik, Wan-Ting Chen, Hervé Carduner, AEC Coimbra, Marco Cortesi, Roy Kaner, Jean-Pierre Cussonneau, et al. Hybrid multi micropattern gaseous photomultiplier for detection of liquid-xenon scintillation.

Nuclear Instruments and Methods in Physics Research Section A: Accelerators, Spectrometers, Detectors and Associated Equipment, 695:163–167, 2012.

[22] J Warren Keuffel. Parallel-plate counters. *Review of Scientific Instruments*, 20(3):202–208, 1949.

[23] P Fonte, Vladimir Peskov, and Fabio Sauli. Feedback and breakdown in parallel-plate chambers. *Nuclear Instruments and Methods in Physics Research Section A: Accelerators, Spectrometers, Detectors and Associated Equipment*, 305(1):91–110, 1991.

[24] G. Charpak, R. Bouclier, T. Bressani, J. Favier, and . Zupani. The use of multiwire proportional counters to select and localize charged particles. *Nuclear Instruments and Methods*, 62(3):262 – 268, 1968. ISSN 0029-554X.

[25] Fabio Sauli and Archana Sharma. Micropattern gaseous detectors. *Annual Review of Nuclear and Particle Science*, 49(1):341–388, 1999.

[26] MJ Neumann and TA Nunamaker. Modification of the charpak chamber with foil supported conductors. *IEEE Transactions on Nuclear Science*, 17(3):43–49, 1970.

[27] E Christophel and M Dracos. The micro-gap wire chamber. *Nuclear Instruments and Methods in Physics Research Section A: Accelerators, Spectrometers, Detectors and Associated Equipment*, 398(2-3):195–202, 1997.

[28] A Oed. Position-sensitive detector with microstrip anode for electron multiplication with gases. *Nuclear Instruments and Methods in Physics Research Section A: Accelerators, Spectrometers, Detectors and Associated Equipment*, 263(2-3):351–359, 1988.

[29] Yannis Giomataris, Ph Rebourgeard, Jean Pierre Robert, and Georges Charpak. Micromegas: a high-granularity position-sensitive gaseous detector for high particle-flux environments. *Nuclear Instruments and Methods in Physics Research Section A: Accelerators, Spectrometers, Detectors and Associated Equipment*, 376(1):29–35, 1996.

[30] Purba Bhattacharya, D Sankar Bhattacharya, Supratik Mukhopadhyay, Sudeb Bhattacharya, Nayana Majumdar, Sandip Sarkar, Paul Colas, and David Attie. Investigation of ion backflow in bulk micromegas detectors. *Journal of Instrumentation*, 10(09):P09017, 2015.

[31] Fabio Sauli. Gem: A new concept for electron amplification in gas detectors. *Nuclear Instruments and Methods in Physics Research Section A: Accelerators, Spectrometers, Detectors and Associated Equipment*, 386(2-3):531–534, 1997.

[32] Jaroslav Vavra, E Shefer, AF Buzulutskov, Amos Breskin, and R Chechik. Study csi photocathodes: volume resistivity and ageing. Technical report, SCAN-9701018, 1996.

[33] Fabio Sauli, L Ropelewski, and P Everaerts. Ion feedback suppression in time projection chambers. *Nuclear Instruments and Methods in Physics Research Section A: Accelerators, Spectrometers, Detectors and Associated Equipment*, 560(2):269–277, 2006.

[34] Eugenio Nappi and Vladimir Peskov. *Imaging gaseous detectors and their applications*. John Wiley & Sons, 2013.

[35] M Alexeev, CDR Azevedo, R Birsa, F Bradamante, A Bressan, M Chiosso, P Ciliberti, PMM Correia, S Dalla Torre, SS Dasgupta, et al. Ion back flow reduction in a thgem based detector. In *Nuclear Science Symposium and Medical Imaging Conference (NSS/MIC), 2012 IEEE*, pages 1165–1171. IEEE, 2012.

[36] FD Amaro, JFCA Veloso, A Breskin, R Chechik, and JMF Dos Santos. Operation of mhsp multipliers in high pressure pure noble-gas. *Journal of instrumentation*, 1(04): P04003, 2006.

[37] A Lyashenko, A Breskin, R Chechik, JMF Dos Santos, FD Amaro, and JFCA Veloso. Efficient ion blocking in gaseous detectors and its application to gas-avalanche photomultipliers sensitive in the visible-light range. *Nuclear Instruments and Methods in Physics Research Section A: Accelerators, Spectrometers, Detectors and Associated Equipment*, 598(1):116–120, 2009.

[38] FD Amaro, C Santos, JFCA Veloso, A Breskin, R Chechik, and JMF Dos Santos. The thick-cobra: a new gaseous electron multiplier for radiation detectors. *Journal of Instrumentation*, 5(10):P10002, 2010.

[39] Rui de Olivera and Marco Cortesi. First performance evaluation of a multi-layer thick gaseous electron multiplier with in-built electrode meshesmm-thgem. *Journal of Instrumentation*, 13(06):P06019, 2018.

[40] M Cortesi, S Rost, W Mittig, Y Ayyad-Limonge, D Bazin, J Yurkon, and A Stolz. Multilayer thick gas electron multiplier (m-thgem): A new mpgd structure for high-gain operation at low-pressure. *Review of Scientific Instruments*, 88(1):013303, 2017.

[41] John S Townsend. Xvii. the conductivity produced in gases by the motion of negatively charged ions. *The London, Edinburgh, and Dublin Philosophical Magazine and Journal of Science*, 1(2):198–227, 1901.

[42] Takahiko Aoyama. Generalized gas gain formula for proportional counters. *Nuclear Instruments and Methods in Physics Research Section A: Accelerators, Spectrometers, Detectors and Associated Equipment*, 234(1):125–131, 1985.

[43] Fabio Sauli. *Gaseous radiation detectors: fundamentals and applications*. Number 36. Cambridge University Press, 2014.

[44] AA Kruithof and FM Penning. Determination of the townsend. ionization coefficient α for mixtures of neon and argon. *Physica*, 4(6):430–449, 1937.

[45] ZM Jelenak, ZB Velikić, JV Božin, Z Lj Petrović, and BM Jelenković. Electronic excitation of the 750-and 811-nm lines of argon. *Physical Review E*, 47(5):3566, 1993.

[46] Paul L Morton. Ionization currents in non-uniform electric fields. *Physical Review*, 70 (5-6):358, 1946.

[47] GS Hurst and CE Klots. Elementary processes in irradiated noble gases. *Adv. Radiat. Chem*, 5(1), 1976.

[48] A Buzulutskov, A Bondar, and A Grebenuk. Infrared scintillation yield in gaseous and liquid argon. *EPL (Europhysics Letters)*, 94(5):52001, 2011.

[49] A Buzulutskov, L Shekhtman, A Bressan, A Di Mauro, Leszek Ropelewski, Fabio Sauli, and S Biagi. Gem operation in pure noble gases and the avalanche confinement. *Nuclear Instruments and Methods in Physics Research Section A: Accelerators, Spectrometers, Detectors and Associated Equipment*, 433(1-2):471–475, 1999.

[50] Tetsuhiko Takahashi, Susumu Himi, Masayo Suzuki, Jian-zhi RUAN Gen, and Shinzou Kubota. Emission spectra from ar xe, ar kr, ar n2, ar ch4, ar co2 and xe n2 gas scintillation proportional counters. *Nuclear instruments and methods in physics research*, 205(3):591–596, 1983.

[51] MJ Druyvesteyn and Fi M Penning. The mechanism of electrical discharges in gases of low pressure. *Reviews of Modern Physics*, 12(2):87, 1940.

[52] Heikki Sipilä. Energy resolution of the proportional counter. *Nuclear Instruments and Methods*, 133(2):251–252, 1976.

[53] Simon Ramo. Currents induced by electron motion. *Proceedings of the IRE*, 27(9):584–585, 1939.

[54] Mohamed Rabie and Christian M Franck. A study of the avalanche-to-streamer transition in arbitrary gases by particle simulation. *Journal of Physics D: Applied Physics*, 49(17): 175202, 2016.

[55] Heinz Raether. Electron avalanches and breakdown in gases. 1964.

[56] V Biteman, S Guinji, V Peskov, H Sakurai, E Silin, T Sokolova, and I Radionov. Position sensitive gaseous photomultipliers. *Nuclear Instruments and Methods in Physics Research Section A: Accelerators, Spectrometers, Detectors and Associated Equipment*, 471(1-2):205–208, 2001.

[57] V Peskov and P Fonte. Research on discharges in micropattern and small gap gaseous detectors. *arXiv preprint arXiv:0911.0463*, 2009.

[58] R Galea, J Dodd, Y Ju, M Leltchouk, W Willis, P Rehak, V Tcherniatine, A Buzulutskov, and D Pavlyuchenko. Gas purity effect on gem performance in he and ne at low temperatures. *IEEE transactions on nuclear science*, 53(4):2260–2263, 2006.

[59] G.F. Karabadzhak, V.D. Peskov, and E.R. Podolyak. Coordinate gas counters with superhigh energy resolution for plasma diagnostics. *Nuclear Instruments and Methods in Physics Research*, 217(1):56 – 64, 1983. ISSN 0167-5087.

[60] P Fonte, V Peskov, and B Ramsey. The fundamental limitations of high-rate gaseous detectors. In *Nuclear Science Symposium, 1998. Conference Record. 1998 IEEE*, volume 1, pages 91–95. IEEE, 1998.

[61] R Chechik, M Cortesi, Amos Breskin, D Vartsky, D Bar, and V Dangendorf. Thick gem-like (thgem) detectors and their possible applications. *arXiv preprint physics/0606162*, 2006.

[62] Maxim Alexeev, R Birsa, F Bradamante, A Bressan, M Büchele, Michela Chiosso, P Ciliberti, S Dalla Torre, S Dasgupta, O Denisov, et al. The gain in thick gem multipliers and its time-evolution. *Journal of Instrumentation*, 10(03):P03026, 2015.

[63] B Azmoun, W Anderson, D Crary, J Durham, T Hemmick, J Kamin, G Karagiorgi, K Kearney, G Keeler, E Kornacki, et al. A study of gain stability and charging effects in gem foils. In *Nuclear Science Symposium Conference Record, 2006. IEEE*, volume 6, pages 3847–3851. IEEE, 2006.

[64] M Pitt, PMM Correia, S Bressler, AEC Coimbra, D Shaked Renous, CDR Azevedo, JFCA Veloso, and A Breskin. Measurements of charging-up processes in thgem-based particle detectors. *arXiv preprint arXiv:1801.00533*, 2018.

[65] M Cortesi, V Peskov, G Bartesaghi, J Miyamoto, S Cohen, R Chechik, JM Maia, JMF dos Santos, G Gambarini, V Dangendorf, et al. Thgem operation in ne and ne/ch4. *Journal of Instrumentation*, 4(08):P08001, 2009.

[66] William Edward Spicer. Photoemissive, photoconductive, and optical absorption studies of alkali-antimony compounds. *Physical review*, 112(1):114, 1958.

[67] Antoine Kahn. Fermi level, work function and vacuum level. *Materials Horizons*, 3(1): 7–10, 2016.

[68] Pierre Hohenberg and Walter Kohn. Inhomogeneous electron gas. *Physical review*, 136 (3B):B864, 1964.

[69] Walter Kohn and Lu Jeu Sham. Self-consistent equations including exchange and correlation effects. *Physical review*, 140(4A):A1133, 1965.

[70] Sam De Waele, Kurt Lejaeghere, Michael Sluydts, and Stefaan Cottenier. Error estimates for density-functional theory predictions of surface energy and work function. *Physical Review B*, 94(23):235418, 2016.

[71] Leon I Maissel and Reinhard Glang. Handbook of thin film technology. *New York: McGraw-Hill, 1970, edited by Maissel, Leon I.; Glang, Reinhard*, 1970.

[72] Donald M Mattox. *Handbook of physical vapor deposition (PVD) processing*. William Andrew, 2010.

[73] Benoit N Illy, Amy C Cruickshank, Stefan Schumann, Raffaello Da Campo, Tim S Jones, Sandrine Heutz, Martyn A McLachlan, David W McComb, D Jason Riley, and Mary P Ryan. Electrodeposition of zno layers for photovoltaic applications: controlling film thickness and orientation. *Journal of Materials Chemistry*, 21(34):12949–12957, 2011.

[74] I Masanobu and O Takashi. Electrolyte optimization for cathodic growth of zno films. *J Electrochem Soc*, 143(3):53–58, 1996.

[75] T Mahalingam, VS John, M Raja, Yan-Kuin Su, and PJ Sebastian. Electrodeposition and characterization of transparent zno thin films. *Solar energy materials and solar cells*, 88 (2):227–235, 2005.

[76] Masanobu Izaki and Takashi Omi. Transparent zinc oxide films prepared by electrochemical reaction. *Applied Physics Letters*, 68(17):2439–2440, 1996.

[77] Dietrich Meyerhofer. Characteristics of resist films produced by spinning. *Journal of Applied Physics*, 49(7):3993–3997, 1978.

[78] DP Birnie. Spin coating technique. In *Sol-Gel Technologies for Glass Producers and Users*, pages 49–55. Springer, 2004.

[79] Walter H Brattain and John Bardeen. Surface properties of germanium. *Bell System Technical Journal*, 32(1):1–41, 1953.

[80] Leeor Kronik and Yoram Shapira. Surface photovoltage phenomena: theory, experiment, and applications. *Surface science reports*, 37(1-5):1–206, 1999.

[81] Victor E Henrich and Paul Anthony Cox. *The surface science of metal oxides*. Cambridge university press, 1996.

[82] Yu S Zharkikh and SV Lysochenko. Mechanic-electrical transformations in the kelvin method. *Applied Surface Science*, 400:71–76, 2017.

[83] ID Baikie, E Venderbosch, JA Meyer, and PJZ Estrup. Analysis of stray capacitance in the kelvin method. *Review of scientific instruments*, 62(3):725–735, 1991.

[84] RJ D'Arcy and NA Surplice. The effects of stray capacitance on the kelvin method for measuring contact potential difference. *Journal of Physics D: Applied Physics*, 3(4):482, 1970.

[85] ID Baikie, S Mackenzie, PJZ Estrup, and JA Meyer. Noise and the kelvin method. *Review of scientific instruments*, 62(5):1326–1332, 1991.

[86] Wilford N Hansen and Galen J Hansen. Standard reference surfaces for work function measurements in air. *Surface science*, 481(1-3):172–184, 2001.

[87] Ralph H Fowler. The analysis of photoelectric sensitivity curves for clean metals at various temperatures. *Physical review*, 38(1):45, 1931.

[88] Iain D Baikie, Angela C Grain, James Sutherland, and Jamie Law. Ambient pressure photoemission spectroscopy of metal surfaces. *Applied Surface Science*, 323:45–53, 2014.

[89] AA Holscher. A field emission retarding potential method for measuring work functions. *Surface Science*, 4(1):89–102, 1966.

[90] EE Huber Jr and CT Kirk Jr. Work function changes due to the chemisorption of water and oxygen on aluminum. *Surface Science*, 5(4):447–465, 1966.

[91] BJ Hopkins and JC Riviere. Work function values from contact potential difference measurements. *British Journal of Applied Physics*, 15(8):941, 1964.

[92] Jack M Hollander and William L Jolly. X-ray photoelectron spectroscopy. *Accounts of chemical research*, 3(6):193–200, 1970.

[93] Paul Van der Heide. *Secondary Ion Mass Spectrometry: An Introduction to Principles and Practices*. John Wiley & Sons, 2014.

[94] Chuan C Chang. Auger electron spectroscopy. *Surface Science*, 25(1):53–79, 1971.

[95] Charles C Chusuei and D Wayne Goodman. X-ray photoelectron spectroscopy. *Encyclopedia of physical science and technology*, 17:921–938, 2002.

[96] JE Castle, H Chapman-Kpodo, A Proctor, and AM Salvi. Curve-fitting in xps using extrinsic and intrinsic background structure. *Journal of Electron Spectroscopy and Related Phenomena*, 106(1):65–80, 2000.

[97] CD Wagner. Auger parameter in electron spectroscopy for the identification of chemical species. *Analytical Chemistry*, 47(7):1201–1203, 1975.

[98] D Shaked Renous, Arindam Roy, Amos Breskin, and Shikma Bressler. Gain stabilization in micro pattern gaseous detectors: methodology and results. *Journal of Instrumentation*, 12(09):P09036, 2017.

[99] C Shalem, R Chechik, A Breskin, and K Michaeli. Advances in thick gem-like gaseous electron multiplierspart i: atmospheric pressure operation. *Nuclear Instruments and Methods in Physics Research Section A: Accelerators, Spectrometers, Detectors and Associated Equipment*, 558(2):475–489, 2006.

[100] BK Singh, E Shefer, A Breskin, R Chechik, and N Avraham. Csbr and csi uv photocathodes: new results on quantum efficiency and aging. *Nuclear Instruments and Methods in Physics Research Section A: Accelerators, Spectrometers, Detectors and Associated Equipment*, 454(2-3):364–378, 2000.

[101] DJ Rogers, P Bove, X Arrateig, VE Sandana, FH Teherani, M Razeghi, R McClintock, E Frisch, and S Harel. The new oxide paradigm for solid state ultraviolet photodetectors. In *Oxide-based Materials and Devices IX*, volume 10533, page 105331P. International Society for Optics and Photonics, 2018.

[102] DH Dowell, I Bazarov, B Dunham, K Harkay, C Hernandez-Garcia, R Legg, H Padmore, T Rao, J Smedley, and W Wan. Cathode r&d for future light sources. *Nuclear Instruments and Methods in Physics Research Section A: Accelerators, Spectrometers, Detectors and Associated Equipment*, 622(3):685–697, 2010.

[103] RB Cairns and JAR Samson. Metal photocathodes as secondary standards for absolute intensity measurements in the vacuum ultraviolet. *JOSA*, 56(11):1568–1573, 1966.

[104] Erskine JT Burns and John F Thurston. The use of some metal photocathodes for absolute intensity measurements in the soft x-ray-vacuum ultraviolet. *Applied Spectroscopy*, 31(4): 317–320, 1977.

[105] BE Hayden, E Schweizer, R Kötz, and AM Bradshaw. The early stages of oxidation of magnesium single crystal surfaces. *Surface Science*, 111(1):26–38, 1981.

[106] Quan Yuan, Aaron W Baum, R Fabian W Pease, and Piero Pianetta. Effect of oxygen adsorption on the efficiency of magnesium photocathodes. *Journal of Vacuum Science & Technology B: Microelectronics and Nanometer Structures Processing, Measurement, and Phenomena*, 21(6):2830–2833, 2003.

[107] S Gutmann, M Conrad, MA Wolak, MM Beerbom, and R Schlaf. Work function measurements on nano-crystalline zinc oxide surfaces. *Journal of Applied Physics*, 111(12): 123710, 2012.

[108] O Siegmund, J Vallerga, J McPhate, J Malloy, A Tremsin, A Martin, M Ulmer, and B Wessels. Development of gan photocathodes for uv detectors. *Nuclear Instruments and Methods in Physics Research Section A: Accelerators, Spectrometers, Detectors and Associated Equipment*, 567(1):89–92, 2006.

[109] Ferechteh Hosseini Teherani, David C Look, and David J Rogers. Oxide-based materials and devices iv. In *Proc. of SPIE Vol*, volume 8626, pages 862601–1, 2013.

[110] YN Hou, ZX Mei, HL Liang, CZ Gu, and XL Du. Monolithic color-selective ultraviolet (266–315 nm) photodetector based on a wurtzite mgxzn1- xo film. *Applied Physics Letters*, 105(13):133510, 2014.

[111] JD Hwang, CC Yang, and CM Chu. Mgzno/zno two-dimensional electron gas photodetectors fabricated by radio frequency sputtering. *ACS applied materials & interfaces*, 9 (28):23904–23908, 2017.

[112] DJ Rogers, F Hosseini Teherani, P Bove, A Lusson, and M Razeghi. Investigation of mgzno/zno heterostructures grown on c-sapphire substrates by pulsed laser deposition. In *Oxide-based Materials and Devices IV*, volume 8626, page 86261X. International Society for Optics and Photonics, 2013.

[113] Zhang Dan, Ji Xu, Lv Pei-Wen, and Huang Feng. Effects of al impurities on the structural, morphological, and optical properties of high mg content mgzno thin films by reactive sputtering. *CHINESE JOURNAL OF STRUCTURAL CHEMISTRY*, 36(8):1271–1275, 2017.

[114] Paul A Anderson. The work function of copper. *Physical Review*, 76(3):388, 1949.

[115] Edgar William John Mitchell and John Wesley Mitchell. The work functions of copper, silver and aluminium. *Proc. R. Soc. Lond. A*, 210(1100):70–84, 1951.

[116] W Li and DY Li. On the correlation between surface roughness and work function in copper. *The Journal of chemical physics*, 122(6):064708, 2005.

[117] W Li and DY Li. Variations of work function and corrosion behaviors of deformed copper surfaces. *Applied Surface Science*, 240(1-4):388–395, 2005.

[118] TA Delchar. Oxygen chemisorption on copper single crystals. *Surface Science*, 27(1): 11–20, 1971.

[119] BK Meyer, A Polity, D Reppin, M Becker, P Hering, PJ Klar, Th Sander, C Reindl, J Benz, M Eickhoff, et al. Binary copper oxide semiconductors: From materials towards devices. *physica status solidi (b)*, 249(8):1487–1509, 2012.

[120] C Mariani and K Horn. Orientation of water adsorbed on cu (110). *Surface Science*, 126 (1-3):279–285, 1983.

[121] S Lee and RW Staehle. Adsorption of water on copper, nickel, and iron. *Corrosion*, 53 (1):33–42, 1997.

[122] Mark C Biesinger, Leo WM Lau, Andrea R Gerson, and Roger St C Smart. Resolving surface chemical states in xps analysis of first row transition metals, oxides and hydroxides: Sc, ti, v, cu and zn. *Applied Surface Science*, 257(3):887–898, 2010.

[123] CD Wagner, AV Naumkin, A Kraut-Vass, JW Allison, CJ Powell, and JR Rumble Jr. Nist standard reference database 20, version 3.4 (web version). *National Institute of Standards and Technology: Gaithersburg, MD*, 20899, 2003.

[124] Rajnikant Borkar, Rashmi Dahake, Sadhana Rayalu, and Amit Bansiwal. Copper oxide nanograss for efficient and stable photoelectrochemical hydrogen production by water splitting. *Journal of Electronic Materials*, 47(3):1824–1831, 2018.

[125] Ju-Yun Park, Kyoung-A Lim, Rex D Ramsier, and Yong-Cheol Kang. Spectroscopic and morphological investigation of copper oxide thin films prepared by magnetron sputtering at various oxygen ratios. *Bulletin of the Korean Chemical Society*, 32(9):3395–3399, 2011.

[126] Kosaku Kishi and Hirofumi Miyoshi. Xps studies of nacl deposited on cu (100) and ni/cu (100) surfaces. *Journal of electron spectroscopy and related phenomena*, 53(4):237–249, 1991.

[127] Hans P Bonzel. Alkali-metal-affected adsorption of molecules on metal surfaces. *Surface Science Reports*, 8(2):43–125, 1988.

[128] Umberto Martinez, Livia Giordano, and Gianfranco Pacchioni. Tuning the work function of ultrathin oxide films on metals by adsorption of alkali atoms. *The Journal of chemical physics*, 128(16):164707, 2008.

[129] P Lange, D Grider, H Neff, JK Sass, and R Unwin. Limitations of the fowler method in photoelectric work function determination: oxygen on magnesium single crystal surfaces. *Surface Science*, 118(1-2):L257–L262, 1982.

[130] Carl L Yaws. *Handbook of vapor pressure: volume 4: inorganic compounds and elements*, volume 4. Gulf Professional Publishing, 1995.

[131] Herbert B Michaelson. The work function of the elements and its periodicity. *Journal of applied physics*, 48(11):4729–4733, 1977.

[132] V Fournier, P Marcus, and I Olefjord. Oxidation of magnesium. *Surface and Interface Analysis: An International Journal devoted to the development and application of techniques for the analysis of surfaces, interfaces and thin films*, 34(1):494–497, 2002.

[133] M Santamaria, F Di Quarto, S Zanna, and P Marcus. Initial surface film on magnesium metal: A characterization by x-ray photoelectron spectroscopy (xps) and photocurrent spectroscopy (pcs). *Electrochimica Acta*, 53(3):1314–1324, 2007.

[134] BV Crist. Xps handbook of the elements and native oxides, xps international, 1999.

[135] A Klein, C Körber, A Wachau, F Säuberlich, Y Gassenbauer, R Schafranek, SP Harvey, and TO Mason. Surface potentials of magnetron sputtered transparent conducting oxides. *Thin Solid Films*, 518(4):1197–1203, 2009.

[136] H Moormann, D Kohl, and G Heiland. Variations of work function and surface conductivity on clean cleaved zinc oxide surfaces by annealing and by hydrogen adsorption. *Surface Science*, 100(2):302–314, 1980.

[137] AT Aldred and JN Pratt. Vapor pressures or zinc, cadmium, antimony, and thallium. *Journal of Chemical and Engineering Data*, 8(3):429–431, 1963.

[138] E Diler, B Lescop, S Rioual, G Nguyen Vien, D Thierry, and B Rouvellou. Initial formation of corrosion products on pure zinc and mgzn2 examinated by xps. *Corrosion Science*, 79:83–88, 2014.

[139] LS Dake, DR Baer, and JM Zachara. Auger parameter measurements of zinc compounds relevant to zinc transport in the environment. *Surface and Interface analysis*, 14(1-2): 71–75, 1989.

[140] G Deroubaix and P Marcus. X-ray photoelectron spectroscopy analysis of copper and zinc oxides and sulphides. *Surface and Interface Analysis*, 18(1):39–46, 1992.

[141] G Moretti, G Fierro, M Lo Jacono, and P Porta. Characterization of cuo–zno catalysts by x-ray photoelectron spectroscopy: Precursors, calcined and reduced samples. *Surface and interface analysis*, 14(6-7):325–336, 1989.

[142] Jiri Duchoslav, Roland Steinberger, Martin Arndt, and David Stifter. Xps study of zinc hydroxide as a potential corrosion product of zinc: rapid x-ray induced conversion into zinc oxide. *Corrosion Science*, 82:356–361, 2014.

[143] Yinhua Zhou, Canek Fuentes-Hernandez, Jaewon Shim, Jens Meyer, Anthony J Giordano, Hong Li, Paul Winget, Theodoros Papadopoulos, Hyeunseok Cheun, Jungbae Kim, et al. A universal method to produce low–work function electrodes for organic electronics. *Science*, 336(6079):327–332, 2012.

[144] Linda Lindell, Mikael Unge, Wojciech Osikowicz, Sven Stafström, William R Salaneck, Xavier Crispin, and Michel P de Jong. Integer charge transfer at the tetrakis (dimethylamino) ethylene/au interface. *Applied physics letters*, 92(16):146, 2008.

[145] LP Mosteller, T Huen, and F Wooten. Photoelectric emission from zn. *Physical Review*, 184(2):364, 1969.

[146] Christopher Martin and Stuart Bowyer. Quantum efficiency of opaque csi photocathodes with channel electron multiplier arrays in the extreme and far ultraviolet. *Applied optics*, 21(23):4206–4207, 1982.

[147] Rachel Chechik and Amos Breskin. Advances in gaseous photomultipliers. *Nuclear Instruments and Methods in Physics Research Section A: Accelerators, Spectrometers, Detectors and Associated Equipment*, 595(1):116–127, 2008.

[148] AF Buzulutskov. Gaseous photodetectors with solid photocathodes. *Physics of Particles and nuclei*, 39(3):424, 2008.

[149] Itamar Israelashvili, AEC Coimbra, David Vartsky, Lior Arazi, Sergei Shchemelinin, EN Caspi, and Amos Breskin. Fast-neutron and gamma-ray imaging with a capillary liquid xenon converter coupled to a gaseous photomultiplier. *Journal of Instrumentation*, 12(09):P09029, 2017.

[150] D Vartsky, I Israelashvili, M Cortesi, L Arazi, AE Coimbra, L Moleri, E Erdal, D Bar, M Rappaport, S Shchemelinin, et al. Liquid-xe detector for contraband detection. *Nuclear Instruments and Methods in Physics Research Section A: Accelerators, Spectrometers, Detectors and Associated Equipment*, 824:240–242, 2016.

[151] P Carlson, T Francke, Bengt Lund-Jensen, and V Peskov. Gaseous photomultipliers with solid photocathodes for the detection of sparks, flames and dangerous gases. *Nuclear Instruments and Methods in Physics Research Section A: Accelerators, Spectrometers, Detectors and Associated Equipment*, 505(1-2):207–210, 2003.

[152] A Breskin. Advances in gas avalanche radiation detectors for biomedical applications. *Nuclear Instruments and Methods in Physics Research Section A: Accelerators, Spectrometers, Detectors and Associated Equipment*, 454(1):26–39, 2000.

[153] GL Harvey. A survey of ultraviolet communication systems. Technical report, NAVAL RESEARCH LAB WASHINGTON DC, 1964.

[154] Zhaotian Sun, Lijun Zhang, Ping'an Li, Yu Qin, and Tingzhu Bai. 1mbps nlos solar-blind ultraviolet communication system based on uv-led array. In *2017 International Conference on Optical Instruments and Technology: Optoelectronic Devices and Optical Signal Processing*, volume 10617, page 106170O. International Society for Optics and Photonics, 2018.

[155] Guanchu Wang, Kun Wang, Chen Gong, Difan Zou, Zhimeng Jiang, and Zhengyuan Xu. A 1mbps real-time nlos uv scattering communication system with receiver diversity over 1km. *IEEE Photonics Journal*, 10(2):1–13, 2018.

[156] Xiaobin Sun, Wenqi Cai, Omar Alkhazragi, Ee-Ning Ooi, Hongsen He, Anas Chaaban, Chao Shen, Hassan Makine Oubei, Mohammed Zahed Mustafa Khan, Tien Khee Ng, et al. 375-nm ultraviolet-laser based non-line-of-sight underwater optical communication. *Optics express*, 26(10):12870–12877, 2018.

[157] Renzhi Yuan and Jianshe Ma. Review of ultraviolet non-line-of-sight communication. *China Communications*, 13(6):63–75, 2016.

[158] Gang Chen, Zhengyuan Xu, Haipeng Ding, and Brian M Sadler. Path loss modeling and performance trade-off study for short-range non-line-of-sight ultraviolet communications. *Optics Express*, 17(5):3929–3940, 2009.

[159] Baisheng Chen, Huanan Wu, and Sam Fong Yau Li. Development of variable pathlength uv–vis spectroscopy combined with partial-least-squares regression for wastewater chemical oxygen demand (cod) monitoring. *Talanta*, 120:325–330, 2014.

[160] CSM Figueiró, D Bastos de Oliveira, MR Russo, ARL Caires, and SS Rojas. Fish farming water quality monitored by optical analysis: The potential application of uv–vis absorption and fluorescence spectroscopy. *Aquaculture*, 490:91–97, 2018.

[161] Thomas Etzkorn, Björn Klotz, Søren Sørensen, Iulia V Patroescu, Ian Barnes, Karl H Becker, and Ulrich Platt. Gas-phase absorption cross sections of 24 monocyclic aromatic hydrocarbons in the uv and ir spectral ranges. *Atmospheric Environment*, 33(4):525–540, 1999.

[162] F Vogt, M Tacke, M Jakusch, and B Mizaikoff. A uv spectroscopic method for monitoring aromatic hydrocarbons dissolved in water. *Analytica Chimica Acta*, 422(2):187–198, 2000.

[163] Cambiador Christian Jay Bautista Leoro Ina Mae Berina, Sto Domingo Angelika Marie Ricohermoso and Cid-Andres Abigail. Biodegradability study of potassium hydrogen phthalate and benzene using bod5 seed as inoculum. *Journal of Bioremediation and Biodegradation*, 9(3):1–5, 2018. ISSN 2155-6199.

[164] Margaret R Douglas and John F Tooker. Large-scale deployment of seed treatments has driven rapid increase in use of neonicotinoid insecticides and preemptive pest management in us field crops. *Environmental science & technology*, 49(8):5088–5097, 2015.

[165] Jesse C Miles, Jessica Hua, Maria S Sepulveda, Christian H Krupke, and Jason T Hoverman. Effects of clothianidin on aquatic communities: Evaluating the impacts of lethal and sublethal exposure to neonicotinoids. *PloS one*, 12(3):e0174171, 2017.

[166] Paula Trumbo, Sandra Schlicker, Allison A Yates, and Mary Poos. Dietary reference intakes for energy, carbohdrate, fiber, fat, fatty acids, cholesterol, protein and amino acids. *Journal of the Academy of Nutrition and Dietetics*, 102(11):1621, 2002.

[167] Takeshi Kimura, Dennis M Bier, and Christine L Taylor. Summary of workshop discussions on establishing upper limits for amino acids with specific attention to available data for the essential amino acids leucine and tryptophan, 2. *The Journal of nutrition*, 142(12): 2245S–2248S, 2012.

[168] Robert H Howland. Dietary supplement drug therapies for depression. *Journal of psychosocial nursing and mental health services*, 50(6):13–16, 2012.

[169] Andy Baker and Roger Inverarity. Protein-like fluorescence intensity as a possible tool for determining river water quality. *Hydrological Processes*, 18(15):2927–2945, 2004.

[170] Naomi Hudson, Andy Baker, David Ward, Darren M Reynolds, Chris Brunsdon, Cynthia Carliell-Marquet, and Simon Browning. Can fluorescence spectrometry be used as a surrogate for the biochemical oxygen demand (bod) test in water quality assessment? an example from south west england. *Science of the total environment*, 391(1):149–158, 2008.

[171] Victor J Norris and Douglas G Currie. Autonomous uv-enhanced-vision system for landing on cat i runways during cat iiia weather conditions. In *Enhanced and Synthetic Vision 2001*, volume 4363, pages 9–21. International Society for Optics and Photonics, 2001.

[172] Sajid Sheikh Muhammad, Benno Flecker, Erich Leitgeb, and Michael Gebhart. Characterization of fog attenuation in terrestrial free space optical links. *Optical engineering*, 46 (6):066001, 2007.

[173] Robert H Dye. Collision avoidance alarm system, October 3 1989. US Patent 4,872,051.

[174] Manuel Edo-Ros. Vehicle collision avoidance system with enhanced pedestrian avoidance, March 27 2018. US Patent 9,925,980.

[175] Scott Philiben and Bradley F Blackwell. Hazard avoidance system, September 6 2005. US Patent 6,940,424.

[176] Marta Ruiz-Llata, Pedro Martín-Mateos, José R López, and Pablo Acedo. Remote optical sensor for real-time residual salt monitoring on road surfaces. *Sensors and Actuators B: Chemical*, 191:371–376, 2014.

[177] Aditya Kumar Bhatt and Deepak Sharma. Lidar technology and applications.

[178] Patrik Jonsson. Remote sensor for winter road surface status detection. In *SENSORS, 2011 IEEE*, pages 1285–1288. IEEE, 2011.